



HAL
open science

Statics and dynamics of ellipsoidal particles in laser beams

Theodor Petkov

► **To cite this version:**

Theodor Petkov. Statics and dynamics of ellipsoidal particles in laser beams. Other [cond-mat.other]. Université de Bordeaux, 2017. English. NNT : 2017BORD0878 . tel-01718275

HAL Id: tel-01718275

<https://theses.hal.science/tel-01718275>

Submitted on 27 Feb 2018

HAL is a multi-disciplinary open access archive for the deposit and dissemination of scientific research documents, whether they are published or not. The documents may come from teaching and research institutions in France or abroad, or from public or private research centers.

L'archive ouverte pluridisciplinaire **HAL**, est destinée au dépôt et à la diffusion de documents scientifiques de niveau recherche, publiés ou non, émanant des établissements d'enseignement et de recherche français ou étrangers, des laboratoires publics ou privés.

Thesis

submitted to

The University of Bordeaux

Faculty of Physical Sciences and Engineering

in order to obtain the degree of

Doctor of Philosophy

Specialty: Optics, Lasers, Nanoscience

by

Theodor Jordanov PETKOV

Statics and dynamics of ellipsoidal particles in laser beams

Thesis directors

Professor Kuan Fang Ren

Dr. Bernard Pouligny

Members of the jury

Catherine Barentin	Professor, University of Lyon, Lumière Matière Institute	Reviewer
Fabrice Onofri	CNRS research director, IUSTI, Marseille	Reviewer
Fang Ren	Professor, University of Rouen, CORIA	Co-director
Bernard Pouligny	Emeritus CNRS research director, CRPP, Bordeaux	Co-director
Philippe Poulin	CNRS research director, CRPP, Bordeaux	Examiner
Jean-Christophe Loudet	Lecturer, University of Bordeaux, CRPP	Examiner

Acknowledgements

Firstly, I would very much like to thank my extremely laudable directors, Bernard Pouligny and Kuan Fang Ren, and our close collaborator, Jean-Christophe Loudet. Without their expert guidance and supervision, I would not have learned anywhere near as much as I did about the field of optics, and the scientific method as a whole. Without a doubt, their help was priceless.

I would also like to thank Patrick Snabre, Pascal Merzeau and Lionel Buisson for invaluable assistance with software that was imperative to the success of the experiments that were performed. The same must be said for the hardware side of things, where I owe a debt of gratitude to both, Philippe Barboteau and the workshop team, as well as Ahmed Bentaleb.

It is also important for me to thank CNRS for financing me, and ANR for providing the funding for the AMOCOPS project (Project ID: ANR-13-BS09-0008), which were both core drivers behind the initiation, and completion, of the thesis work herein.

For supporting me, as well as bringing me much joy, I would like to thank my family and friends, who made it possible to deal with the many obstacles that life tends to throw in peoples' paths, and for helping me not trip up along the way.

Last, but certainly not least, I am very grateful to the reviewers and the members of the jury, whom I deeply respect, namely Catherine Barentin, Fabrice Onofri, and Phillippe Poulin. Their thorough review of this work, and their thoughtful comments and questions, are a testament to their scientific expertise, as well as being an inspiration for any person willing to pursue the fundamental nature of the universe around us.

Glossary

- A - Without index: Rotation matrix
- With index: Amplitude (indices: 1 - perpendicular; 2 - parallel to interaction plane)
- a - Ellipsoid semi-minor axis
- b - Ellipsoid semi-minor axis
- c - Ellipsoid semi-major axis
- D - Divergence factor
- \vec{E} - Electric field
- \vec{F} - Force
- \vec{H} - Magnetic field
- I - Intensity
- \hat{k} - Directional unit vector of ray
- k - Part A: Aspect ratio of spheroidal particles
- Part B: Wavenumber
- \vec{k} - Wave vector
- l - Rayleigh length
- n - Refractive index
- \hat{n} - Unit vector normal to the dioptric surface
- P - Power of laser beam (indices: \uparrow - up beam; \downarrow - down beam; *tot* – total power; *lev* – levitation power)
- p - Order of ray
- R_0 - Radius of mother spheres used to make ellipsoids
- R - Principal curvature radii of wavefront (indices: 1 - perpendicular; 2 - parallel to interaction plane)
- r - Without index: Distance travelled by ray
- With index: Fresnel coefficient of reflection (indices: 1 for perpendicular; 2 for parallel polarisation with respect to the interaction plane)

- S - Complex amplitude
- T - Transmissivity
- t - Fresnel coefficient of transmission (indices: 1 for perpendicular; 2 for parallel polarisation with respect to the interaction plane)
- u - Analogue of x axis for the Gaussian beam
- v - Analogue of y axis for the Gaussian beam
- w - Analogue of z axis for the Gaussian beam
- x - Part A: x coordinate of laser coordinate system

Part B: x coordinate of particle coordinate system
- y - Part A: y coordinate of laser coordinate system

Part B: y coordinate of particle coordinate system
- z - Part A: z coordinate of laser coordinate system

Part B: z coordinate of particle coordinate system
- α - Incident angle of ray
- β - Refracted angle of ray
- ε - Part A: Laser beam power ratio

Part B: Product of Fresnel coefficients (indices: 1 for perpendicular; 2 for parallel polarisation with respect to the interaction plane)
- θ - Part A: Angle between the long axis of the particle and the beam axis (polar angle)

Part B: Angle of rays with respect to the positive z-axis
- λ - Wavelength of light
- ρ - Part A: Density

Part B: Principal curvature radii of dioptric surface (indices: 1 - perpendicular; 2 - parallel to interaction plane)
- $\hat{\mathbf{t}}$ - Tangential unit vector (with respect to surface)
- ϕ - Azimuth angle of the particle system

- φ - Phase
- ω - Laser beam radius (indices: 0 – beam waist; l – local beam radius)

Abbreviations

AO	Acousto-optic deflector
GLMT	- Generalised Lorenz-Mie theory
GO	- Geometrical optics
LMT	- Lorenz-Mie theory
MLFMA	- Multilevel Fast Multipole Algorithm
OL	- Optical levitator
OT	- Optical tweezers
PS	- Polystyrene
RO	- Ray optics
VCRM	- Vectorial Complex Ray Model

Résumé

Ce travail de thèse est une contribution au projet national AMOCOPS, financé par l'ANR. Le thème central du projet est la diffusion de lumière par des particules de formes complexes et de grandes tailles (plusieurs dizaines de μm au moins), domaine où les méthodes de simulation numérique existantes trouvent leurs limites d'applicabilité.

Nous abordons le problème par le biais des effets mécaniques de la lumière, autrement dit les forces et couples créés par la pression de radiation. Étant la conséquence du transfert d'impulsion entre l'onde et la matière, ces effets sont directement liés à la diffusion de lumière. La thèse comprend une partie expérimentale –majoritaire– concernant les réponses mécaniques de particules de polystyrène de forme ellipsoïdale et d'allongement variable sous illumination par un ou deux faisceaux laser. Les cas de faisceaux faiblement focalisés (lévitation optique) et d'un faisceau très fortement focalisé (pincette optique) sont examinés successivement. Nous caractérisons différents types d'équilibre statique, certains d'entre eux non décrits auparavant, obtenus dans les deux géométries. Par ailleurs nous confirmons l'existence de réponses purement dynamiques, où la particule oscille en permanence. Trois nouveaux modes sont observés, deux dans la géométrie lévitation optique et un autre sous pincette optique. Cette étude nous permet de distinguer les oscillations dites de Simpson-Hanna dans le régime linéaire de celles non linéaires mises en évidence avant nous par Mihiretie et al.

Les résultats de nos expériences sont comparés à ceux obtenus par les simulations de J.C. Loudet, sur la base de la simple optique géométrique (OG) et limitées à 2 dimensions (2d). Nous montrons que ces simulations permettent de reproduire qualitativement et comprendre physiquement la plupart des comportements observés dans nos expériences. La principale limitation de ces calculs tient à ce que l'OG ignore le caractère ondulatoire de la lumière. Pour faire mieux et aller vers des simulations fiables quantitativement, il faut développer un modèle alliant optique géométrique et optique ondulatoire. C'est la fonction du modèle VCRM (Vectorial Complex Ray Model) développé récemment par K.F. Ren en 2d. Le but du projet Amocops est de mettre au point la version 3d de la méthode et de la valider sur la base d'expériences comme celles que nous avons conduites. La deuxième partie de la thèse est consacrée à la méthode VCRM. Nous en exposons les principes, et nous présentons quelques résultats des travaux en cours avec une version intermédiaire entre 2d et 3d, dite « 2d+ ». Quelques illustrations sont proposées sur des exemples impliquant des sphères et ellipsoïdes de grandes tailles.

Abstract

This work is a contribution to the “AMOCOPS” project, funded by Agence Nationale de la Recherche. AMOCOPS is dedicated to the development of new computation schemes to simulate the light scattering patterns of large complexly shaped particles. Particle sizes are of the order of several 10s of micrometres, which is at the limit, or beyond the capabilities of currently available computation techniques.

Our work indirectly deals with light scattering through the corresponding mechanical effects of light. Light scattering is the source of momentum transfer between light and matter, and therefore of the forces and torques acting on the exposed particles. The majority of Part A of this thesis is about the mechanical responses of ellipsoidal polystyrene particles of varying aspect ratios, under illumination by one or two laser beams. We investigate the case of weakly focused beams (optical levitation), and that of a single large aperture beam (optical tweezers). Different types of static equilibria, some of which are new, are observed and characterized in both geometries. We confirm the existence of dynamic states, whereby the particle permanently oscillates within the laser beam(s). Three new oscillation modes are observed, two of them in the conditions of optical levitation, and another one in the optical tweezer geometry. The study allows us to make a distinction between noise-driven oscillations in the linear regime, of the type predicted by Simpson and Hanna, and nonlinear oscillations such as those evidenced prior to this work, by Mihiretie et al.

Results from our experiments are compared to simulations by J.C. Loudet, using simple ray-optics (RO) in two dimensions (2D). We show that results from 2D-RO qualitatively match most of our observations, and allow us to physically understand the main mechanisms at work in the observed phenomena. The simulations cannot be quantitatively exact, due to the 2D limitation, and because RO essentially ignores the wave nature of light. In Part B of the manuscript, we present the principles of the Vectorial Complex Ray Model (VCRM), which was recently developed by K.F. Ren in 2d. The goal of AMOCOPS is to develop a full 3D version of VCRM, able to simulate light scattering by particles of any shape with a smooth surface. We explain the basics of the model, as well as the “2D+” version, which is an extension of the basic 2D-

VCRM. A few illustrative examples of light scattering patterns computed with 2d+-VCRM for large-sizes spheres and ellipsoids are presented.

Contents

Acknowledgements	3
Glossary.....	5
Abbreviations	9
Résumé	11
Abstract.....	12
General introduction.....	17
Part A.....	21
A-1. Introduction	23
A-2. Experimental hardware and methods.....	29
A-2.1. Particle fabrication and characteristics	29
A-2.2. Two-beam optical levitator setup.....	31
A-2.3. Single beam optical tweezer setup.....	37
A-3. Experimental results	43
A-3.1. Static equilibria of spheres	43
A-3.2. Static equilibria of spheroids	57
A-3.3. Dynamic states of spheroids	61
A-3.4. Bifurcation diagram	64
A-3.5. Single beam three-dimensional trapping.....	67
A-4. Numerical simulations.....	87
A-4.1. 2D RO forces and torques	88
A-4.2. Two-beam levitation.....	92
A-4.3. Single tightly focused beam (optical tweezers).....	98
A-5. Discussion	105
A-5.1. Manipulation of spheres using the optical levitator	105
A-5.2. Manipulation of ellipsoids using an optical levitator and optical tweezers	107
A-6. Conclusion of Section A.....	117
Part B.....	119

B-1. Introduction	121
B-2. Classical models for light scattering	123
B-2.1. Lorenz-Mie theory	124
B-2.2. Generalized Lorenz-Mie theory	126
B-2.3. Geometrical Optics	128
B-3. Vectorial Complex Ray Model.....	135
B-3.1. General principles	136
B-3.2. Gaussian beam.....	149
B-4. Results and discussion	157
B-4.1. Scattering diagrams for spheres	157
B-4.2. Scattering diagrams for spheroids.....	161
B-5. Conclusion of Section B.....	165
General Conclusion	167
Bibliography	171
Appendices	179
Sedimentation of spheroids in viscous fluid	179
Numerical aperture calibration.....	183
Spheroid tilt-tracking software	185

General introduction

The work reported in this dissertation is part of a large project called “Advanced Methods for Optical Characterization of Complex Particle Systems”, or AMOCOPS for short, led by Professor Kuan Fang Ren (CORIA, Rouen). AMOCOPS has research teams in Rouen, Lyon, Marseille and Bordeaux, and is funded by Agence Nationale de la Recherche (ANR).

The project deals with the optical properties of droplets, as well as particles of “complex” shape, whose size is beyond a few wavelengths of visible light, up to tens of micrometres. Complex-shaped particles (CSPs) can be found everywhere: fluid mechanics (multiphase flows, sprays, aerosols etc.), atmospheric physics, chemical engineering and the life sciences are just some examples. Attempts to characterize particles in flows exploit their far-field light scattering properties, which can be characterized by various experimental techniques (laser diffraction spectrometry, phase Doppler interferometry and particle imaging are standard). The intensity of the scattered light is taken into account in different directions and across a given time period to deduce the characteristics of the particles present inside the probed volume of a system. If the particles are sufficiently similar in size, shape, constitution, and are not too large (less than 100 μm , say), then essential characteristics can be determined from the scattered light through approximate inversion procedures. These procedures are based on theoretical models for light scattering that are used to calculate the characteristics of light scattered by a given type of particle, or an ensemble of such particles.

In general, the modelling of the interaction between light and particles is a difficult problem. Many theories have been developed to deal with scattering, absorption and radiation pressure. Rigorous methods are limited to particles with simple shapes (spheres and cylinders) due to theoretical or computational barriers; however, there are numerical methods capable of dealing with CSPs. These include the T-matrix, the Discrete Dipole Approximation (DDA), the Method of Moments (MoM) and the Finite Difference Time Domain (FDTD) techniques [1], which allow the calculation of the scattering properties of arbitrarily shaped particles, although there are still some limitations related to size, shape and processing power. There is currently no single perfect method to encompass all particle shapes and sizes within a few tens of microns, but more relevantly, there is no accurate method to perform the calculations for particles larger than a few tens of microns. The ultimate goal of the AMOCOPS project is to develop a novel model which relies on the combination of both, rays and waves, and is then easily applicable to the calculation of scattering diagrams for large CSPs, including above a few tens of microns.

Ray tracing, or Geometrical Optics (GO), is flexible when it comes to particle shapes. However, it may completely, or partially, neglect the contribution of wave effects and many internal reflections to the overall scattered field. Recently, Ren et al. [2, 3, 4, 5, 6] have successfully introduced wave properties to the geometrical optics model, and developed a mathematical formalism that allows the consideration of wavefront curvature as well as the phase shift due to focal lines. This approach is called the Vectorial Complex Ray Model (VCRM), and it permits the precise computation of the scattering of an incident wave by a large CSP with a smooth surface. Prior to this thesis, a two-dimensional version of VCRM has been developed to deal with the scattering of a plane wave by elliptical cylinders and ellipsoidal particles [2, 3, 4]. To include diffraction effects, Ren et al. have proposed methods based on the Heisenberg uncertainty principle, and introduced near-critical-angle scattering effects in the model. AMOCOPS aims to offer a full three-dimensional version based on the above considerations, which can be generally be called the Ray Theory of Waves.

In parallel to the development of VCRM, the AMOCOPS project is also concerned in large part with experimental work. Some of the experiments, are directly aimed at measuring light scattering intensities of well-defined CSPs in controlled conditions [5]. Furthermore, light scattering is a source of the so-called “radiation pressure”, and of the mechanical effects of light in general, which are the direct manifestation of the momentum carried by electromagnetic waves. In essence, scattering by a particle has the effect of changing the direction of momentum carried by the light, which is the source of the force that acts upon the particle in order to preserve the conservation of momentum. Whenever the particle is non-spherical, the momentum transfer translates as both, force and torque, which can make the particle move and rotate. In general, the effect of radiation pressure is negligible on the scale of macroscopic objects and classical light sources, but can be quite significant in the case of a focused laser beam illuminating the cross-section of a micrometre-sized particle.

Investigating the mechanical effects of light is the central aspect of the experimental part of the work performed throughout this thesis. To this end, experiments have been carried out in CRPP (Bordeaux) with ellipsoidal particles that are exposed to one, or two, laser beams. The goal of these experiments was to gather data on the light induced forces and torques that are obtained when a single particle is manipulated using, most commonly, an optical levitator, or in a few cases, optical tweezers. This work is reported in Part A of this dissertation and consists of various experimental results procured with spheroids a few tens of microns in length. Their responses, either static or dynamical, are described. As will be seen, static configurations are directly exploitable for quantitative comparison with the predictions of existing models, such as one based on MoM, and a classical, two-dimensional ray-optics (2D RO) model. Beyond

the static states, a great deal of attention is also devoted to the dynamical states, which are light-driven oscillations of the particles. Existing theories are able to account for a large part of the observed phenomena. 2D RO predicts the polar angle oscillations seen in many experiments, but is very approximate, and limited to two dimensions, which means it misses the three-dimensional motions. MLFMA (the MoM based model) has the potential to provide very accurate force and torque maps in three dimensions, and therefore account for all of the phenomena, but it is very computationally expensive.

Part B is about VCRM, proposed here as an inexpensive, yet still accurate tool, better suited for some practical purposes. The model is still far from a real three-dimensional version; however, an intermediate version is reported, which takes into consideration some three-dimensional features, whilst staying within a two-dimensional framework. This is achieved by including the curvature of the ellipsoid perpendicular to the scattering plane, with the scattering plane being a plane of symmetry of the ellipsoid, and therefore setting up the scenario as two-dimensional. Both, a plane wave and a Gaussian beam are incorporated into the model as sources of light, as well as wavefront curvature and phase, which takes into account the Gouy phase (applicable to the Gaussian beam), the phase shift due to focal lines and the shift resulting from total reflection. The model also utilises vectors as a means of directing the rays, thus making it easier for the evolution into a full three-dimensional version to occur, as well as making the calculations more efficient. Moreover, in order to have some comparison between experiment and theory, the linear forces acting on the particles are calculated using the VCRM framework. This will be discussed in much greater detail in Part B.

Part A

Behaviours of spheroidal micro-particles in one- and two-beam trap configurations

A-1. Introduction

Laser beams powered by a few milliwatts are known to produce forces in the piconewton range, well above the threshold necessary to levitate and manipulate a micrometre sized dielectric particle [7]. Ever since the invention of optical tweezers (OT) [8], which are based on a single large aperture beam, considerable savoir-faire and theoretical knowledge have been accumulated in the art of trapping and manipulating particles with light [9].

However, research has been predominantly focused on the simplest kind of particles, namely spheres. Trapping of non-spherical particles is both, very different, and less mastered, than that of spheres [10]. Currently, a lot of physicists and engineers show interest in the trapping and manipulating of elongated particles, in great part due to the proliferating applications of nanotubes and nanorods in biophysics, microfluidics, microelectronics and photonics [11, 12, 13, 14]. For example, a goal pursued by engineers is to assemble micron-sized structures and mechanisms made of these particles, a challenge that necessitates optical trapping, not just for the positional and orientational control over individual rods, but also because of its nonintrusive nature [13, 15].

A collection of recent theoretical and numerical studies, thoroughly reviewed in [16], explored the trapping properties of rods [17, 18], cylinders [19, 20, 21, 22], as well as prolate and oblate ellipsoids [23, 24, 25, 26]. Both attraction and repulsion from the beam axis have been predicted, along with stable tilted orientations in the case of cylinders.

In biology, double-beam fibre-based optical traps have been used to characterize the deformability of red blood cells and fibroblasts [27]. The method yields information on the elasticity of cells, and could be the basis of a high throughput medical diagnosis tool. Inverting data into quantitative elasticity parameters, however, demands theoretical knowledge of the radiation pressure forces acting on the deformed cells.

Calculating the forces and torques exerted by light on a particle is closely related to calculating the way in which this particle scatters light. This matter is very well documented for spherical particles. For instance, K.F. Ren has used Generalized Lorenz-Mie theory (GLMT) to predict the radiation pressure forces of a Gaussian beam on a spherical particle, and developed user-friendly software capable of determining this for different types of spheres and beams [28]. A number of theoretical works have been dedicated to the prediction of radiation pressure [29, 30, 31, 32, 33, 34], and finding the equilibrium configurations of cylinders [11, 19, 20, 21] and

ellipsoids [24] inside single beam traps. These, however, are limited to very small particles. As aforementioned, there is a definite need to go beyond the current achievements. In reality, the above examples involving rods and deformed cells still lack the quantitative predictions necessary for the simulations to be considered fully operational.

The work of this thesis is focused on the ellipsoidal particle case. Recently, Mihiretie et al. carried out systematic experiments using an optical levitator to trap ellipsoid-shaped particles made from polystyrene spheres [35, 36, 37]. Various configurations of the levitation were studied, with different values of the particle aspect ratio (defined as $k_1 = \frac{c}{a}$ and $k_2 = \frac{c}{b}$, with $c > a > b$, where a , b and c are the semi-principal axes of the ellipsoid, of which c is the longest). Particles with $k_{1,2} \leq 3$ near the beam-waist ($\omega_0 \cong 1.3\mu\text{m}$) of the levitation beam were found to align their semi-major axis along the beam axis, a configuration that allows for a straightforward and accurate measurement of the levitation power, P_{lev} , and then of the axial radiation pressure force, F_{lev} . The particles in these experiments were up to several tens of microns in length, beyond the limits of current computational methods.

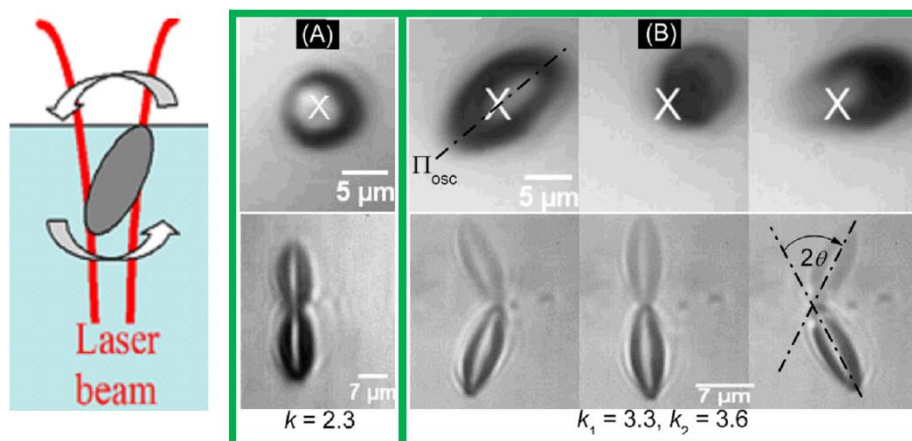


Figure 1: These are images from above (the top row) and from the side (the bottom row) of particles with a different aspect ratio inside the optical levitator setup. They are suspended in water, which is inside a quartz cuvette. Photos show the regimes observed with a low-aspect ratio ellipsoid (A) and a more elongated particle (B). The power of the laser in the sample is 17mW. The dotted line on top marks the instantaneous plane of polar angle θ oscillation (Π_{osc}). The particles are in contact with the ceiling (water-quartz interface) of the sample cell. The reflection on the interface creates a mirror image of the particle, hence the impression that there are two particles in the side view images. The oscillation of (B) is readily visible, as it breaks the alignment between the particle and its mirror image. The photos of top row show the particles in relation to the beam axis, depicted as a white X.

It is noteworthy that these experiments, as well as others with rod-like particles, have revealed that optical trapping of non-spherical particles does not simply summarize into either stable (immobile), or unstable (rejection from the laser beam) states [11, 12, 38, 10]. The experiments

performed by Mihiretie et al. [35, 36, 37] showed that ellipsoidal particles either come to rest along the beam axis, or go through a characteristic tumbling motion, with a transition between both regimes that depends on the aspect ratio of the particles and the beam waist radius. The motions, shown in Figure 1, consist of oscillations in the polar angle, θ , which is the angle between the particle symmetry axis and the laser beam axis, coupled with a back and forth translational motion of the particle centre, all of which occurs along the oscillation plane, Π_{osc} . As was shown by Mihiretie et al., the polar angle oscillations can be understood through a simple ray optics model [39]. This was limited to two dimensions, as it only considered the interaction of light with an elliptical body inside a plane. Remarkably, it was able to capture the main physical aspects of the situation and reproduce the same bifurcation between the static and oscillating states as was obtained experimentally. It helped with the understanding of the origin of the tumbling phenomenon, which can be explained with the structure of the force and torque functions.

However, whilst the 2D RO model has been very helpful in providing physical insight into the origin of the polar angle oscillations, its relation to the experimentally observed phenomena is only qualitative. The model does not include diffraction, interference between the light rays, and ignores the three-dimensional nature of the real system. An improved version of the model is necessary, together with more quantitative data from the experimental side. Further data are necessary, as they may serve to further — and more accurately — validate numerical simulations. The general goal of the experiments carried out during this thesis was to extend Mihiretie's work on ellipsoid-shaped particles in several different ways:

- ❖ The provision of accurate measurements of levitation powers in the basic configuration, which consists of the particle standing vertically and coaxially with a single laser beam that propagates in opposition to the direction of gravity. Values of P_{lev} can be calculated directly using existing models (GLMT for spheres, RO and MLFMA [40] for ellipsoids) and compared to measured experimental values.
- ❖ The extension of the single-beam levitation scheme to a two-beam geometry. In this case, the particle is manipulated by a couple of coaxial confocal contra-propagating beams, whose powers can be controlled independently. As we will see, the 2-beam geometry leads to non-trivial static configurations of the ellipsoidal particles. These are especially interesting, because they subtly combine optical forces and torques in an overall asymmetric particle equilibrium. Because the configuration is static, hydrodynamic forces and torques do not exist, and hence make the equilibrium equations simpler to deal with.

- ❖ The systematic observation of dynamical states, whereby a particle permanently moves in either the one-beam, or the two-beam geometry. As will be reported, two new types of oscillatory regimes are observed when ellipsoidal particles are exposed to two-beam illumination. These depend on the power ratio between the two beams, as well as the aspect ratio of the particles.
- ❖ To test three-dimensional trapping of long ellipsoids with an optical tweezer (OT) setup. This case differs from the levitation experiments mainly because of the use of a single very large aperture beam, as opposed to a moderately focused small aperture one, as is the case in the optical levitator. It is of interest to study the influence of the beam aperture up to that provided by high magnification microscope objectives. Three-dimensional trapping is effective, as we will see, and a different type of particle motion can be produced, resulting from the combined action of thermal agitation and optical torque.

Below, in Section A-2, the optical setups and related experimental procedures will be described. This includes the optical levitator (OL), as well as the optical tweezers (OT).

In Section A-3, the main experimental observations will be reported, starting with the a priori simple case of spherical particles in the OL, which is dealt with in some detail, mainly to test our understanding of the equilibrium of such a particle in a one- and two-beam geometry. As will be seen, there is still much to learn, even with spheres. Next, the behaviour of ellipsoids in the OL is addressed, both for static and dynamical states concerning one and two-beam configurations. The many types of responses obtained with the two-beam arrangement of the OL are gathered into a single diagram, where the particle aspect ratio, k , and the beam power ratio, ε (defined as $\varepsilon = \frac{P_{\downarrow}}{P_{\uparrow}}$), play the role of control parameters. This is found in Section A-3.4. Section A-3.5 is devoted to the experiments performed with the OT for spherical and ellipsoidal particles. The stability of 3D trapping is studied, as well as the interference of the sample cell with the particle trapping. A new type of oscillation, occurring when the particle is in contact to the bottom of the sample cell, is described and proven to be different from the oscillations seen in the OL experiments. Finally, the gathered data are discussed in Section A-5, where the emphasis is on distinguishing between the different types of dynamical regimes observed in the OL and OT geometries, with an insistence on the difference between the nonlinear OL oscillations, and what are believed to be noise-driven incoherent OT oscillations.

Numerical results, obtained with GLMT, RO and MLFMA, are discussed in Sections A-4 and B-2. In Section A-3, these three methods are used for comparison with the experimental data of the levitation powers of polystyrene spheres and ellipsoids, in the simple vertical coaxial configuration with a single laser beam. We then move to the case of the off centred, tilted, static configurations, and the polar angle oscillatory regimes. The problem of dynamical states has the added complexity of fluid mechanics, since the dissipation due to the fluid viscosity must be incorporated into the equations of motion. This combination of optical and fluid dynamics is examined with the simple 2D RO model proposed by Loudet et al. [39], which is currently the only method available for the simulation of time-dependent responses. Based on the results of the 2D RO simulations, a (k, ε) state diagram is produced and compared to its aforementioned experimental counterpart. As will be seen, 2D RO still performs fairly well, in so far as the theoretical and experimental diagrams have some definite similarities.

These results are commented on in Section A-5. The section is ended with the distinction that must be made between sustained large amplitude oscillations and the noise-driven motions of similar appearance.

Part A is then finished with a summary of the main results, and a conclusion, in Section A-6.

A-2. Experimental hardware and methods

A-2.1. Particle fabrication and characteristics

The ellipsoidal particles were fabricated from polystyrene (PS) “mother” spheres, each with a radius of R_0 , following the mechanical stretching procedure used by Mihiretie et al., as well as others [37, 41, 42]. Prolate ellipsoids with semi-principal axes a , b and c (Figure 2) were obtained by uniaxial stretching, and since all of the used particles were spheroids, whereby $a = b$, they can be characterized by a single aspect ratio, $k = \frac{c}{a}$, ranging from $k = 1$ (sphere) up to $k = k_{max} \gg 1$. In principle, stretching preserves the particle volume:

$$V_0 = \frac{4}{3}\pi R_0^3 \quad \text{A.1}$$

The length of the spheroid can then be given by:

$$2c = 2k^{\frac{2}{3}}R_0 \quad \text{A.2}$$

The optical levitator is operated with 50x objectives (see Section A-2.2), hence “large” particles were used. These were made from $R_0 \approx 5\mu\text{m}$ mother spheres, and had aspect ratios up to $k_{max} \approx 4.5$. Therefore, the longest particles had a length of $2c_{max} \approx 30\mu\text{m}$. On the other hand, since the optical tweezers (see Section A-2.3) use a large aperture, high magnification (100x) objective, smaller spheres were used for the stretching procedure, where $R_0 \approx 3\mu\text{m}$. Tests were made with aspect ratios up to $k_{max} \approx 7$, with a corresponding length, $2c_{max} \approx 20\mu\text{m}$.

Further details of the ellipsoid fabrication can be looked up in [37, 41, 42]. Once stretched, the particles were dispersed in ultra-pure water (from a Millipore Milli-Q purification system) at very low concentrations, such that only one particle was visible within the microscope field of view at any given time, in order to reduce the chance of unwanted particles interfering with the beam during an experiment.

It is assumed that the volume of the ellipsoids is the same as that of the corresponding mother spheres, as we see no reason why stretching would modify the density, or the composition, of the particle’s material, polystyrene.

This may be checked by using sedimentation experiments. The density of a spherical particle with known parameters can be experimentally determined from its sedimentation velocity:

$$v_{sed} = \frac{2\Delta\rho g R^2}{9\eta} \quad \text{A.3}$$

where η is the fluid viscosity ($\sim 10^{-3} \text{Pa} \cdot \text{s}$), $\Delta\rho$ is the difference in density between the particle and the fluid medium (0.05gcm^{-3} for polystyrene in water), and g is the acceleration due to gravity. Optical levitation is the ideal tool for studying the sedimentation dynamics of single particles. A particle is initially lifted up, close to the ceiling of the cuvette, and then the laser is switched off, letting the particle fall freely. A large sphere, for example with a radius of $R_0 \approx 5 \mu\text{m}$, then falls down roughly vertically, with minor disturbance caused by Brownian motion. Measuring the sedimentation velocity, v_{sed} , is straightforward, and obtaining the value for the density follows.

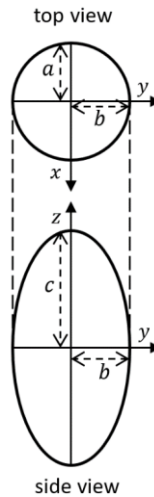


Figure 2: An example of the geometry of a prolate ellipsoid with semi-axes a , b and c , in our (x, y, z) coordinate system

A number of sedimentation tests were also performed using spheroidal particles (see Appendix - Sedimentation of spheroids in viscous fluid for further details). In short, these experiments revealed that the free-falling trajectories of spheroidal particles are more complex than expected. According to theory, a spheroid-shaped particle is expected to keep its initial tilt angle (θ_0) during the full sedimentation process [43, 44], meaning that one can then measure the corresponding sedimentation velocity, $v_{sed}(\theta_0)$, and deduce the value of the particle density in the same way as for a sphere. Surprisingly, however, it was observed that each of the tested particles would change its orientation during sedimentation, in strong contradiction with the expected behaviour. This occurred in a similar way for both, the 1mm

and 2mm thick cuvettes used for optical levitation, as well as with the 0.1mm thick cells used for the optical tweezers. Sedimentation velocities could only be measured in short intervals, where the particle tilt was approximately constant. Due to this limitation, measured velocities were less accurate than those obtained with spheres; however, the differences between the obtained density values and the expected value, 1.05gcm^{-3} , were negligible. Although this issue deserves a more thorough study, it is assumed here that all the ellipsoids have the same volume and density as that of their mother spheres. As will be seen, this assumption is compatible with the experimental results.

A-2.2. Two-beam optical levitator setup

The concept of an optical levitator, in its most minimalist state, simply amounts to a single vertical laser beam, propagating in the opposite direction to gravity [7]. The beam is moderately focused, with a beam waist radius, ω_0 , of a few micrometres, which is a similar size to that of the polystyrene spheres used in the experiments. The corresponding Rayleigh length:

$$l = \frac{\pi\omega_0^2}{\lambda} \quad \text{A.4}$$

with λ as the wavelength of light, is at least of the order of several tens of micrometres, meaning that the beam is an approximate cylinder on the scale of the particle. Such a beam, generated with a few milliwatts of power, is strong enough to levitate a PS or glass particle in water. Whenever the index of refraction of the particle (in this case $n_{PS} = 1.59$ for PS) is larger than that of the surrounding medium ($n_w = 1.33$ for water), then the particle gets trapped at the beam axis, but is free to move along it (see Figure 3). Thus, the configuration can only achieve two-dimensional trapping, and only within a plane perpendicular to the beam axis. Vertical equilibrium can also be achieved by tuning the laser power, P , such that the optical force is just enough to balance the buoyant weight of the particle. The optimal value then corresponds to the levitation power, P_{lev} . Note that this configuration does not realise three-dimensional trapping because increasing P makes the particle move upward, instead of locking its position along the beam axis.

As was shown by Mihiretie et al. [35, 36, 37], levitation, as well as two-dimensional trapping, was similarly achieved with low aspect ratio ellipsoids (with $k < 3$ and $\omega_0 = 1.3\mu\text{m}$), which stay vertical along the beam axis. Conversely, higher aspect ratio ellipsoids were observed to

undergo permanent polar angle oscillations along a plane passing through the beam axis (see Figure 3 (c)).

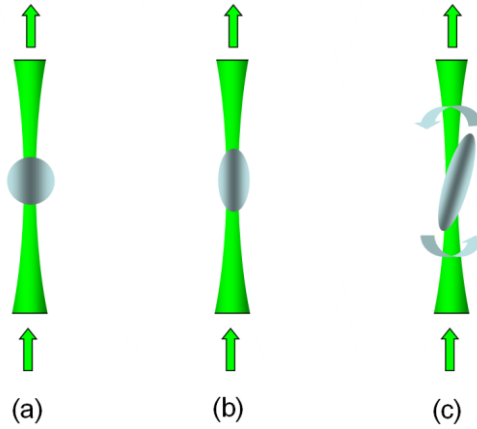


Figure 3: This is a depiction of single beam levitation with a sphere (a) and a short ellipsoid (b). A longer ellipsoid (c) does not stay static across the beam, but is observed to oscillate, both in tilt and position, relative to the laser beam axis.

The main parts of the setup are sketched in Figure 4. It is essentially an optical levitator, based on a pair of vertical counter-propagating Gaussian laser beams arranged in a triangular geometry. Both beams are generated from a single beam by means of a polarizing beam splitter cube (BS) [45, 46, 47]. The source is a Coherent Genesis continuous wave laser, with a vacuum wavelength, $\lambda_0 = 514\text{nm}$.

Each beam goes through a long working-distance microscope objective and is focused down to a small spot inside a 1mm thick quartz cuvette (QC). In most experiments, a couple of Zeiss objectives (Zeiss Epiplan 50x, NA = 0.5) were used. The cuvette contains a highly diluted water suspension of the ellipsoids to be manipulated, and is mounted on an (x, y, z) translation stage. Thus, the sample can be moved relative to the beams in any direction. Both objectives can also be independently moved in x, y and z too. Motions in x and y are driven by four piezoelectric actuators (Aerotech 101 Zeta Drive), allowing for sub-micrometre accuracy.

Combining the BS with a half-wave plate lets us control the power ratio of the “up” and “down” beams, whereby we can use either one on its own, or any combination of both. The total power, P_{tot} , inside the sample is defined as:

$$P_{tot} = P_{\uparrow} + P_{\downarrow} \tag{A.5}$$

where P_{\uparrow} and P_{\downarrow} are respectively the powers of the up and down-beams. Changing the orientation of the half-wave plate ($\lambda/2$ in Figure 4) allows us to tune the power ratio, ε . When $\varepsilon = 0$, all the power is directed to the up-beam, which corresponds to the basic one-beam levitation scheme. The value of ε is given by $\cos^2 \xi$, where ξ is the angle by which the half-wave plate is rotated, starting from the position which gives full power to the up-beam. The two-beam levitation scheme requires that $\varepsilon > 0$, meaning that a fraction of the power is given to the down-beam. In the experiments with ellipsoids, we used values of ε up to about 1.5, a situation where more power is fed to the downward beam than to the upward one. This situation may seem paradoxical, but is not in reality whenever the particle (an ellipsoid) is tilted and off-cantered.

While the power ratio is determined by the orientation of the half-wave plate, measuring the absolute value of the power inside the sample cell requires using a power-meter and a calibration procedure. A small fraction ($\sim 10\%$) of the beam close to the laser source is siphoned off by a beam-splitter into a thermoelectric sensor (Ophir 12A-SH-V1 ROHS). We thus obtain the value of the power reaching the Ophir detector, P_{Ophir} . A second power-meter, with a slim sensor probe (Coherent OP2), is used to measure the power between ML_1 and ML_2 . The latter value is corrected for the losses due to the quartz cuvette full of water, which has a total transmission of $T_{cuvette} = 0.9465$, meaning that the sample experiences a fraction of $\sqrt{T_{cuvette}} = 0.9729$ of the light entering the cuvette. We then compare the measured powers of the Coherent OP2, P_{OP2} , to those of the Ophir power meter, P_{Ophir} , when all the power is directed either to the up-beam, or to the down-beam, respectively. Repeating this for different beam powers gives the corresponding proportionality constants for P_{\uparrow} and P_{\downarrow} . We can therefore know the values of the beam powers passing through the sample during routine operation based on the values of P_{Ophir} and ξ .

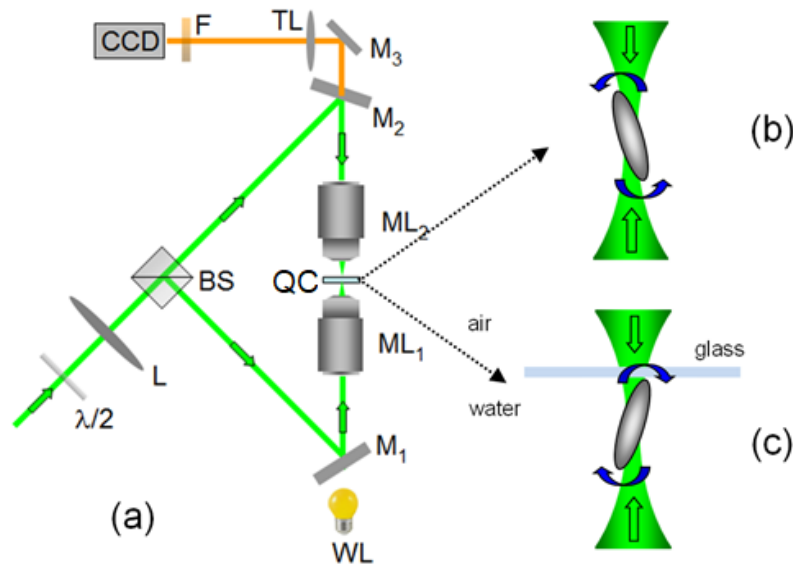


Figure 4: (a) Optical setup. The setup functions as a two-beam levitator, including a classical microscope (TL is the tube lens) with bright field illumination (WL is the white light Koehler source). $M_{1,2}$ are dichroic mirrors, BS is the polarizing beam splitter, $\lambda/2$ is the half-wave (514 nm) plate. The beam waist of the laser, ω_0 , is located within the focal plane common to the microscope objectives, ML_1 and ML_2 (confocal scheme). It can be varied by changing the lens, L, and/or ML_1 and ML_2 . The sample (QC) is located between ML_1 and ML_2 . Optical images are recorded by a Charge Coupled Device (CCD) camera fitted with a set of filters (F). The green arrows show the direction of the beams. (b) Levitation in bulk water. (c) Levitation at the water-quartz interface. The curved arrows in (b) and (c) indicate the oscillatory behaviour of the ellipsoid, which depends on the values of both the aspect ratio, k , and the power ratio, ε . Distances are not to scale in the interest of clarity.

The two beams are supposed to be co-axial and confocal, meaning that the corresponding beam waists and cross-sections in the observation plane are superposed. This is achieved through a systematic alignment procedure. In the last step of the procedure, we use a beam profilometer (Thorlabs BP209-VIS) (see Figure 5). This device works with a couple of slits that scan across a magnified image of the beam waist cross-section. Both beam cross-sections can be detected simultaneously by tuning the power ratio to $\varepsilon \sim 1$. A defect in superposition clearly shows up as two distinct peaks in the intensity profile. This can then be easily eliminated using the piezo-actuators. A narrow beam waist (for example $\omega_0 = 1.6 \mu\text{m}$) gives sharp peaks, which can be superposed with sub-micrometre precision. Conversely, a large beam waist gives smoother peaks, naturally resulting in a larger uncertainty in superposition. Overall, the error in this process is a roughly constant, at about 15% of the beam waist radius, ω_0 .

In our experiments, P_{tot} typically ranged from 1mW to 30mW. The levitation of the mother spheres typically required $P_{\uparrow} \approx 1.2\text{mW}$, a value which may be taken as a reference power. For

most dynamic state systematic experiments, a range of $8\text{mW} \leq P_{tot} \leq 20\text{mW}$ was used. The beam waist radius, ω_0 , can be chosen to be between $1.3\mu\text{m}$ and about $9\mu\text{m}$ with appropriate combinations of the lenses L and $ML_{1,2}$, of focal lengths f_L and f_{ML} respectively. The lens L is located between the laser source and the beam-splitter, at distance f_L from the rear aperture diaphragm of $ML_{1,2}$. The value of f_L is chosen based on the following reasoning using standard formulas for the transformation of Gaussian beams [48]. Let ω_L be the beam waist radius of the beam delivered by the laser source (in this case, $\omega_L \approx 0.95\text{mm}$). L focuses the beam down to:

$$\omega_1 = \frac{\lambda f_L}{\pi \omega_L} \quad \text{A.6}$$

inside the rear focal planes of $ML_{1,2}$. The beam waist inside the sample plane is then given by:

$$\omega_0 = \frac{\lambda f_{ML}}{\pi \omega_1} = \left(\frac{f_{ML}}{f_L} \right) \omega_L \quad \text{A.7}$$

The Zeiss 50x objectives have focal lengths, $f_{ML} = 3.29\text{mm}$. With these objectives in operation, we expect a lens of focal length $f_L = 2\text{m}$ to produce $\omega_0 \approx 1.6\mu\text{m}$, and one with $f_L = 1\text{m}$ to produce $\omega_0 \approx 3.1\mu\text{m}$. These predicted values were verified using the beam profilometer. The obtained beam waist radii were $\omega_0 = 1.7\mu\text{m}$ and $\omega_0 = 3.6\mu\text{m}$, with the corresponding Rayleigh lengths in water equal to $l \approx 21\mu\text{m}$ and $l \approx 105\mu\text{m}$, respectively. Most of the experiments performed with the optical levitator were done with these two beam waist values.

In addition to their role of focusing the laser beams, the long-working-distance objectives ($ML_{1,2}$) are used as a condenser and for imaging, respectively. The sample is illuminated by a white light source (WL), in a classical Koehler configuration. Images are built onto the sensor of a digital camera (Edmund Optics, EO-1312M) by means of a tube lens (TL) of focal length $f_{TL} = 300\text{mm}$. In principle, the green laser light is supposed to be totally reflected by the mirror, M_2 . In reality, a small fraction can pass through, which is enough to saturate the camera. This green light can be partially, or totally blocked by a set of different filters (F) positioned before the camera. By choosing an adequate filter, we can see a faint image of the beam cross-section on the live video produced by the camera, and use it for the tuning and alignment necessary for an experiment.

Video images can be recorded by means of the Ueye software (IDS Imaging Development), or with a home-made, modified version of Ueye (created by Pascal Merzeau). The latter version includes a very useful feature, whereby the values of the main experimental parameters (the video frame rate and beam powers) are recorded and displayed at the bottom of each video. Video images and films are later analysed using ImageJ software (National Institute of Health, USA). To determine the particle trajectories, as well as other parameters, we used lab-made particle-trackers developed and provided by colleagues of CRPP (Patrick Snabre, Jeremy Vrignon, Pascal Merzeau).

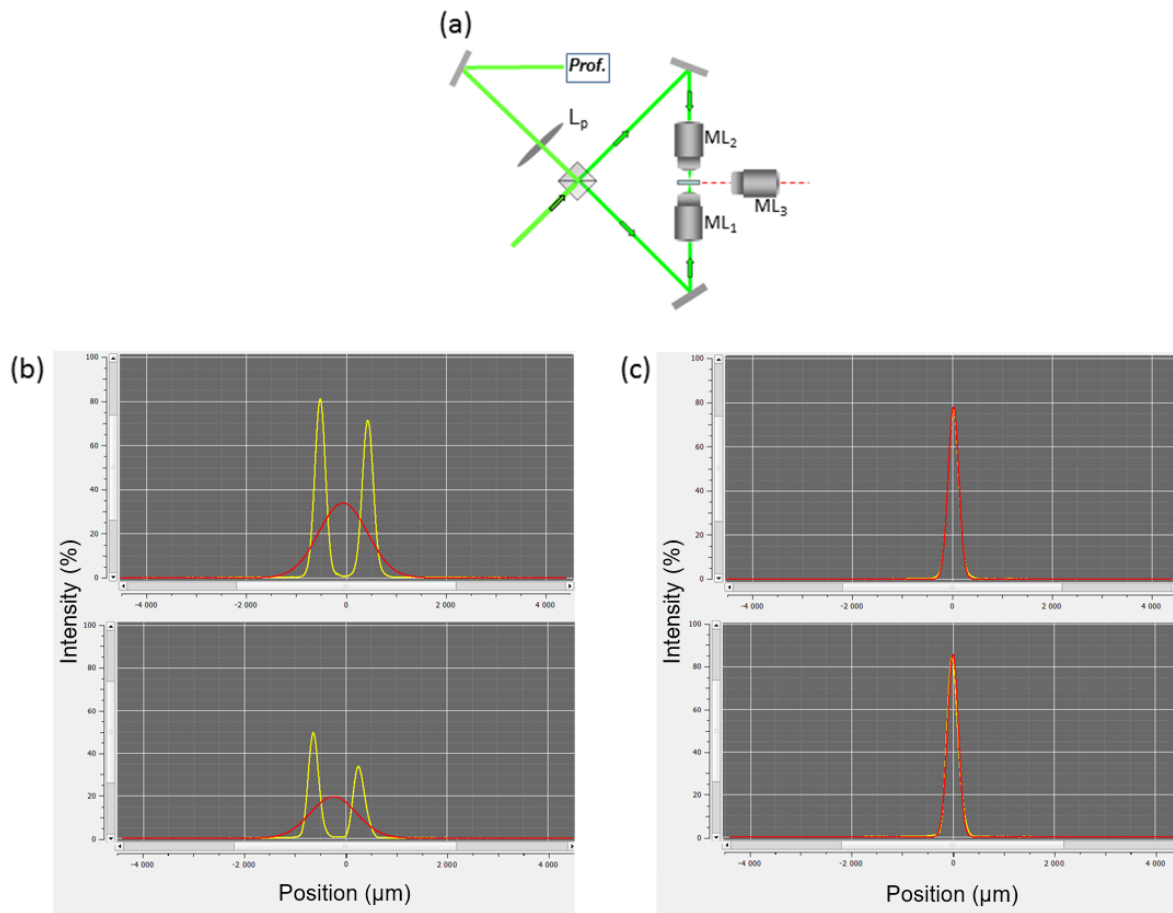


Figure 5: a) The beam cross-section in the observation plane (inside QC, from Figure 4) is imaged by the lens, L_p , onto the profilmeter, $Prof.$ ML_3 is a very long-working-distance objective used to image the levitated particle through the side wall of the cuvette. b) The two beams are misaligned, which is signalled by the two-peak structure shown in the intensity profile obtained using the Thorlabs BP209-VIS, with each peak representing either the up, or the down beam. c) The aligned beams, which is shown by the symmetrical Gaussian structure of the intensity profile, which is obtained after the necessary corrections.

ML_2 provides images of the sample viewed from the top. In many experiments, however, we observe the levitated particle both from the top and from the side, using ML_2 for the top view, and a third, long working-distance objective, ML_3 (Mitutoyo 50x, Working Distance = 23mm),

positioned to see particles through the side wall of the sample cuvette. Because the particle is generally positioned deeply inside the cuvette, and because the side wall strongly reduces the aperture of the imaging system in the vertical direction, images are of poor quality. Nevertheless, they are still exploitable enough to reveal the oscillations of ellipsoidal particles.

A-2.3. Single beam optical tweezer setup

The optical tweezer setup that was used in the work of this thesis is a commercial product provided by Elliot Scientific (United Kingdom). It is based on the well-known principles of optical trapping by a single tightly focused beam, see [8, 49].

The core of the setup consists of a laser source (IPG Photonics, YLR-10-LP, $\lambda_0 = 1070\text{nm}$, $P_{max} \approx 10\text{W}$), an optical arm (Elliot E3541) and an inverted microscope (Olympus IX73). The microscope turret is comprised of three objectives (20x, 40x and 100x). The 100x objective (Olympus UPlanFL N 100x, $NA = 1.3$) is used with its lens immersed in oil and has a very large numerical aperture, $NA = 1.30$. Only this objective can produce a tight enough focus for the beam to be able to achieve three-dimensional trapping of small particles. It also includes an iris diaphragm which allows the reduction of the aperture down to $NA = 0.6$. This function is useful for studying the stability of 3D trapping as a function of the beam aperture, as will be reported in Section A-3.5.3. A homemade scale was added onto the objective to indicate intermediate values of the aperture, between the extremes of 0.6 and 1.3. The calibration of this scale is studied in Appendix - Numerical aperture calibration.

The laser beam is guided through a single mode fibre which ends with a connector, so that it may propagate into the optical arm (Figure 5). The source is linearly polarized, and the direction of the polarisation can be tuned by utilising a half-wave plate (HWP).

The optical arm yields a wide laser beam, overfilling the aperture diaphragm (AD) at the bottom of the objective. Ideally, the laser intensity distribution should be uniform within the objective pupil. This is not possible in reality, without losing most of the power. In practice, overfilling means that the Gaussian beam cross-section is partially cut by the objective pupil. Consequently, the effective numerical aperture of the trapping beam is less than that of the objective (see the Appendix - Numerical aperture calibration).

Figure 5 shows the basic configuration, where the beam is coaxial with the objective axis. In this case, the beam is simply focused at point F, the front focus of the objective. Inside the

optical arm, the beam passes through an acousto-optic deflector (AO), the function of which is to deflect the beam by an angle, ζ , and to make it rotate around F' , the rear focal point of the objective. As a consequence, the beam still gets focused in the front focal plane, but at distance, $f_{ML} \cdot \zeta$, from the axis. This function allows us to move the optical trap centre within the observation plane very easily, simply by dragging the computer mouse.

However, a drawback of this feature is that the diffraction efficiency is poor ($\sim 1\%$), meaning that most of the laser power is lost. Moreover, the AO does not maintain the linear polarisation of the beam. Generally, the AO makes it so that the beam reaching the microscope objective is elliptically polarized. Whenever a linear polarisation is required, the setup has to be operated without the AO. In this case, we lose the ability to move the trap inside the observation plane, but the polarisation is well defined. As mentioned previously, by moving the half-wave plate, the polarisation can be oriented either perpendicular to the microscope symmetry plane, or parallel to it, which is necessary to be able to check the effect of polarisation on the particles.

Because of the poor diffraction efficiency of the AO, the laser power reaching the microscope objective, P_{MO} , is much smaller when the AO is in operation, than when it is not. To reduce this difference, a neutral density filter (Schott NG4 glass, with a transparency of 0.11) was added to the beam path, specifically between the M_1 and M_2 mirrors (see Figure 7), when operating the optical tweezers without the AO. Therefore, the experiments are respectively labeled as “AOoff-NGin”, or “AOin-NGoff”, depending on whether the AO is in operation with no neutral density filter, or vice versa. The value, P_{MO} , was measured as a function of the laser power at its source, P , by means of a Coherent FieldMax II power meter. This was done by removing the microscope objective and placing the power meter head above the microscope nosepiece. During the course of this calibration, it was noticed that the power of the beam diffracted by the AO was very sensitive to small changes in the beam direction, which is controlled with the mouse. Since the angular position of the AO can be finely tuned within the optical arm, by means of four small screws, the diffraction efficiency could be optimized through a systematic procedure; however, due to the delicate nature of this kind of procedure, and since there was always enough power in all our experiments (even with the $\sim 1\%$ diffraction efficiency), the optimization was not attempted as it was deemed unnecessary. Results of the measurement are indicated below:

$$P_{AOoff-NGin} = 72.15 \times 10^{-3} P \quad \text{A.8}$$

$$P_{AOin-NGoff} = 7.0 \times 10^{-3} P \quad \text{A.9}$$

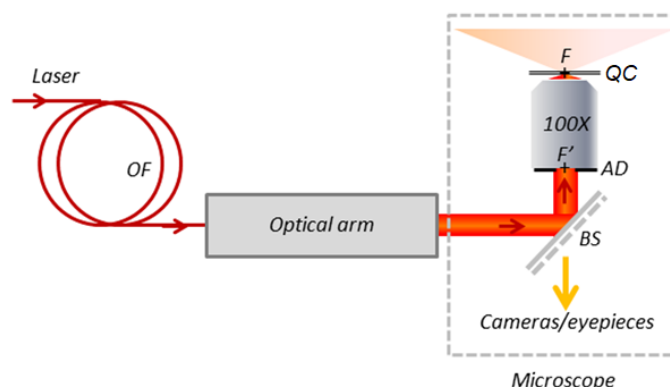
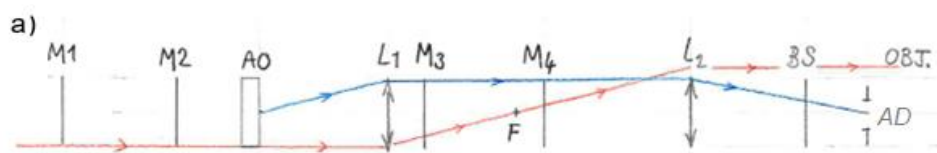


Figure 6: Diagram of the optical tweezer setup. OF is the optical fibre, BS is the beam-splitter, AD is the aperture diaphragm, QC is the quartz cuvette and F and F' are the front and rear foci of the microscope objective (100x), respectively. A film of immersion oil (not shown) bridges the gap between the objective and the lower side of the QC.



b)

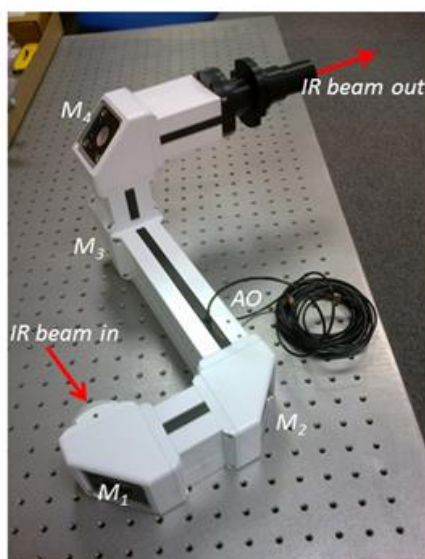


Figure 7: a) Sketch and b) photo of the Elliot optical arm (E3542). The sketch, a), is the unfolded representation of the composition of the optical arm. $M_{1,2,3,4}$ mark the positions of the mirrors along the optical path. As shown by the blue line, the role of lens L_1 is to conjugate the position of AO with the aperture diaphragm (AD) of the objective. The path followed by the laser beam is represented in red. The $L_{1,2}$ pair of lenses function as a telescope to control the width of the laser beam inside the microscope. Mirrors, $M_{1,2}$, have tuning screws to centre and direct the beam through the acousto-optic deflector. The end of the arm (the black tip in b)) is connected to the microscope through a video port. By tuning the screws of $M_{3,4}$, the beam may be centred within the microscope.

In addition to moving the position of the trap, the acousto-optic deflector can also be used in time-sharing mode to generate an array of traps. If the transit time between successive positions is short enough on the scale of the particle dynamics, then time sharing allows the formation of multiple effective traps.

The Elliot optical tweezer apparatus includes two video cameras, as well as dedicated software with user friendly graphic interfaces. During standard operation, both of these cameras are connected to a single video port, which is located at the bottom of the microscope body. The cameras share the light coming from the experiment using a beam splitter residing in a two-port connecting box. They are also fixed for optimum focusing of the microscope image, meaning that they show details of the front focal plane of the microscope objective, which is labelled as F in Figure 6.

The first camera (Basler), from now on dubbed, “CAM0”, is used to observe the sample, and the position of the trap(s). The infrared spot of the laser can be made visible by bringing one of the interfaces (quartz-water at the bottom, or water-glass at the top) in the focus of the microscope. The spot must have the characteristic aspect of an Airy diffraction pattern. A non-symmetrical spot means that a better tuning of the optical arm elements is necessary.

The second camera (Dalsa Genie), “CAM1”, captures images that are used by the Elliot particle tracking software. This tool has been designed to find and track the position of a spherical particle over time. When no external force is acting on the trapped particle, fluctuations in the particle position are due only to the thermal agitation (Brownian motion). In this case, the particle moves randomly around the centre of the laser spot. The software interface then provides histograms of the particle position, the time correlation function of the position, and the corresponding power spectrum. These data are used to calculate the trap stiffness within the horizontal, xy plane. A detailed description of the statistical analysis tools required for this can be found in the article by Gibson et al. [50], as well as the cited papers therein.

Despite having two cameras dedicated to observing the beam focal plane of the OT setup, it was also necessary to observe above or below that plane. This was not possible with CAM0 or CAM1, because their positions were fixed. The solution to this problem was to use the second video port of the microscope, which is located below the eyepieces, so that the camera could be moved to various distances from the tube lens, each corresponding to planes of different altitudes with respect to the beam waist plane, located, in theory, at F in Figure 6. The Basler camera was used to achieve this configuration, and was relabelled “CAM2”. The

images from this camera could now be focused above or below the beam waist plane freely. The values of the altitude shift were determined through a dedicated calibration procedure that allowed the range of $5\mu\text{m}$ above or below the laser focus to be accurately read using a homemade scale.

To change the altitude of the beam waist plane of the laser, the objective could be moved using the focusing knob of the microscope. This allowed the vertical movement of the observation plane within the sample cell, the altitude of which shall be denoted as, z_F . While in theory the laser focus should be located at F in Figure 6, in reality it is slightly above it, by about $2\mu\text{m}$, meaning that $z_{laser\ focus} - z_F \approx 2\mu\text{m}$. The focusing knob moves both simultaneously at the same rate, and is connected to a rotary encoder that enables the altitude to be known to within a $0.1\mu\text{m}$ uncertainty.

As will be explained in Section A-3.5, the altitude of the beam focus above the bottom interface ($z_{laser\ focus} - z_0$) of the cuvette is critical in determining the behaviour of a trapped ellipsoidal particle. Therefore, to be able to know this value, software developed by P. Merzeau enabled the displaying of the altitude at the bottom of each video frame, making it possible to know z_F at each point during the experiment. z_F is measured with respect to an arbitrary original altitude chosen by the experimenter, due to the way the rotary encoder works.

Contrary to the optical levitator setup, where a large space is available for the sample between the microscope objectives, optical trapping by a large aperture beam is restricted to a very short working distance of about 0.3mm for a $100\times$ objective. Because of this limitation, the sample cell has to be very thin. It is made of a microscope cover slip, approximately 0.17mm in thickness, and of a 1mm thick cover glass above it. These are separated by 0.1mm . There were frequent problems with the polystyrene particles sticking to the glass, so the glass cover slip was substituted for a quartz one, which prevented the sticking, at least for a short while (~ 1 hour). Initially, this was cleaned with sulfochromic acid and rinsed with pure water prior to the cell assembly; however, this did not always make it so that the particles did not stick. It was found that a simple rinse with methanol, ethanol and pure water was enough, and in fact a better way to prevent sticking. We tested different materials for the spacer, and estimated that glass did not perform better than a simple mylar sheet. The latter was simply rinsed with water before assembly.

The sample cell was moved horizontally, in the xy plane, using a motorised platform (Marzhauser Sensotech), which can be controlled by the experimenter with a joystick, the velocity of which can be tuned to be from nm s^{-1} to cm s^{-1} .

A-3. Experimental results

We start this section with a report on the optical levitation of spherical particles (Section A-3.1). As we will see, the spherical case is not as simple as it might be thought of a priori. Knowledge of the difficulties and limitations of measuring levitation forces with spheres is necessary before trying to deal with the more complicated problem of ellipsoids. In Section A-3.2.2, we report how the two-beam configuration adds unforeseen complexity to the static cases (where there is some Brownian motion, but no sustained oscillations) obtained with spheroidal particles.

Following this, Section A-3.3 is dedicated to the dynamical responses of spheroidal particles when they are illuminated by either one, or two beams. In this case, dynamical means that a particle constantly moves under the action of the laser beam(s). The different types of behaviours observed in one, and two-beam geometries within the optical levitator, both static and dynamic, are summarized in a state diagram in Section A-3.4.

Finally, Section A-3.5 is about the responses of ellipsoids in the OT geometry. As we will see, the very large aperture beam in that case provides stable, static three-dimensional trapping in the bulk of the water. However, bi-stable configurations and polar angle oscillations are observed when the particle is in contact to a cell boundary.

Our main observations are summarized in the conclusion, which is presented in Section A-6. The difference between nonlinear oscillations, observed in one- and two-beam levitation geometries, and noise-driven motion, including that observed with the optical tweezers, is also elaborated in this section.

A-3.1. Static equilibria of spheres

Levitation of a sphere is straightforward in practice. The experimenter first selects a particle at the cell bottom, and by moving the cell horizontally, brings it on the laser spot. Applying a few milliwatts of power is enough to make the particle lift up quickly. Equilibrium is reached by reducing the power to the value, P_{lev} , where the vertical radiation pressure force provided by the beam, F_z , exactly balances the buoyant weight of the particle, $\tilde{m}g$. In principle, F_z is proportional to the beam power:

$$F_z = f_z P$$

where,

$$f_z = \frac{dF_z}{dP} \quad \text{A.11}$$

The condition for equilibrium then reads:

$$\tilde{m}g = f_z \cdot P_{lev} \quad \text{A.12}$$

Here, $\tilde{m}g$ is known, given the particle density, ρ_p , and its radius, R_0 :

$$\tilde{m}g = \frac{4\pi}{3}(\rho_p - \rho_w)R_0^3g \quad \text{A.13}$$

with ρ_w as the density of water ($\rho_w = 1\text{gcm}^{-3}$), and g as the acceleration due to gravity. The term, $\rho_p - \rho_w$, which is the difference in density between the particle and the surrounding medium (in this case water), will from now on be denoted as, $\Delta\rho$.

In this part of the thesis, the results concerning the levitation of silica and PS spheres will be shown, as well as compared to GLMT calculations of f_z . This kind of comparison can be made because of the assumptions associated with Equations A.12 and A.13, namely:

- ❖ The only forces acting on the particle during equilibrium are from radiation pressure, F_z , and from gravity, $\tilde{m}g$. This supposes that there is no absorption of the laser light from the water, or from the particles, meaning that the possibility of thermally induced flows, which have the potential to perturb the equilibrium of the particle, are ignored.
- ❖ The optical force, F_z , is simply proportional to the laser power, so any nonlinear optical effects are not considered.

Firstly, the silica sphere experiments are addressed. These were used as a way to ensure that the procedures being done adhered to expectations, and were therefore safe to perform on the polystyrene particles. Silica spheres are known to be very smooth and highly transparent. Due to their high density, with $\Delta\rho \sim 1\text{gcm}^{-3}$, and comparatively low refractive index, $n_{silica} \approx 1.46$, these particles require a lot more power to be manipulated than their polystyrene counterparts. It is presumed that the silica spheres are not very sensitive to small disturbances such as Brownian motion, or parasitic flows within the water medium. On the contrary, PS

spheres are much less dense, with $\Delta\rho \approx 0.05\text{gcm}^{-3}$, and of the particles in the experiments, the biggest PS particles were in fact lighter than the much smaller silica spheres. The assumption is that PS particles would therefore be more sensitive to perturbations caused by the surrounding water medium, and it has also been measured that they may also be slightly absorbing [45]. These were also some points to verify.

A-3.1.1. Silica spheres

The silica spheres used here were provided by Bangs Laboratoires, with reference SS05003. The suspension was slightly polydisperse, with $R_0 \approx 2.37 \pm 10\mu\text{m}$.

The goal of the experiments with spheres is to measure the levitation power, P_{lev} , required to maintain the particle in equilibrium with gravity whilst in the bulk of a medium, which in this case is water. Specifically, the configuration that is mainly looked for is that of Figure 8 a), when the particle centre is within the beam waist of the laser, which is located at $z = 0$. In principle, this is the condition where the particle image should be sharpest and most focused. In reality, however, the OL setup does not provide a high-quality image of the particle due to the Zeiss X50 Epiplan objective not being corrected for imaging through a thick refractive medium, which in this case amounts to about 1mm of water and 1mm of quartz. This leads to the particle having slightly blurred boundaries on the video images, making it difficult to locate the altitude of the beam waist using the best focused image of the particle to an uncertainty lower than a few micrometres. The particle may therefore be either above or below the desired position, causing a potentially large error in the measurement of P_{lev} .

The error in P_{lev} is due to the dependence of the beam diameter, $2\omega(z)$, on the distance from the beam waist plane along the beam axis, z , as is illustrated in Figure 8. In Figure 8 a), the beam is narrow compared to the particle size, and so goes through the particle centre. Within a ray-optics description of this situation, where the density of rays describes the intensity of the beam, most rays are only weakly refracted. Consequently, the momentum transfer, and therefore the levitation force, is low. In Figure 8 b), the beam that the particle is exposed to is wider; hence, keeping with the aforementioned optics approximation, many more rays hit the particle away from its symmetry axis, and are then strongly refracted. Momentum transfer then becomes more efficient, and f_z increases, making P_{lev} smaller in the configurations of Figure 8 b) and c), than that in a). This dependence of f_z on z was realised and explained in the early works of Ashkin and Roosen during the 1970s. Using a ray optics approximated representation of a Gaussian laser beam, Roosen [51] found that the maximum f_z for dielectric spheres

occurs when $\frac{R_0}{\omega(z)} \approx 1$, meaning that the momentum transfer is most efficient when the beam and particle radii are approximately the same. This is highlighted in Figure 9. The computation was performed with the GLMT software, ABSphere [28], for the case of a small silica sphere such as the ones which that were used in the OL experiments, with $R_0 = 2.37\mu\text{m}$, and a laser with the small beam waist of $\omega_0 \approx 1.7\mu\text{m}$. The refractive index was taken to be $n_{\text{silica}} = 1.46$, as given by [52]. GLMT takes into account the wave nature of light and is close to the exact solution of the problem. A brief description of this model will be given in Section B-2.2.

Figure 9 a) shows that the levitation force is minimal near the beam waist plane, with $f_{z,\text{min}} \approx 0.0554\text{pNmW}^{-1}$ at $z_{\text{min}} \approx 3.6\mu\text{m}$. The levitation becomes much more efficient away from this value of z , with the maximum being, $f_{z,\text{max1}} \approx 0.134\text{pNmW}^{-1}$, which occurs when the particle is far below the beam waist, at $z_{\text{max1}} \approx -34\mu\text{m}$. Another maximum, of a slightly lower amplitude, $f_{z,\text{max2}} \approx 0.102\text{pNmW}^{-1}$, occurs on the opposite side of the beam waist, at $z_{\text{max2}} \approx 37\mu\text{m}$.

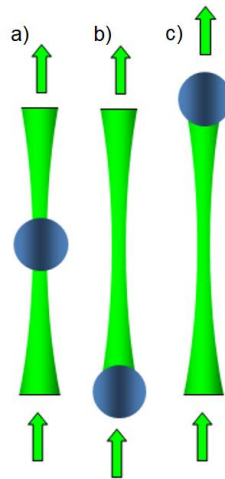


Figure 8: Levitation of a dielectric spherical particle can be achieved when it is situated at different beam altitudes, with respect to the beam waist. a) The levitation power is maximal when $z \approx 0$, and it is lower for the configurations in b) and c).

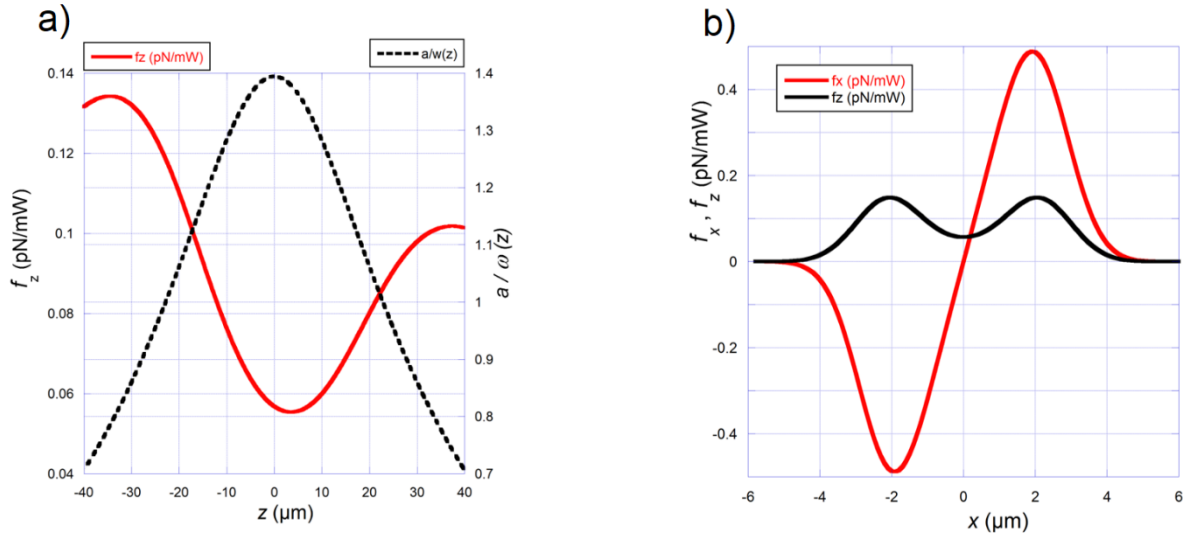


Figure 9: a) The axial optical force component, f_z , calculated with ABSphere for a spherical silica particle of the same specifications as those used in the experiments. The particle is taken to be on-axis ($x = y = 0$). The solid red line represents the variation of the vertical force against the particle altitude, while the black dotted line shows the $\frac{R_0}{\omega(z)}$ ratio at a given altitude. b) The effect of particle off-centring in the x -axis on f_z and f_x , when $z = 0$. Calculation parameters: $R_0 = 2.37\mu\text{m}$, $\omega_0 = 1.70\mu\text{m}$, $n_{\text{silica}} = 1.46$.

In the silica particle example of Figure 9 the levitation at the beam waist plane is far from efficient, because ω_0 is a lot smaller than R_0 , with $\frac{R_0}{\omega_0} = 1.39$ at $z = 0$. The beam radius varies with z according to:

$$\omega(z) = \omega_0 \sqrt{1 + \left(\frac{z}{l}\right)^2} \quad \text{A.14}$$

where l is the Rayleigh length of Equation A.4, which in the case of Figure 9 is $23.5\mu\text{m}$. The black dotted line in Figure 9 a) shows the variation of $\frac{R_0}{\omega(z)}$ along the beam axis, in z , with the corresponding axial force represented by the solid red line. It can be seen that both maxima of f_z occur when $\frac{R_0}{\omega(z)} \approx 0.8$, not far from the expected result of $R_0 \sim \omega(z)$. The fact that the maxima calculated by GLMT have different amplitudes is not something predicted by the simple analysis based on the $\frac{R_0}{\omega(z)}$ ratio. In fact, the observed asymmetry is due to the local wave curvature, which is positive for $z < 0$ (when the beam is converging) and negative for $z > 0$ (when the beam is diverging). f_z is minimal close to the beam waist, when $z \approx 3.6\mu\text{m}$, which is presumed to also be caused by the wave curvature.

Figure 9 b) shows the variation of the axial and transverse components of the optical force when the particle is located at the beam waist plane, with $z = 0$, but is off-centred along the x -axis. It should be noted that the slope of the red curve, representing f_x , indicates that the particle gets stably trapped onto the laser axis, as is expected. The axial force, f_z , is largest when the shift along x is approximately $2\mu\text{m}$, but due to the effect of the transverse force, f_x , the particle should predominantly reside in the on-axis configuration, at $x = 0$. The effective axial force amplitude is therefore that for $x \approx 0\mu\text{m}$, which is $f_z \approx 0.0554\text{pNmW}^{-1}$. Everything discussed so far concerning f_x , also holds true for its y -axis counterpart, f_y .

Theoretical values of the levitation power were obtained using Equations A.12 and A.13, with $R_0 = 2.37\mu\text{m}$ and $\rho_p^{Si} = 1.91\text{gcm}^{-3}$, which was determined as the average from sedimentation experiments that utilised the different particle sedimentation velocities, as well as approximated values of R_0 based on microscope images. From this information, the deduced particle buoyant weight was $\tilde{m}g = 0.498\text{pN}$. Therefore, the calculated levitation power values, P_{lev} , corresponding to the extrema of f_z are: $P_{lev}(z \approx 0) = 9.0\text{mW}$, $P_{lev}(z_{max1}) = 3.72\text{mW}$ and $P_{lev}(z_{max2}) = 4.89\text{mW}$.

The existence of such extrema was experimentally verified. During the experiments, the particles were observed both from the top and from the side. The side view is very useful, since it tells us whether the particle is moving up or down, with a resolution of around $1\mu\text{m}$.

The experiments proceed by first levitating the particle near bulk, and bringing it to the beam waist plane, or at least what is thought to be the beam waist based on the sharpness of the top view image of the particle. Then, the power is decreased until the particle is stable along z . Next, the power continues to be slowly decreased until the lowest possible power of a stable levitation state is found. This will be denoted as, P_{lev}^{min} , which is essentially equivalent to the theoretical value, $P_{lev}(z_{max1})$. Decreasing the laser power lower than P_{lev}^{min} makes the particle fall indefinitely. Once, P_{lev}^{min} has been recorder, the particle is lifted once more, with the power being gradually increased. The particle moves through a series of intermediate equilibrium positions in z , with this finishing at the maximum possible power able to maintain a stable levitation, P_{lev}^{max} . Anything above that power sends the particle upward indefinitely. In principle, the altitude corresponding to P_{lev}^{max} is the beam waist plane, $z = 0$. In general, it was observed that the respective top view image at this power was not exactly that which produces the optimal sharpness of the particle. In fact, the sharpest image was obtained with the particle a

few micrometres below the presumed beam waist plane. The results of experiments performed with five different particles have been gathered in Table 1.

P_{lev}^{min} (mW)	5.30	5.03	4.35	3.70	3.20
P_{lev}^{max} (mW)	10.6	9.34	7.08	8.20	8.18
v_{sed} (μms^{-1})	12.00	11.55	11.57	10.44	10.75

Table 1: The maximum and minimum value of the levitation power for silica spheres, and their corresponding sedimentation velocities. The beam waist radius is $\omega_0 \approx 1.7\mu\text{m}$.

The third row in Table 1 gives the sedimentation velocity of each particle. As was mentioned in Section A-2.1, optical levitation can be used as a convenient tool to perform sedimentation experiments by bringing the particle somewhere within the bulk of the water and dropping it. The particle then slowly falls, with a constant sedimentation velocity given by Equation A.3, where η is the shear viscosity of water (which is $\approx 10^{-3}\text{Pas}$ when $T = 20^\circ\text{C}$). The sedimentation velocity, v_{sed} , can be measured by tracking the descent of the particle with an uncertainty of less than 1%. If $\Delta\rho$ is known, R_0 can be deduced with a better accuracy than from the microscope image of the particle. Conversely, one can measure $\Delta\rho$ if R_0 is known with sufficient accuracy.

The values in Table 1 have been obtained with particles of different sizes. It may therefore seem natural to gather the data into a graph of P_{lev} against R_0 , and then calculate the GLMT counterpart for comparison. However, as aforementioned, the values of R_0 are not known with sufficient accuracy. Instead of its size, each particle can be more accurately represented by its sedimentation velocity. From Equations A.3, A.12 and A.13, it can be seen that both, P_{lev} and v_{sed} , are proportional to $\Delta\rho$. Therefore, a more accurate graph may be one of P_{lev} against v_{sed} . Thusly, if there is disagreement between the experimental and GLMT values of P_{lev} , this cannot be related to the density, because changing the value of $\Delta\rho$ cannot change the ratio between the experimental and GLMT levitation powers for a given v_{sed} . This leaves only the complex refractive index of the particle as an adjustable parameter in the GLMT calculation.

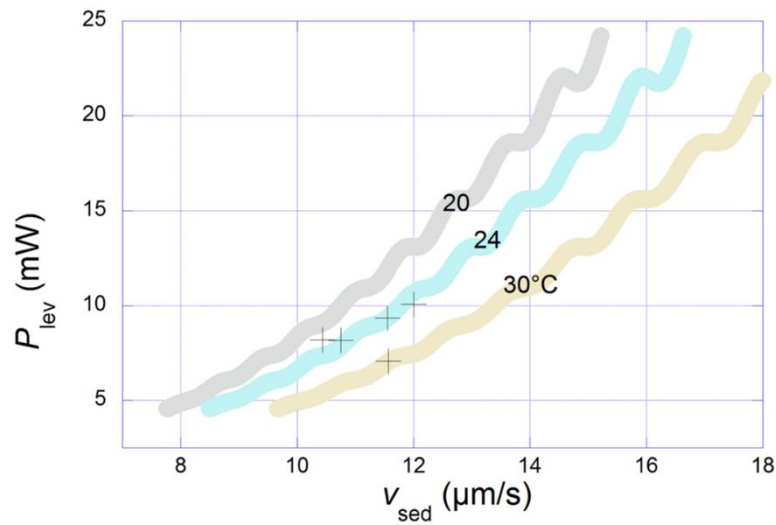


Figure 10: A graph comparing the theoretical and experimental levitation powers for silica spheres. The GLMT values of the levitation power are represented by the coloured lines, and the experimental counterparts are shown by the crosses. The temperature corresponding to each coloured curve is indicated on the graph. Calculation parameter: $n_{silica} = 1.46$ (with the imaginary part being 0), $\omega_0 = 1.65\mu\text{m}$, and $\eta = 1.020, 0.933, 0.820\text{mPas}$ for $T = 20, 24, 30^\circ\text{C}$, respectively.

The aforementioned graph has been plotted in Figure 10 to compare the GLMT and experimental values of the levitation powers. Due to the sensitivity of the viscosity of water to the temperature ($\frac{d\eta}{dT} \sim 0.02\text{mPasK}^{-1}$), it must be specified in the simulation. This dependence has a measurable influence on the sedimentation velocities of the particles, as can clearly be seen in Figure 10. Note that the undulations along each curve are a symptom of the wave nature of light, since coherent light creates interference within the volume and along the surface of the particle, which then has visible consequences on the momentum transfer.

The sample temperature of each experiment is not specified accurately, since the cuvette was not temperature controlled. Therefore, the temperature was taken to be approximately that of the laboratory, which usually varied between 24°C and 30°C , depending on the meteorological conditions and the activities inside the experiment room.

Figure 10 indicates that the GLMT values of P_{lev} reasonably match the experimental ones within each given temperature interval. This agreement supports the previously made assumptions that nothing other than radiation pressure and gravity is responsible for the particle equilibrium, and that F_z is proportional to the laser power.

Using reasoning initially proposed by [53, 54], if both the up and the down beams are exactly superposed, then the geometry is symmetrical along the z -axis. This means that at the beam waist plane, the equation for the levitational equilibrium of a spherical particle is:

$$\tilde{m}g = f_{z=0}(P_{\uparrow} - P_{\downarrow}) \quad \text{A.15}$$

This equation holds true no matter what total power, $P_{tot} = P_{\uparrow} + P_{\downarrow}$, is applied to the particle.

The total power was therefore increased to much higher values for two-beam experiments, than it was for levitations using only a single beam. It was then necessary to verify if the particle remains stably levitated when $P_{\uparrow} - P_{\downarrow} = P_{lev}$, where P_{lev} is the levitation power obtained with only the up-beam in operation.

In practice, P_{tot} was increased in sizeable increments, whilst making sure that the power repartition of the two opposing lasers was adjusted such that the difference between them stayed constant, at approximately the value of P_{lev} . The particle was then monitored to make sure that it remained in levitation at around the altitude of the beam waist, $z \approx 0$. The results for three silica particles, with a beam waist of $\omega_0 \approx 1.7\mu\text{m}$, are gathered in Figure 11, where the difference in powers, $P_{\uparrow} - P_{\downarrow}$, has been plotted against the total power, $P_{\uparrow} + P_{\downarrow}$. If all assumptions about the model are correct, the graph should show a horizontal straight line, and as can be seen from Figure 11, this is indeed the outcome, within the experimental uncertainty.

It is worthwhile discussing the uncertainty within this series of seemingly basic experiments. This kind of configuration can become severely biased as a result of asymmetry in the two-beam setup. The asymmetry may be due to a lack of accuracy in the beam superposition, or for the particle to be too far above or below the beam waist plane, or both. Another potential source of asymmetry is an error in the power calibration, which would result in different values for the calibration coefficients for the up and down beams, leading to the wrong beam powers being recorded. Another reason for the wrong beam powers to be recorded would be an offset in the half-wave plate ($\lambda/2$ in Figure 4) that has not been accounted for. Whatever the cause, or causes for it may be, an asymmetrical system would become apparent with an erroneous slope in graphs such as the one in Figure 11. For example, a finite positive slope of the graph is a clear indication of asymmetry, while on the other hand, a negative slope may be due to both an asymmetry, or to heating of the particle due to absorption [54].

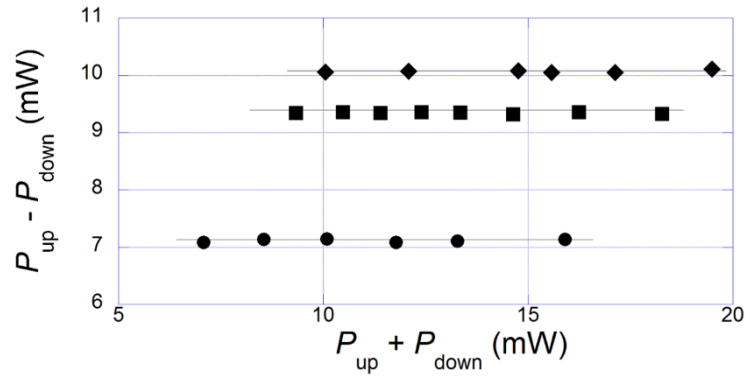


Figure 11: The power difference against the total power during a two-beam levitation experiment for three different silica particles.

In perfect conditions, this kind of experiment is in fact useful in the detection of a source of absorption, either by the material constituting the particle, or by the fluid around it. If a non-negligible fraction of the laser power is absorbed, the energy dissipates as heat, which is then transferred to the fluid, creating convective flow. This corresponds to a hydrodynamic drag force F_{hydro} , which acts on the particle, and is involved in the case of particle equilibrium alongside F_z and $\tilde{m}g$. The negative slope this causes in graphs such as the one in Figure 11 may be so large, that $P_{\uparrow} - P_{\downarrow}$ may become negative at high total power [54]. In that case, the particle is levitated even if more power is partitioned to the down beam than in the up beam, culminating in quite a counter intuitive scenario.

In conclusion, the measured levitation powers of silica spheres are close to the predictions made using the GLMT simulation. Experiments with both, the one and two-beam configurations confirmed that the radiation pressure force is simply proportional to the laser power. These tests do not detect any absorption by the particles, meaning that the refractive index, n_{silica} , is purely real.

A-3.1.2. Polystyrene spheres

The other type of spheres that were used for levitation experiments in the OL were larger ($\approx 5\mu\text{m}$) PS particles provided by Polysciences. The polydispersity of the size was around 10%, according to the manufacturer. The particles were made of a copolymer consisting of polystyrene and divinylbenzene (used for cross-linking). The technical data sheet provided alongside the particles indicates that the particle density is, $\rho_p^{PS} = 1.05\text{gcm}^{-3}$, with a refractive index of $n_{PS} = 1.59$.

Experimental results

Levitation experiments were carried out with two values of the beam waist radius, $\omega_0 \approx 1.7\mu\text{m}$ and $\omega_0 \approx 3.6\mu\text{m}$.

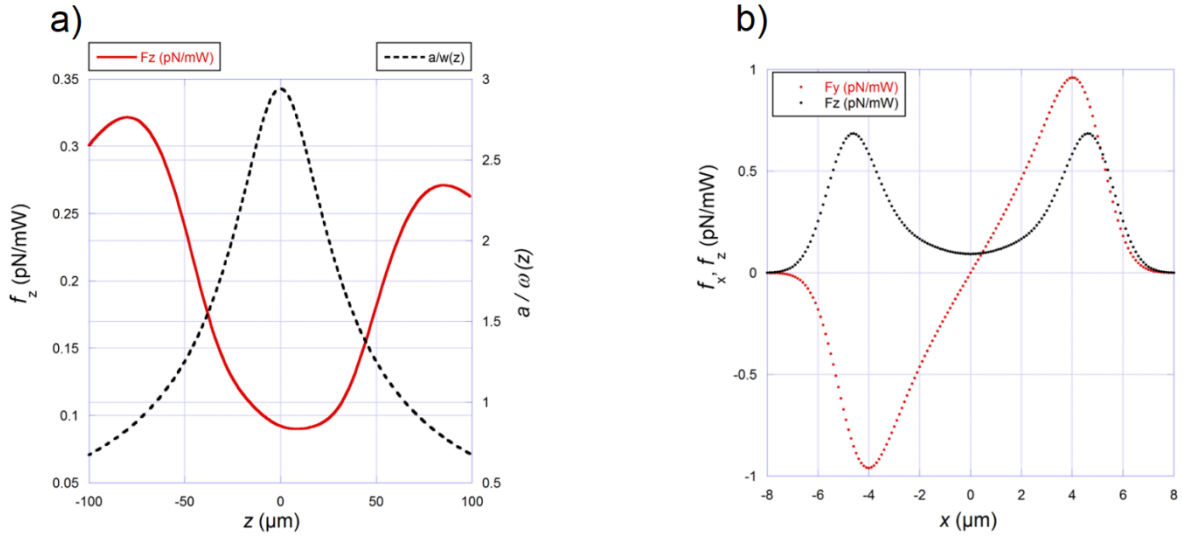


Figure 12: GLMT simulation of a levitated PS sphere in water, with the particle taken to be on the beam axis, ($x = y = 0$). a) The red line signifies the variation of the vertical force with the particle altitude ($z = 0$ when the particle centre is at the beam waist plane). The black dotted line represents the $\frac{R_0}{\omega(z)}$ ratio. b) The effect of particle off-centring on the vertical and horizontal forces when $z = 0$. Calculation parameters: $R_0 = 5\mu\text{m}$ and $\omega_0 = 1.70\mu\text{m}$.

The GLMT results for the small beam waist ($\omega_0 \approx 1.7\mu\text{m}$) are displayed in Figure 12. The aforementioned values of the density and refractive index were used for the calculation, with the particle buoyant weight, for a sphere of radius $R_0 \approx 5\mu\text{m}$, as $\tilde{m}g \approx 0.2568\text{pN}$.

Unsurprisingly, the trends are similar to those obtained with silica spheres. The levitation force goes through a minimum, $f_{z,min} \approx 0.090\text{pNmW}^{-1}$, near the beam waist plane, at $z_{min} \approx 9\mu\text{m}$. Again, the levitation becomes much more efficient at some distance from the beam waist plane. In this case, the greater maximum, $f_{z,max1} \approx 0.323\text{pNmW}^{-1}$, occurs when the particle is at $z_{max1} \approx -81\mu\text{m}$, with the second maximum, of slightly lower amplitude, occurring at $z_{max2} \approx 85\mu\text{m}$, with a levitation force of $f_{z,max2} \approx 0.271\text{pNmW}^{-1}$.

Both of these maxima coincide with $\frac{R_0}{\omega(z)} \approx 0.8$, similarly to the silica spheres. It is worth emphasising that both, z_{max1} and z_{max2} are very large distances, at least on the scale of a particle, and are both well beyond the plausible error in localising the beam waist plane, which is $\pm 20\mu\text{m}$ at worst. However, the variation in f_z within this interval is not negligible, $0.090 \leq f_z \leq 0.117\text{pNmW}^{-1}$. Consequently, the effective levitation power recorded by the

experimenter should be slightly lower than the theoretical one, with $P_{lev} = 2.85\text{mW}$ when $z \approx 0$.

The theoretical GLMT results from the previous paragraph were obtained by taking a particle radius of $R_0 = 5\mu\text{m}$; however, in reality the suspension was somewhat polydisperse. To illustrate the effect that polydispersity may have on the levitation power, Figure 13 shows the beam waist ($z = 0$) levitation powers for particles with radii ranging from 4 to $6\mu\text{m}$, which is a far larger size range than exists in the particles used in the experiments. The graph shows characteristic undulations of the same nature as those previously noted with the silica particles. As can be seen from the graph, a small difference in R_0 may result in a significant difference in P_{lev} . For example, for $R_0 = 4.95\mu\text{m}$, $P_{lev} = 2.16\text{mW}$, yet when $R_0 = 4.96\mu\text{m}$, $P_{lev} = 2.80\text{mW}$. Consequently, a strict comparison with GLMT values would make sense only if the particle radii can be determined within around $\pm 0.01\mu\text{m}$, which is quite elusive.

Based on Figure 13, an overall uncertainty of the predicted value of P_{lev} can be estimated. By combining the effect of interference, and that of the potential z shift of $\pm 20\mu\text{m}$, it can be stated that for $z \approx 0$, $P_{lev} = 2.4 \pm 0.4\text{mW}$ at worst.

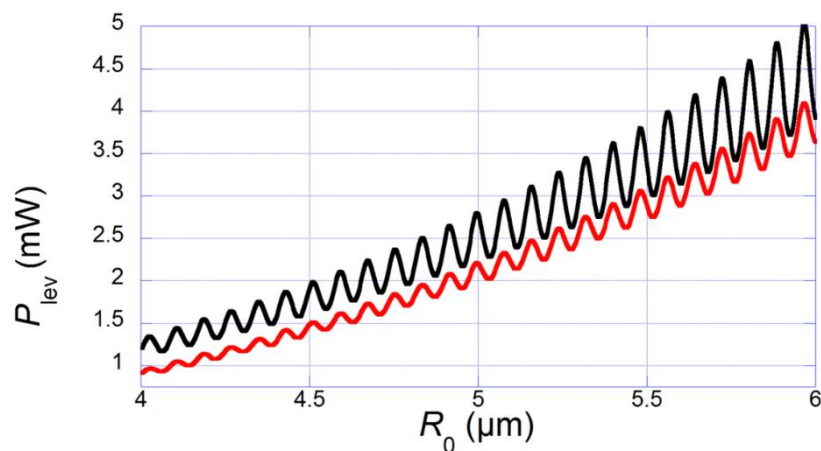


Figure 13: GLMT levitation powers against different PS particle radii for $z = 0\mu\text{m}$ (the black curve), and for $z = -20\mu\text{m}$ (the red line), with $\omega_0 = 1.70\mu\text{m}$.

Figure 12 b) indicates that lateral off-centring increases f_z , which is expected whenever the particle radius is larger than the local beam radius. However, both for the PS and the silica spheres, off-axis excursions are very small, $\ll 1\mu\text{m}$. Therefore, the effect of Brownian off-axis fluctuations should be negligible, and as such, does not modify the estimated levitation power.

Figure 14 shows the experimental results of the PS particles that were levitated with a beam waist of $\omega_0 \approx 1.7\mu\text{m}$, as compared to the results obtained using GLMT. Much like its silica counterpart, this graph also indicates the levitation power against the sedimentation velocity, with the additional variable of temperature. Clearly, experimental values for the levitation power at the beam waist are lower than the theoretical predictions, with the differences often being larger than the estimate of the uncertainty previously calculated for the predicted values.

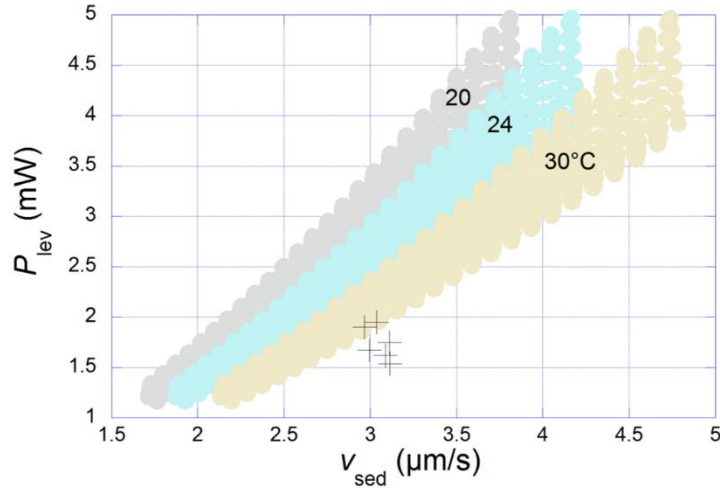


Figure 14: The theoretical (the coloured lines) and experimental (the crosses) values of the levitation power for PS particles, with temperature values indicated on the graph. Calculation parameters: $n_{PS} = 1.59$ (with the imaginary part being 0), $\omega_0 = 1.70\mu\text{m}$, and $\eta = 1.020, 0.933, 0.820\text{mPas}$ for $T = 20, 24, 30^\circ\text{C}$, respectively.

Similar experiments were carried out using a wider beam waist, namely $\omega_0 \approx 3.6\mu\text{m}$. Since increasing the beam waist brings it closer to the radii of the PS particles, this has the effect of improving the levitation efficiency. Therefore, the levitation power is expected to be lower than that with the smaller beam waist of $\omega_0 \approx 1.7\mu\text{m}$, which is in fact something that is confirmed by the GLMT calculations, as can be seen in Figure 15.

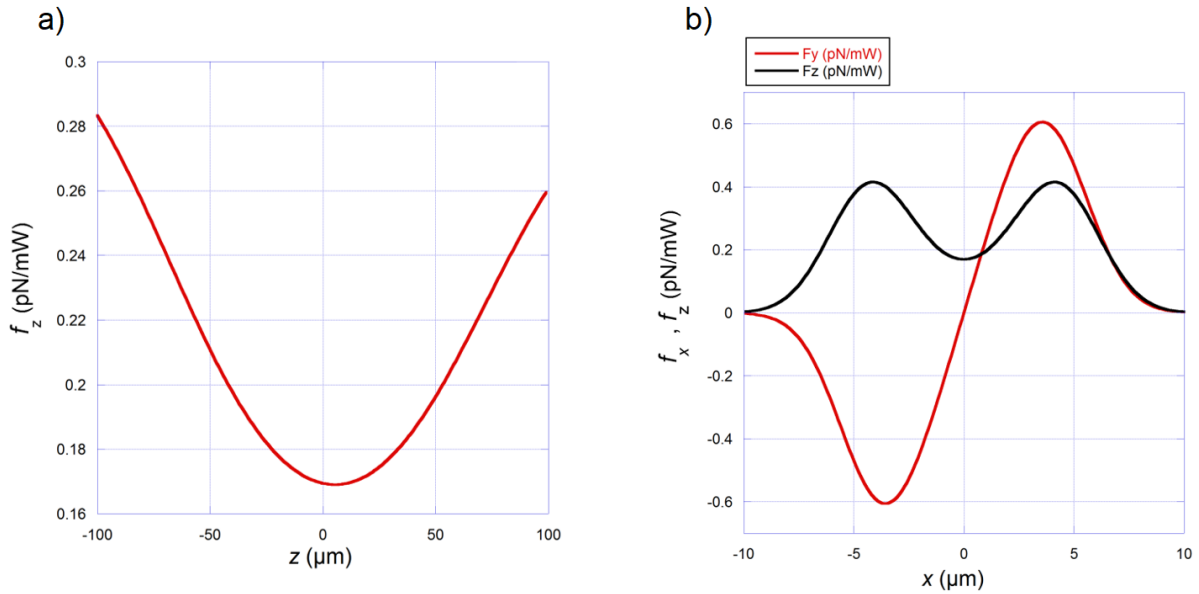


Figure 15: The GLMT levitation force calculation for a $R_0 = 5\mu\text{m}$ PS sphere in water, with $\omega_0 \approx 1.7\mu\text{m}$, for the on-axis case of $x = y = 0$. a) The red line shows the variation of the vertical force against the particle altitude, with $z = 0$ being the altitude when the particle centre is at the beam waist plane. b) The effect of lateral off-centring of the particle on the vertical and horizontal levitation forces, when $z = 0$.

Due to the large value of the beam waist radius, the Rayleigh length is very large, with $l \approx 97\mu\text{m}$. Consequently, both maxima of the levitation force are very far from the beam waist plane, completely away from the previously mentioned $\pm 20\mu\text{m}$ interval along z , and much bigger than the size of the particle. Following the same reasoning as for the smaller beam waist radius of $\omega_0 = 1.70\mu\text{m}$, the predicted levitation power for $\omega_0 = 3.6\mu\text{m}$ can be estimated as $P_{lev} = 1.40 \pm 0.1\text{mW}$ for a PS sphere of radius $R_0 \approx 5\mu\text{m}$, at $z \approx 0\mu\text{m}$.

Figure 16 shows the experimental values obtained with the beam waist radius of $\omega_0 \approx 3.6\mu\text{m}$ alongside the equivalent GLMT predictions, to make a graph of P_{lev} against v_{sed} . As before, temperature has also been included as a factor, and the graph shows that the experimental levitation powers match the $T = 30^\circ\text{C}$ branch reasonably well, with this actually being the room temperature of the laboratory at the time.

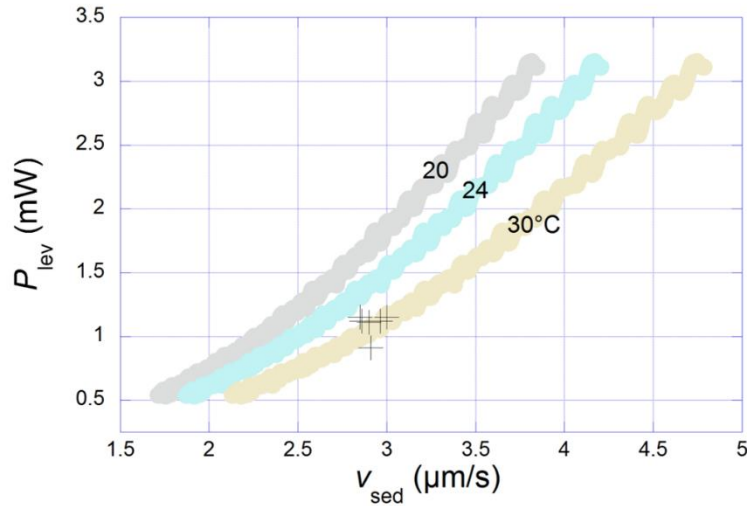


Figure 16: The theoretical GLTM (the coloured lines) and experimental (the crosses) values of the levitation power for PS particles of radius, $R_0 \approx 5\mu\text{m}$, with the temperature values indicated in the graph. Calculation parameters: $n_{PS} = 1.59$ (with the imaginary component being 0), $\omega_0 = 3.60\mu\text{m}$ and $\eta = 1.020, 0.933, 0.820\text{mPas}$ for $T = 20, 24, 30^\circ\text{C}$, respectively.

A-3.2. Static equilibria of spheroids

A-3.2.1. Single-beam levitation

When performing single-beam levitation experiments, only the up-beam is used. The spheroid particles are shaped from polystyrene spheres of radius, $R_0 \approx 5\mu\text{m}$, as explained in Section A-2.1.

The first steps of the levitation experiment are the same as those for spheres. It starts with the capture of a particle that has sedimented at the bottom of the cuvette. Levitation of low- k spheroids is fairly simple. Once exposed to the up-beam, the particle lines up its longest axis with the axis of the beam, and starts its ascension (provided the power of the laser is greater than the levitation power, P_{lev}). The particle may be elevated continuously until it makes contact with the cuvette ceiling, where it remains vertical. On the contrary, levitating high- k spheroids is more delicate, since these particles do not keep to the beam axis, and instead permanently oscillate around it. This is discussed in Section A-3.3.1.

As discussed above, there are no oscillations for low- k spheroids ($k \lesssim 4$) when using the beam waist radii, $\omega_0 \approx 1.7\mu\text{m}$ and $\omega_0 \approx 3.6\mu\text{m}$, with only one beam. This means that the levitation

power for such spheroids can be measured. In the experiments that were performed, the altitude of the quartz cell was tuned so that the observation plane is within the bulk of the water, roughly midway between the cell bottom and ceiling. The particles are then manipulated around this altitude, where each is levitated until it is as focused as possible. In such conditions, the particle centre is approximately at the beam waist plane. Equilibrium is achieved when the radiation pressure force from the beam exactly balances the buoyant weight of the particle. All the other forces are balanced due to symmetry, and the particle stays locked onto the beam, with its longest axis lying vertically along that of the laser (see Figure 3 b)). This system is not strictly immobile, due to thermal agitation, and shows some Brownian motion in the form of random changes in position and orientation. However, these motions have small amplitudes compared to the particle and beam sizes ($\ll 1\mu\text{m}$ displacement and $< 5^\circ$ tilt).

The vertical equilibrium is unstable, but can be easily maintained through the application of small corrections to the laser power. The value of the experimental levitation power, P_{lev} , can then be easily read out, and the experiments repeated for other particles with $k \lesssim 4$. The results have been compiled in Figure 17 for particles of increasing aspect ratio — specifically for the range $1 \leq k \lesssim 4$.

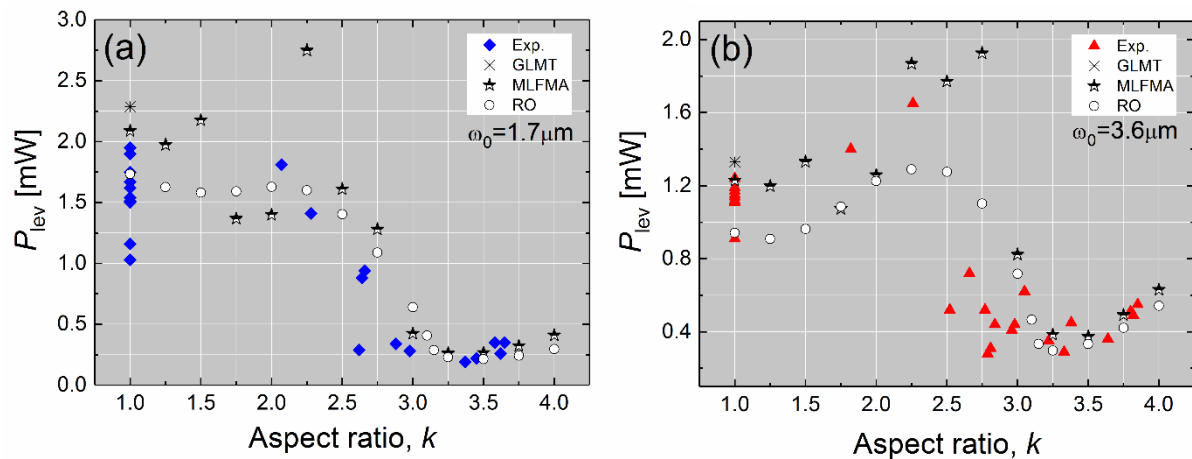


Figure 17: The levitation power, P_{lev} , as a function of the particle aspect ratio, k , (obtained with the up-beam only configuration) is shown here, with a comparison between experimental and theoretical data obtained for two different beam waist values: (a) $\omega_0 \approx 1.7\mu\text{m}$ and (b) $\omega_0 \approx 3.6\mu\text{m}$. The theoretical data was derived using GLMT, MLFMA and RO (see Sections A-4 and B-2 for details). We see that the variations of P_{lev} with respect to k are not smooth, as well as the fact that P_{lev} decreases significantly for $k \geq 2.5$.

In the case where $\omega_0 \approx 3.6\mu\text{m}$, P_{lev} clearly increases at first, as the particle stops resembling a sphere ($k > 1$), but then steeply drops when $k \geq 2.5$. The levitation power goes through a minimum at $k \sim 3.5$. A similar drop in P_{lev} can be noticed with the more focused beam, where

$\omega_0 \approx 1.7\mu\text{m}$; however, there is no clear variation in the first segment of the graph ($1 \leq k \leq 2.5$).

In addition to the experimental data, Figure 17 also shows computed values of P_{lev} based on different theoretical models. These results will be elaborated upon in Section A-5. As a preliminary comment, we see that both the experimental and computed values are scattered, but do show the same tendency.

A-3.2.2. Two-beam static equilibria

Optical manipulation of high- k spheroids is delicate when using a small beam waist relative to the particle size, as has been previously mentioned. This is because such particles escape the beam laterally when exposed to the laser, after which they come back across the beam, and repeat this motion indefinitely to form an oscillatory pattern. Levitating a high- k spheroid to the ceiling of the cuvette requires frequent feedback from the experimenter in order to keep the particle close to the beam axis. The down-beam is usually switched on when the particle is in contact to the top water-quartz interface (Figure 4 c)). We then observe the particle behaviour as the power ratio is varied, whilst the total power remains constant. In some of the experiments, the down-beam was turned on as the particle was being levitated in the bulk (away from the sample boundaries (Figure 4 b))). In this case, stabilising the particle height demands a delicate balance between P_{\uparrow} and P_{\downarrow} . Therefore, for practical convenience, most of the experiments were conducted in contact to the ceiling of the cuvette (Figure 4 c)), since this allows a greater range of laser power ratios to be explored without the problem of the particle moving away from the focus. Previous experiments have shown that having the particle in contact to the interface does not qualitatively affect its observed behaviour [35, 36, 37].

Using both beams in the levitator setup detailed in Section A-2.2, it is possible to maintain a particle of any of the tested aspect ratios in static equilibrium. However, this kind of equilibrium markedly differs from that encountered in the one-beam levitation case (Section A-3.2.1), which can only be achieved with low- k spheroids. It was found, unexpectedly, that when the second (down) beam is introduced to the system, both low- and high- k particles can be stably trapped in a tilted and off-centred position with respect to the beam axis, as sketched in Figure 18 a). Such states occur both at the water-quartz interface and in bulk water, although, as aforementioned, most experiments were carried out in the former of those cases. For given values of k and P_{tot} , the off-centring distance with respect to the beam axis, Δr , increases as the power ratio, ε , becomes higher, while the tilt angle, θ , remains roughly constant (see Figure

18 b)). There are still some differences between low- and high- k particles when they are in this state. High- k particles always have their top tip centred on the beam axis, with the other tip pointing away, whilst low- k particles display the opposite behaviour, as shown in Figure 19. These non-trivial configurations actually occur for a range of particle aspect and beam power ratios, as will be seen in Section A-3.4. They emerge as one of the salient new features of our study, and are very useful for modelling purposes due to equilibrium being reached despite the lack of symmetry.

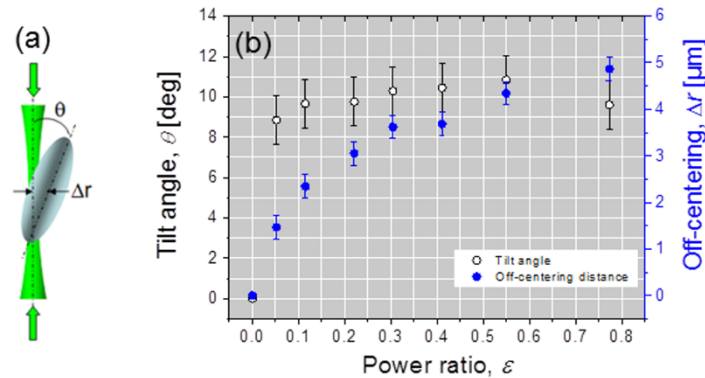


Figure 18: (a) A schematic illustration of a static oblique configuration characterized by the tilt angle, θ , and the off-centering distance, Δr . (b) The graph is showing Δr as an increasing function of the power ratio, ϵ , while θ remains roughly constant. Parameters: $k = 3.3$, $P_{tot} = 4mW$, $\omega_0 \approx 1.7\mu\text{m}$.

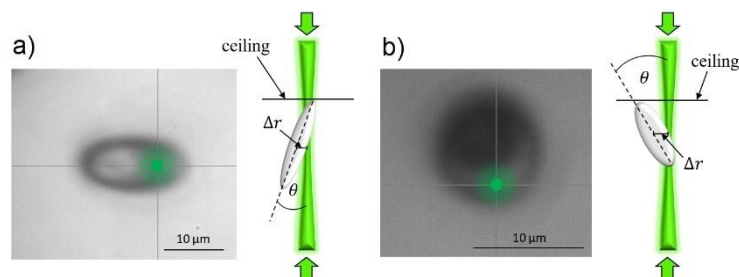


Figure 19: Optical microscopy images and corresponding schematics showing the static, tilted and off-centred configuration observed in the two-beam levitation experiments, for two different particle aspect ratios. (a) Top view of a high- k spheroid (left) and corresponding side view sketch (right). $k = 4.2$, $\epsilon = 0.17$, $P_{tot} = 20.5mW$, $\omega_0 \approx 1.7\mu\text{m}$. (b) Top view of a low- k spheroid (left) and corresponding side view sketch (right). $k = 3.3$, $\epsilon = 0.42$, $P_{tot} = 8.2mW$, $\omega_0 \approx 1.7\mu\text{m}$. The green arrows depict the up and down-beams.

Intuitively, one might suspect that such configurations would be the result of an inaccurate superposition of the beam axes. However, the beams were aligned very carefully, and these static states were reproducible, and robust, with or without slight changes in the relative positioning of the two beams. Moreover, the fact that the simulations (see Section A-4.2) clearly predict the existence of such static scenarios leaves few doubts that what is observed in the experiments indeed corresponds to the ideal case of perfectly coaxial beams.

A-3.3. Dynamic states of spheroids

A-3.3.1. Polar angle oscillations

Polar angle (PA) oscillations correspond to the sustained oscillations observed in [35, 36, 37] for particles with aspect ratios $k > 3$, or $k < 0.33$, in one-beam levitation experiments where $\omega_0 = 1.3\mu\text{m}$. The particles permanently tumble relative to the beam, performing a kind of “dance” consisting of back and forth translational and orientational motions (see Figure 20). The oscillation only involves the polar, or tilt angle, θ , which is measured with respect to the z -axis in a spherical coordinate system. These oscillations are general, meaning that they may occur when the particle is in bulk, or in contact to an interface, and can be both periodic and nonperiodic, depending on the shape parameters of the particle and its position along the beam axis [37]. They are direct evidence of the non-conservative nature of radiation pressure (RP) forces [55, 56]. When the motion is periodic, Mihiretie et al. showed that the frequency of oscillations, f , is proportional to the laser power, P_{tot} , and inversely proportional to the medium viscosity, η , forming the relation [37]:

$$f \sim \frac{P_{tot}}{\eta} \quad \text{A.16}$$

This behaviour is expected if the oscillation is driven by RP forces that are balanced by Stokes drag forces.

Our observations reveal that PA oscillations also exist in two-beam experiments; however, only within some very low power ratio ranges. Firstly, it should be noted that the beam waist radius in the present experiments, $\omega_0 \approx 1.7\mu\text{m}$, differs from that used in the one-beam geometry of Mihiretie et al., $\omega_0 = 1.3\mu\text{m}$ [35, 37]. The consequence of this change is that, for prolate spheroids, the critical aspect ratio, k_c , above which PA oscillations occur, is shifted to higher values. Whilst $k_c \approx 3$ when $\omega_0 = 1.3\mu\text{m}$, this changes to $k_c \approx 3.7$ for the beam waist $\omega_0 \approx 1.7\mu\text{m}$. This means that PA oscillations disappear when the ratio, $\frac{\omega_0}{a}$, becomes too large. This phenomenon was reproduced and explained with simple 2d RO simulations by Loudet et al. [39].

In a typical two-beam experiment, a high- k ellipsoid (with $k > k_c$) is first levitated by the up-beam all the way to the ceiling of the cuvette. As the particle oscillates, the second, down-

beam is switched on, whereby its power is progressively increased throughout the experiment. The outcome of this is a slowing down of the particle dynamics. Interestingly, if a high enough value of ε is reached, the particle will eventually become immobilized, and adopt one of the oblique configurations mentioned in Section A-3.2.2. Otherwise stated, the PA oscillations are “killed” above some power ratio threshold, ε_c , that depends on k (typically, $0.1 < \varepsilon_c < 0.5$). This is illustrated on the overview bifurcation diagram that we shall describe below (see Section A-3.4).

Although the above two-beam experiments were focused only on prolate spheroids, similar behaviour may be expected from their oblate counterparts ($k < 1$), which also exhibit PA oscillations during one-beam levitations [37]. Hence, the two-beam configuration permits the stoppage of PA oscillations for high ellipticity particles, be they prolate or oblate. Our observations confirm previous predictions based on RO calculations that will be presented in a later section.

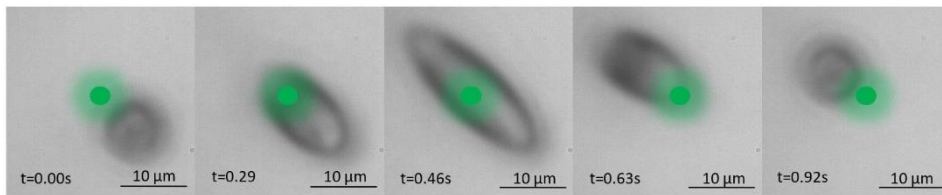


Figure 20: Polar angle oscillations of spheroid at the ceiling of the cuvette. This sequence is only half of the oscillation, as the other half is a mirror of the first. The particle passes through the single beam (the green spot) and repeats that motion back and forth until the power is changed. Experimental parameters: $k = 4.55$, $P_{tot} = P_{\uparrow} = 5.83mW$, $\omega_0 \approx 1.8$.

Off-centred PA oscillations (see Figure 21) are a distinct variant of the standard PA oscillations. This type of motion has not been observed prior to this work, as far as we know. The dynamics are still planar, except they only occur on one side of the beam axis. Much like the standard PA motions, the frequency of the oscillation is reduced as the power ratio, ε , is increased. However, contrary to standard PA oscillations, the time average configuration of the particle is not aligned with the beam axis, and as ε is increased, so does the amplitude of the movements, which instead remains constant in the standard PA case. It should also be noted that since these states always occur after an off-centred, tilted equilibrium state, they also adhere to the rule of having their top tip pointing away from the beam axis (on average), while their bottom tip points toward it (on average). This is the case, since so far, only particles below k_c have been observed to perform such dynamics.

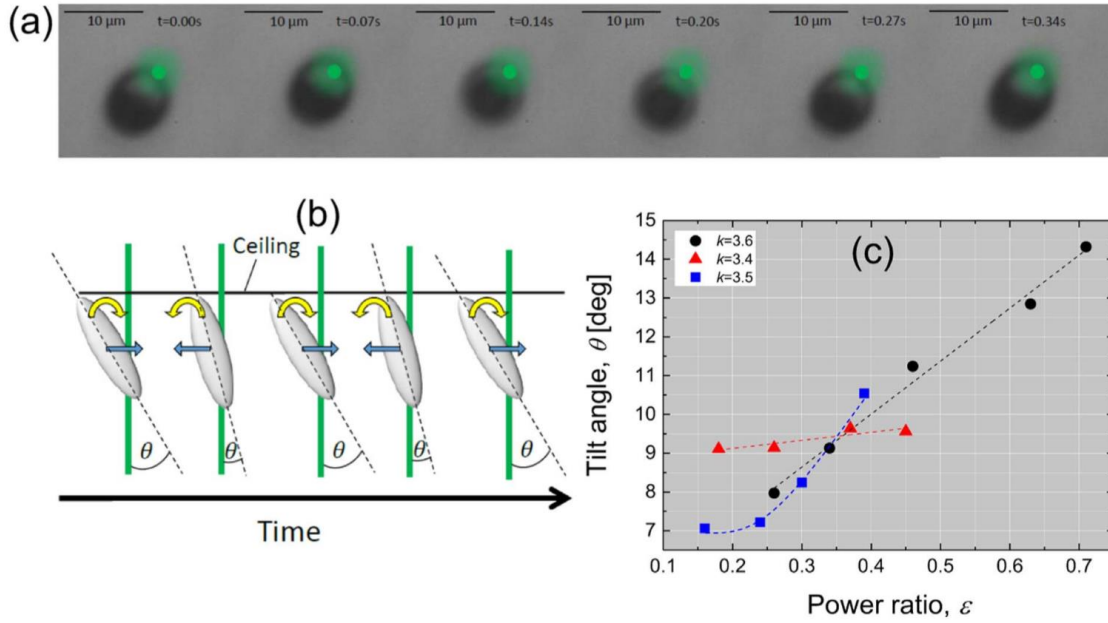


Figure 21: Sequence of off-centred PA oscillations observed in the two-beam geometry. The particle performs sustained oscillations within a plane, both in translation and rotation, but only on one side of the beam axis. (a) Time sequence of top-view optical images. Experimental parameters: $k = 3.6$, $\epsilon = 0.63$, $P_{tot} = 8.7\text{mW}$, $\omega_0 \approx 1.7\ \mu\text{m}$. (b) Schematic side-view illustration of the asymmetrical particle motion. (c) Evolution of the maximum tilt angle, θ_{max} , achieved by 3 different particles as a function of the power ratio. Dashed lines are simply guides for the eye.

A-3.3.2. Azimuthal angle oscillations

This type of motion constitutes a new kind of dynamical state, also not reported in previous works. Azimuthal angle (AA) oscillations only occur for particular two-beam configurations, and have been observed both at the cuvette top boundary, as well as in bulk (which requires a very delicate power balance to achieve). They consist of periodic oscillations of the azimuthal angle, ϕ , in reference to a 3d spherical coordinate system, where the particle follows a conical-type trajectory around a pivot point. The motion is shown using top view images in Figure 22. The ellipsoid is tilted with respect to, and oscillating around, the beam axis, while its top tip is in contact to the ceiling near the pivot point. The particle pivots in a periodic manner, with angular excursions in ϕ between 0 and 180° , depending on ϵ . As far as can be seen from the limited resolution of the video images, the pivot point hops to a slightly different position when the motion reverses, meaning that the particle does not follow exactly the same path when coming back to the initial azimuth angle. The qualitative trend observed so far is that, the higher the power ratio, ϵ , the greater the excursion in ϕ will be during the oscillation. The tilt angle, θ , remains the same throughout the rotation, and typically ranges from $\approx 5^\circ$ to $\approx 20^\circ$.

The bifurcation diagram in Figure 24 marks the domains of existence of AA oscillations (yellow circles) within the (k, ε) plane. They appear for $3 < k < 3.3$ and $4.2 < k < 4.5$ when $\varepsilon > 0.2$, both above and below the critical aspect ratio, $k_c \approx 3.7$. Much like the off-centred PA oscillations, AA oscillations occur directly after an off-centred and tilted equilibrium state. Hence, they exhibit the same kind of configurations for high aspect and low aspect particles in terms of their tip orientation. If the ellipsoid has a high k , its top tip will point toward the beam, and vice versa, if k is low, then the top tip of the particle will point away from the beam axis.

It is worthwhile to note that seemingly similar rotations, both at a boundary and in bulk, were reported by Neves et al. for optically trapped polymer nanofibers [11]. This study will be commented on in the discussion part.

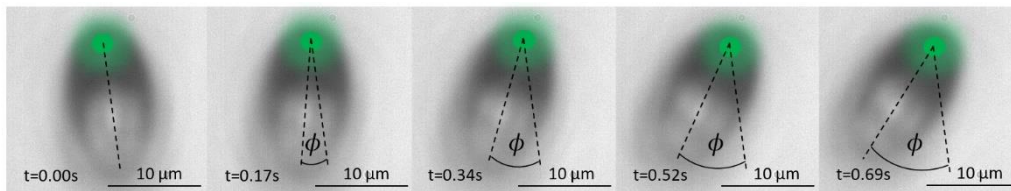


Figure 22: Sequence showing azimuthal angle (AA) oscillations. Again, this is just the first half of the oscillation, whereby the second half is a mirror of the first. The particle pivots around the beam axis of the two coaxial beams (the green spot), resulting in sustained oscillations of the azimuthal angle, ϕ . Experimental parameters: $k = 4.2$, $\varepsilon = 0.32$, $P_{tot} = 20.48\text{mW}$, $\omega_0 \approx 1.8\mu\text{m}$.

A-3.4. Bifurcation diagram

The different kinds of oscillations described in the previous sections can be represented as limit cycles inside the configuration space, which is three-dimensional (see Figure 23). The first dimension is the distance between the particle centre and the beam axis, Δr , the second is the tilt (or polar) angle, θ , and finally, the third is the azimuthal angle, ϕ . ϕ defines the position of the plane containing both the beam axis and the particle centre.

The blue cycle, corresponding to standard PA oscillations, is centred about the origin ($\Delta r = 0$, $\theta = 0$, $\phi = 0$) and occurs within the $\phi = 0$ plane. In reality, the plane of oscillation would gradually drift in azimuth in some of the experiments. As these drifts were slow on the scale of the oscillation period, they can be interpreted as the cycle slowly moving up and down, parallel to the ϕ axis.

The cycle with a dashed line in represents an off-centred PA oscillation. Graphically, it is similar to the standard PA cycle, except that it is centred on one side of the beam axis, which corresponds to a finite value of Δr .

AA oscillations are simply represented as a vertical brown line in Figure 23. This is due to the approximation that Δr and θ are about constant within a period of the motion. This representation is quite rough as a result of the poor resolution of the optical images. In fact, tiny changes in Δr and θ can be detected, but not measured with accuracy, meaning that the trajectory in the diagram is not quite a line, but a limit cycle spanning a small but finite area.

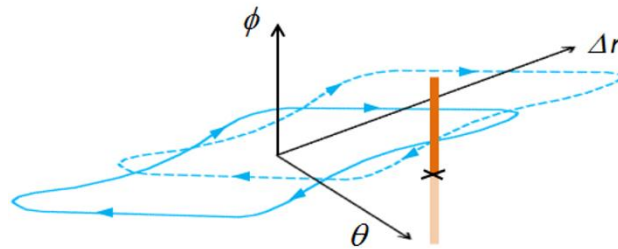


Figure 23: Limit cycles corresponding to the different types of particle oscillations that occur in two-beam experiments. Solid blue line: standard polar angle (PA) oscillation. The shape of the cycle is based on the former work by Mihiretie et al. [35, 36, 37]. Dashed blue line: off-centred PA oscillation. The brown line is a simplistic representation of the conical motion performed during azimuthal angle (AA) oscillations.

All types of static and dynamical regimes encountered in the two-beam levitation experiments have been gathered in a bifurcation diagram that has been plotted in the (k, ε) plane (see Figure 24). At this point, it is worth recalling that all the data points in the bifurcation diagram were obtained using prolate spheroids in the “contact” configuration (an example is shown in Figure 19), and with $\omega_0 \approx 1.7\mu\text{m}$.

The black crosses correspond to a stable static state at the origin ($x = y = z = 0, \theta = 0$). The ellipsoid stands vertically, centred on the beam axis, with its long axis parallel to that of the beam. This only occurs during one-beam experiments, when $\varepsilon = 0$, and the aspect ratio of the spheroids is below the critical threshold (in this case $k < k_c \approx 3.7$), as shown previously [35, 36, 37].

The solid black circles represent static, oblique configurations, where the particle is tilted and off-centred with respect to the beam axis. These states require the two-beam geometry and cover a large part of the diagram.

The standard PA and AA oscillations are marked by empty blue and yellow) circles, respectively. The former exist in both the one- and two-beam configuration, whereas the latter only occur for certain power ratios involving both beams.

The green squares symbolize the off-centred PA oscillations. Note that the particles which undergo such motions do not oscillate under one-beam exposure, and are below the critical aspect ratio for the beam waist $\omega_0 \approx 1.7\mu\text{m}$ ($k < 3.7$). As has already been explained, the particle performs sustained oscillations within a fixed plane, performing both translational and orientational motions. However, unlike standard PA oscillations, the particle remains only on one side of the beam axis, thereby creating an asymmetrical situation (see Figure 23). Preliminary measurements show that the tilt amplitude is an increasing function of ε (see Figure 21c)).

Finally, the orange squares correspond to irregular dynamical regimes, where the particle seemingly performs violent and unpredictable motions around the beam axis. They occur above a threshold power ratio. Similar irregular dynamics have already been pointed out in one-beam levitation experiments [37].

It should be noted that for each of the data series (vertical sequences of points – each corresponding to same particle with a given aspect ratio) plotted in Figure 24, the total power inside the sample was kept constant, and the difference in power was always maintained to be high enough so as to prevent the particle from falling. Additionally, no qualitative difference in dynamics was observed when using either a high, or a low total power – the power ratio is what determines the particle states. The only noticeable change was the frequency of the sustained oscillations, which is proportional to the total power [35, 36, 37].

Perhaps the most salient conclusion that may be drawn from Figure 24 is that the power ratio, ε , in addition to the aspect ratio, k , may serve as another bifurcation parameter between static and dynamical regimes. This is of direct practical interest, and it constitutes another important new feature obtained from the two-beam levitation experiments.

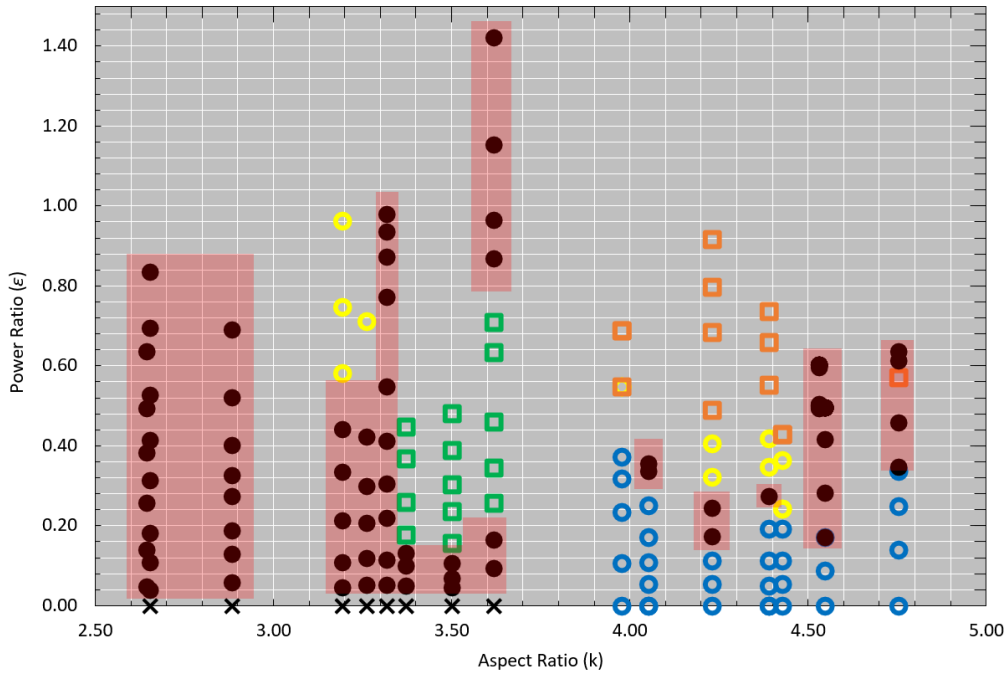


Figure 24: Experimental bifurcation diagram summarising all the static and dynamical regimes obtained in both one- and two-beam manipulations, as a function of the beam power ratio, ε , and the particle aspect ratio, k . The blue circles represent standard polar angle (PA) oscillations. The yellow circles show the azimuthal angle (AA) oscillations. The black crosses correspond to particles with a stable, fixed point at the origin, with their long axis parallel to the beam. The orange squares are ‘unstable’ scenarios, where the particle performs seemingly random and sporadic motions. The green squares locate the off-centered PA oscillations, and finally, the black spots represent the static, tilted and off-centered states. The red area highlights these static, oblique particle configurations on the diagram. The beam waist radius for all experiments shown here is $\omega_0 = 1.7\mu\text{m}$.

A-3.5. Single beam three-dimensional trapping

This section is dedicated to experiments carried out with the Elliot-Olympus IX73 optical tweezer setup (see Section A-2.3 for technical details). To recapitulate briefly, the setup uses a single laser beam, directed upwards through the microscope objective. This objective then has the two-fold function of focusing the laser, and building the image of the sample (see Figure 6).

The system was built to work as a 3D optical trap only when a very large numerical aperture (NA) objective is in place (in this case 100x, oil immersion, $NA = 1.30$). According to the Rayleigh criterion, the 100x objective provides “extreme focusing”, meaning that it can focus the laser beam down to a spot which is less than a wavelength in diameter (in this case $\lambda_0 = 1070\text{nm}$). Intermediate aperture objectives, such as 20x ($NA = 0.45$) and 40x ($NA = 0.60$) only

provide “intermediate focusing” (IF), with the beam waist diameter being slightly larger than the wavelength.

A-3.5.1. Comparison between the optical tweezers and the optical levitator

It is instructive to compare the beam characteristics corresponding to the different objectives used in the Elliot setup with those of the optical levitator (OL). Note that beam cross-section in the OL setup is not cut by any aperture, hence it remains close to Gaussian everywhere, including within the sample cell. The beam characteristics are the beam waist radius, ω_0 , the far field diffraction angle:

$$\theta_\infty = \frac{\lambda}{\pi\omega_0} \quad \text{A.17}$$

and the Rayleigh length (see Equation A.4), l , where:

$$\lambda = \frac{\lambda_0}{n} \quad \text{A.18}$$

with n as the refractive index of the medium through which the beam is propagating. In the case of the Elliot-Olympus setup, where the infrared beam is supposed to overfill the objective aperture diaphragm, the beam cross-section in the sample cell becomes close to an Airy spot, rather than being Gaussian. For the purpose of a rough comparison between the OT and OL beam parameters, we may take the beam aperture angle:

$$u = \sin^{-1}\left(\frac{NA}{n}\right) \quad \text{A.19}$$

to be the equivalent of θ_∞ for the OT beam. The beam waist radius is then deduced by using $u = \theta_\infty$ in a rearranged form of Equation A.17. For simplicity, the transition from oil to water is ignored, and it is supposed that $n = 1.50$, the refractive index of oil. Calculated values of the beam parameters are displayed in Table 2.

	ω_0 (μm)	θ_∞ (rad)	l (μm)
OL / 3.6 μm	3.6	0.034	105
OL / 1.6 μm	1.6	0.077	21
Elliot / 20x	0.76	0.30	2.54
Elliot / 40x	0.55	0.41	1.33
Elliot / 100x	0.22	1.05	0.21

Table 2: Shape parameters of the Gaussian beam in the case of the optical levitator (OL), as well as equivalent parameter values for the Elliot-Olympus IX73 setup.

Clearly, the optical levitator may be seen as very weakly focusing when compared to the optical tweezer configuration with the 100x objective. Note that the Rayleigh length varies from very large, down to very small on the scale of a typical spheroid length (respectively for the different particle sizes used in the OT and OL setups). In the conditions of the first row of the table, the particle essentially experiences a cylindrical laser beam. These circumstances mean that the optical forces do not vary by much when the particle moves up or down, parallel to the laser axis. Conversely, the 100x OT configuration generates a very strong axial gradient of intensity, which is required for 3D trapping. Optical forces are very sensitive to whether the particle centre is upstream or downstream of the beam focus.

A-3.5.2. 3D Trapping of polystyrene spheres and spheroids

3D optical trapping with the OT/100X setup was first attempted with spherical PS particles with diameters between 1 μm and 10 μm . Trapping in bulk water was verified using the whole range of particle sizes (1 μm to 10 μm). Horizontal (x , y) trapping locked the particle onto the laser axis very strongly, with the presence of small Brownian excursions (see Figure 25). Axial trapping, however, was delicate, especially with medium sized (2 μm to 4 μm) particles. It was found to be necessary to first bring the laser focus above the particle, meaning that the scattering and gradient forces would act in the same direction in order to achieve trapping. The particle would then be raised to the beam waist and come into focus on the video images. This would result in the particle finally being trapped in the z direction, to complete the three-dimensional trap. However, it was observed that axial trapping was weak in general, even when the laser was at high power ($> 1\text{W}$). It was not a rare occurrence for the procedure to fail, or for the particle to escape the observation plane after a few seconds. Some quantitative information about the trapping stiffness could be obtained using the Elliott tracking software, although the tracking is limited to excursions in the (x , y) plane, from which only the horizontal

trap stiffness constants, κ_x and κ_y , can be calculated (see Figure 25). Even though no quantitative information about the z -direction is available through the software, in general, the practical conclusion is that $\kappa_z \ll \kappa_x \sim \kappa_y$ for the tested PS particles.

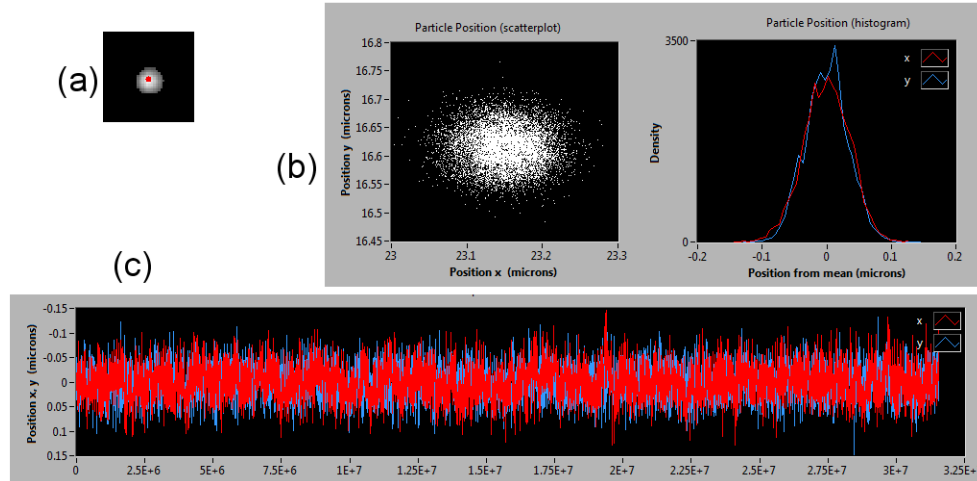


Figure 25: 3D trapping of a spherical PS particle. Experimental parameters: $R_0 = 1\mu\text{m}$, $P = 2.3\text{W}$, 100x objective. (a) Snapshot of the trapped particle (frame rate 50 fps) in bulk water. The red spot indicates the (x, y) position of the particle as determined by Elliot's tracking software. (b) Cloud of (x, y) particle positions (10^5 points) and the corresponding histograms. Standard deviation $\approx 35\text{nm}$. Note that the cloud is anisotropic, as might be expected due to the laser polarisation [57]. The corresponding trap stiffness constants are $\kappa_x \approx 3.2\mu\text{Nm}^{-1}$ and $\kappa_y \approx 3.8\mu\text{Nm}^{-1}$. (c) Time fluctuations of the position – evidence of the Brownian motion of the particle (time unit: $1\mu\text{s}$).

For the optical trapping of spheroidal particles, the typical particle diameter of the mother spheres was between $3\mu\text{m}$ and $4.5\mu\text{m}$, although some experiments were performed with larger sizes.

Surprisingly, the 3D trapping of high- k particles was easier to accomplish and more robust than that of spheres. The procedure is the same as the one described above, meaning that it starts by bringing the laser focus above the particle, which is then followed by the trapping. Once exposed to the laser, the spheroid lines up its long axis with the axis of the beam and lifts up to an equilibrium position, where it is locked in place. An example of this is shown in Figure 26. 3D trapping was successful with particles ranging from large ($2c \sim 25\mu\text{m}$) to small ($2c \sim 4\mu\text{m}$). Generally, the particle self-equilibrated with its centre below the laser focus. This conclusion is based on simple experiments such as that shown in Figure 26. Figure 26 b) shows the image of a trapped ellipsoid in bulk water, which is located on the border of the focal plane of the objective, as seen by the camera, CAM2 (when $\delta_{z,CAM2} = 0\mu\text{m}$). The particle is clearly out of focus, as signified by the characteristic rings in the image. In Figure 26 c), the

observation plane has been moved $\approx 2\mu\text{m}$ below the focal plane ($\delta_{z,CAM2} = -2\mu\text{m}$), hence the enhanced focusing of the particle in the image.

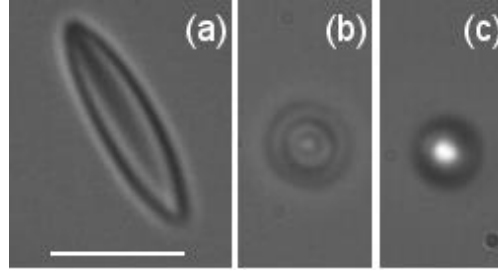


Figure 26: Example of the 3D trapping of an ellipsoid. (a) Image of the particle floating horizontally above the quartz-water (QW) interface. The scale bar is $5\mu\text{m}$ in length. The particle parameters are: $c = 4.15\mu\text{m}$, $a \sim 1\mu\text{m}$, with $k \approx 4.2$. (b) Photo of the optically trapped particle in bulk water (image from camera CAM2, with $\delta_{z,CAM2} = 0\mu\text{m}$). (c) Image of the particle in better focus, obtained with the $\delta_{z,CAM2} \approx -2\mu\text{m}$ configuration.

An alternative way to show that the centre of the trapped particle is below the laser focus is shown in Figure 27. Here, CAM1 is used, since it only yields images from the objective focal plane. Due to the hydrodynamic drag, when the microscope focus (and hence the laser focus) is adjusted suddenly by $\approx -5\mu\text{m}$, the particle cannot immediately accompany the laser focus shift to reach its equilibrium configuration. Consequently, the observation plane temporarily moves down, along the particle body. A much sharper image of the particle is then obtained, as shown in Figure 27.

A third procedure consists of (slowly) moving down the objective until the particle touches the bottom boundary of the sample cell (the QW interface), as depicted in Figure 28. In this case, the microscope is brought down at a rate of $< 1\mu\text{ms}^{-1}$, so that the particle can follow the motion of the laser focus inside the water medium.

The altitude of the laser focus, $z_{laser\ focus}$, can be read continuously throughout the recorded video sequence. Note that the reading, z_{read} , must be referred to with respect to an origin, which is taken as the altitude, z_{QW} , where a well-defined Airy spot from the laser is visible on the QW interface (see Figure 80 in the Appendix). Moreover, the difference, $z_{touch} - z_{QW}$, must be corrected due to the refraction through oil and water. The value, $z_{laser\ focus}$, is then given by:

$$z_{laser\ focus} = \frac{n_w}{n_{oil}} (z_{read} - z_{QW}) \quad \text{A.20}$$

with the refractive index of water being taken as, $n_w = 1.33$. In the above formula, it is supposed that the index-matching between oil and quartz is perfect. Since the oil is made to have the same refractive index as glass ($n_{oil} \cong n_{glass} \cong 1.50$), it does not have exactly the same refractive index as the quartz coverslip. However, since the difference is not so large, the assumption is maintained, since it provides much in terms of simplicity.

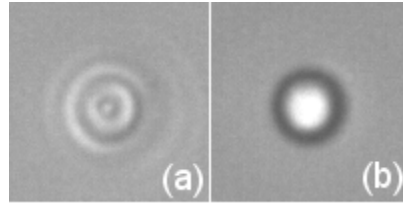


Figure 27: (a) Standard image of the trapped particle. (b) The altitude of the objective has been suddenly decreased by $\delta_z \sim -5\mu\text{m}$. A transient, well focused image of the particle is captured by the camera, CAM1, before the particle has a chance to react to the shift. The particle parameters are: $c = 4.1\mu\text{m}$, $a \sim 1.1\mu\text{m}$ and $k \approx 3.8$.

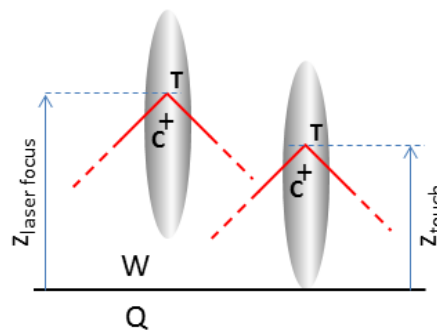


Figure 28: Driving the particle down until contact with the cell bottom boundary (QW) is made. The red lines represent the focused laser beam.

The image of the particle does not change so long as the bottom tip is in bulk water. A discontinuity in the sequence of images can be detected when the particle touches the interface, at $z_{laser\ focus} = z_{touch}$. The effect is shown in Figure 29. Figure 29 a) is a standard image of the trapped particle in bulk water, as observed by CAM2. To improve the detection of the particle collision with QW, the camera is shifted by $\delta_{z,CAM2} \approx +2\mu\text{m}$, which gives a strongly defocused image, as shown in Figure 29 b). The advantage of defocusing the image resides in the easily visible large ring that can be seen in Figure 29 b) c) and d). The diameter of this ring is approximately constant when the particle is in bulk water, but suddenly decreases once $z_{laser\ focus} = z_{touch}$. The evolution of the ring diameter is shown in Figure 30.

Experimental results

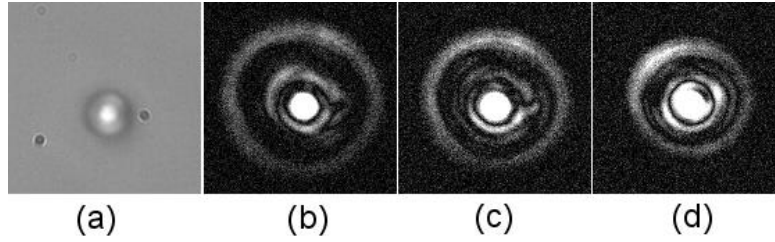


Figure 29: Sequence showing the particle being trapped in bulk water, then taken down to the QW boundary. (a) Shows an image of the particle in bulk water. (b, c, d) Correspond to $z_{laser\ focus} = 14.2\mu\text{m}$, $6.24\mu\text{m}$ and $5.0\mu\text{m}$, respectively. The contrast of the rings has been increased by image subtraction in order to aid the reader. The particle parameters are: $c = 5.25\mu\text{m}$, $a \approx 1\mu\text{m}$ and $k \approx 5.3$.

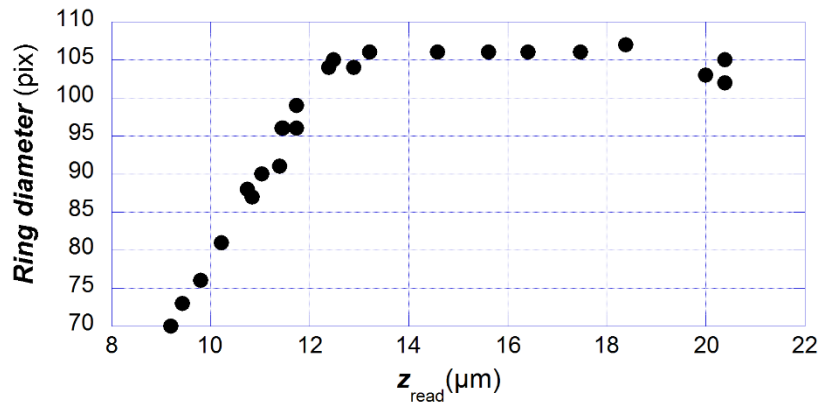


Figure 30: The evolution of the diameter of the outermost ring (see Figure 29 b) c) and d)) as a function of the objective altitude, z_{read} . Contact with QW is made at $z_{read} = 12.8\mu\text{m}$. The particle is the same as that in Figure 29.

The point at which the particle makes contact with the QW interface is easily identified as the kink in the graph, from which it can be deduced that $z_{touch} = 7.47\mu\text{m}$, with a $(+0.7\mu\text{m}, -0.6\mu\text{m})$ uncertainty. In this case, the value, z_{touch} , indicates the position of the laser focus within the 3D-trap configuration (see T in Figure 28). Since $c = 5.25\mu\text{m}$ in this case, it can be concluded that the laser focus is located between the particle centre, C, and its top tip. This procedure was repeated with many particles of different sizes, resulting in the same outcome every time. To illustrate this point, a few of the results have been gathered in Table 3.

$c (\mu\text{m})$	2.6	5.2	4.4	4.1	5.3	10.4	11.8
k	2.0	6.4	4.9	3.8	5.3	3.3	3.4
$z_{touch} (\mu\text{m})$	4.0	5.7	5.6	5.1	7.5	13.2	12.5

Table 3: Results of QW contact experiments with particles of different sizes and aspect ratios. The 100x objective is used at $NA = 1.30$, which is the maximum.

The uncertainties on z_{touch} are approximately $\pm 1\mu\text{m}$. Consequently, it is not possible to accurately locate the position of the laser focus on the scale of the particle semi-axes; however, the conclusion that T is above C, as indicated in Figure 28, is both solid and general.

A-3.5.3. Influence of the objective aperture

The results from the previous Section, A-3.5.2, have been obtained with the 100x objective being operated at maximum aperture, $NA_{max} = 1.30$. Optical trapping is very stable in such conditions, as has been discussed. However, it is expected that if the aperture is diminished beyond some critical value, NA_{crit} , the trap stability would decrease and the particle would escape the trap. The general observation that was made by progressively closing the objective iris diaphragm is that it has the effect of slightly moving the trapped particle up. This is illustrated by the photos shown in Figure 31. Figure 31 a) shows a standard image of the trapped particle when $NA = NA_{max} = 1.30$. In Figure 31 b), the aperture has been reduced to $NA \approx 1.1$ (this value was determined using the method described in the Appendix - Numerical aperture calibration). Clearly, when $NA \approx 1.1$, the image is more focused, which means that the particle centre has moved up, close to the altitude of optimal focus.

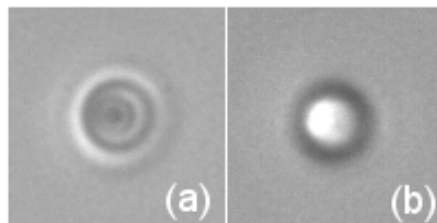


Figure 31: Showing the effect of partially closing the aperture diaphragm during the trapping of a particle in equilibrium. (a) Image of the particle slightly out of focus when trapped in equilibrium with the objective at maximum numerical aperture, $NA = NA_{max} = 1.30$. (b) Sharper image of the particle with a reduced numerical aperture, $NA \approx 1.1$, whilst still trapped and in equilibrium, signifying a shift in altitude relative to the beam focus. The particle is the same as that in Figure 29 and Figure 30.

Figure 32 shows the results of a quantitative study concerning the particle shift in altitude with respect to variations in the numerical aperture. The manipulated particle was the same as that in Figure 29, Figure 30 and Figure 31 and was observed with the camera, CAM2, as the 100x iris diaphragm was progressively closed. For each discrete size of the diaphragm, the position of the camera was adjusted to achieve the best particle image focusing, with the corresponding difference in altitude between this image and the beam focus being recorded as, $\delta_{z,CAM2}$. 3D trapping could be maintained down to approximately $NA \approx 0.85$, which may be taken as the value, NA_{crit} , for this particle. As can be seen in Figure 32 a), the value of $\delta_{z,CAM2}$

Experimental results

increases from $\sim -2.2\mu\text{m}$ to $\sim -0.5\mu\text{m}$, meaning that the particle was shifted up by $\sim 1.7\mu\text{m}$ between NA_{max} and NA_{crit} . Thus, reducing the aperture has the effect of shifting the particle centre up to a position closer to the laser focus, as has been illustrated in Figure 32 b). It was also observed that the Brownian fluctuations of the particle became very large when approaching NA_{crit} . These large fluctuations signal that the particle is close to escaping from the optical trap. Conversely, when the trap is operated at NA_{max} , the Brownian fluctuations are almost imperceptible, indicating that the trap has a very high stiffness.

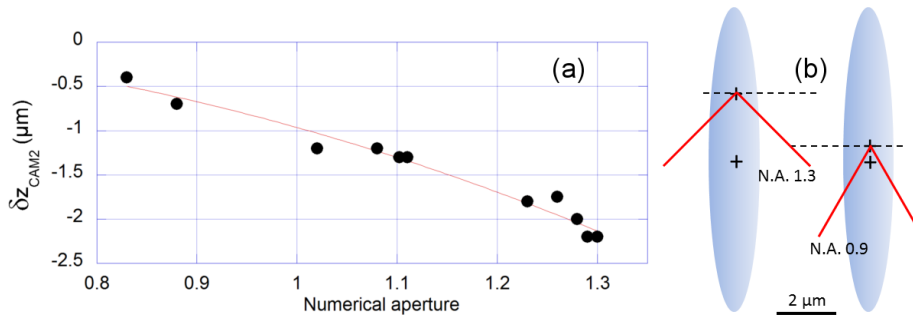


Figure 32: (a) Focus correction of the CAM2 image of the trapped particle, against the 100x objective numerical aperture. The red line is simply there to help with visualisation. (b) Sketch of the trapped spheroid, at NA_{max} (left) and reduced NA (right). The laser beam is represented by the red lines. Angles are not to scale, for clarity. The particle is the same as that in Figure 29, Figure 30 and Figure 31.

A-3.5.4. The dependence of trap equilibrium on laser power

When the setup is in the configuration, AOff-NGin, as is the case in most of our experiments, the optical forces that can be exerted on the polystyrene particles are on the scale of piconewtons. A particle such as the one used in Section A-3.5.3, has a buoyancy corrected weight of $\sim 0.01\text{pN}$. In view of the very small Brownian fluctuations exhibited by trapped particles at NA_{max} , it is presumed that forces resulting from the thermal agitation of water molecules do not significantly influence the particle equilibrium. Therefore, it can be considered that only the optical forces are involved when the particle is trapped. If nothing in the system absorbs light with the wavelength of the laser ($\lambda_0 = 1070\text{nm}$), it is expected that the optical forces will simply be proportional to the laser power (P). Consequently, the trapping configuration should not depend on P . Note that “nothing” means that neither the particle, or the surrounding water and cell walls, are absorptive. Otherwise stated, the assumption being made is that the temperature of the system remains constant, and equal to room temperature, regardless of how high, or low, the laser power may be.

Figure 33 shows the results of an experiment carried out with the same particle as that in Section A-3.5.3; however, instead of changing the objective aperture, which is now constantly NA_{max} , the laser power is varied, with the particle still being observed by CAM2. The shift in CAM2, δz_{CAM2} , is once again utilised in order to determine the particle altitude. This experiment clearly indicates that increasing P shifts the particle to a lower altitude, meaning that the laser focus moves closer to the top tip of the particle, as illustrated in Figure 33 b). The amplitude of this shift is $\approx 1.3\mu\text{m}$, and is far from negligible on the scale of the particle.

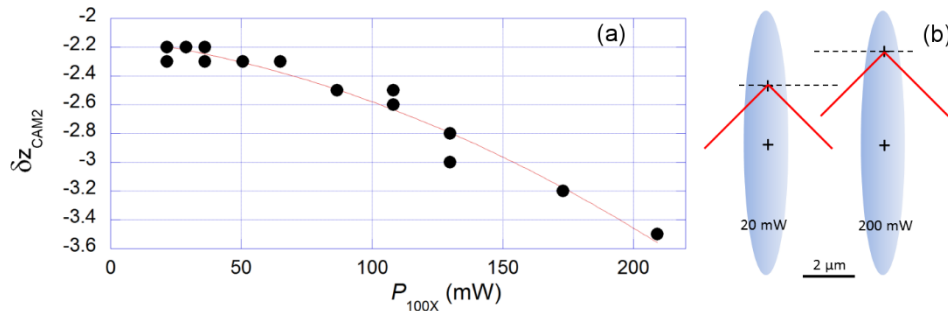


Figure 33: (a) The dependence of the trapping configuration on the laser power. The red line is simply there as a guide. P_{100x} is the power of the laser beam in the plane of the objective pupil. (b) A sketch of the trapped ellipsoid at low (left) and high power (right). The laser beam is depicted by the red lines. The particle that is used is the same as that in A-3.5.3, with the numerical aperture as $NA = NA_{max} = 1.30$.

The conclusion to be drawn from these results is that there is a source of nonlinearity in the system, the effect of which becomes visible at high powers. It is not clear whether the sensitivity of the equilibrium to P is due to some absorption by at least one of the constitutive elements of the system, or due to a change of the polystyrene refractive index because of the very intense light in the focal zone. It should be noted that this effect is only evident for $P_{100x} \geq 50\text{mW}$, with most of the experiments having been carried out at a lower power, well within the range where the linear relationship between the optical forces and P can be assumed safely.

A-3.5.5. The stability of spheroid trapping in 3D

The stability of the optical trap can be tested by moving the sample cell around the particle, or equivalently, moving the particle inside the water medium of the sample cell. In both cases, the hydrodynamic force and torque due to the motion of the particle relative to the fluid, perturb its efforts to attain equilibrium in the laser beam. To test the lateral stability of the trap, the cell was moved horizontally (in the x, y plane) using the motorised microscope platform. The velocity of the platform was progressively increased up to the point where the particle escapes the trap. A similar test could be performed using the 100x objective, whilst altering the altitude

at various velocities to create a vertical flow, in order to determine the stability along the z -axis. However, the latter option is not practical because of the very short working distance of the objective, which does not allow enough time to reach a constant state. Therefore, an alternative method was used, which consisted of keeping the particle against the bottom boundary (QW), whilst lowering the laser focus, so that the upward force from the interface pushes the particle above the natural equilibrium point of the 3D-trapping, and the behaviour of the particle can be explored with the laser focus below z_{touch} (see Figure 28). This will be referred to as the “ Δz_+ stability test”.

Firstly, the response of the particle to horizontal flow will be dealt with, after which, the Δz_+ stability test will be addressed.

A-3.5.6. The response of a trapped particle to Stokes flow

Moving the cell horizontally (in the x or y directions), whilst observing the behaviour of a trapped particle, is a typical way to find the lateral stiffness of an optical trap, and has been used by many authors with spheres [58]. In the reference frame of the particle, the lateral motion is the same as having a uniform Stokes flow coming from that direction. The procedure progressively increases the velocity of the motion until the sphere escapes the trap laterally. Then, combining the knowledge of the flow velocity with the Stokes formula for hydrodynamic drag on a sphere gives an estimate of the maximum lateral force exerted by the laser beam on the particle. This experiment was also carried out with some ellipsoids, to learn something about how that kind of particle would behave under such circumstances. As will be seen, the response of the elongated particles is much more complex than that of spheres, as a result of the coupling of translation and rotation.

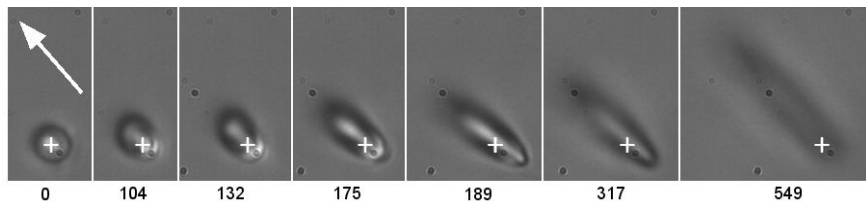


Figure 34: The escape of an ellipsoid from a 3D optical trap using a Stokes flow. The direction of flow is indicated by the white arrow. The time is indicated below each image, in milliseconds. Experimental parameters: $c = 6.4\mu\text{m}$, $a \approx 1.1\mu\text{m}$, $k \approx 5.8$, $P_{100x} = 22\text{mW}$, with the velocity of the motion (or flow) as $v_{flow} = 40\mu\text{ms}^{-1}$ and a video frame rate of 211fps.

Figure 34 shows a sequence of images taken from a video that captured a case of flow-induced particle trap escape. The experimental parameters are listed in the figure caption.

The flow velocity, $v_{flow} = 40\mu\text{ms}^{-1}$, is very close to the threshold value, v_{esc} , beyond which the particle escapes the trap. When $v_{flow} < v_{esc}$, the ellipsoid is simply pushed towards the direction of the flow, and is slightly tilted, as shown in the first two images of the Figure 34 sequence. The particle then remains in this asymmetrical configuration for as long as v_{flow} is constant.

This configuration, however, becomes destabilised when $v_{flow} \geq v_{esc}$. In order to interpret the images in Figure 34, the particle altitude must be ascertained. This was done by taking advantage of the blurred contours that exist in the images at different altitudes. The sequence shown in Figure 35 can be used as a guide to approximate what parts of the ellipsoid in Figure 34 are above the laser focus in each image. Figure 35 was made simply by bringing the particle in contact to the top boundary of the sample cell, against the glass cover slip, where it was stuck in place, and completely flat along the surface. This was possible because unlike with quartz, which comprises the cell bottom, polystyrene particles usually stick on a glass interface about a minute after contact has been made. The images in Figure 35 were captured with CAM2, whereby the leftmost frame has the optimal focusing, and is taken as the reference altitude of $0\mu\text{m}$. The other frames show the observation plane some micrometres below the particle, meaning that $\delta_{z,CAM2} < 0$. Thusly, a series of blurred contours corresponding to a specific altitude are generated, which enables a tentatively altitude measurement to be performed with different parts of the images in Figure 34.

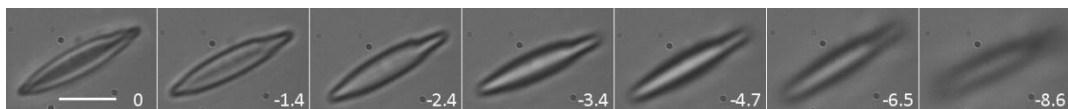


Figure 35: A series of video images showing the same ellipsoid as that in Figure 34 stuck to the water-glass interface (top boundary) of the sample cell. The numbers indicate the position of the observation plane below the particle in micrometres, and scale bar shown in the first frame spans $5\mu\text{m}$.

The conclusion of this analysis is shown in Figure 36. The ellipsoid is initially vertical (Figure 36 a)), with the focus of the laser located between its centre and upper tip, as was shown before. Firstly, the flow pushes the particle laterally (Figure 36 b)), much in the same way as it would a sphere. The off-centring of the particle then creates a torque, which makes the particle rotate (Figure 36 c)). In Figure 36 d) and e), the tilted particle advances upward, before finally being expelled above the laser focus (Figure 36 f)). Even though this is only a qualitative scenario, it is still valuable as a guide for simulations. In principle, it should be possible to reproduce this effect based on adequate approximations for the calculation of optical and hydrodynamic forces and torques. It is possible to compare this sequence with a simulation

that takes into consideration the particle off-centring, r , and its tilt, θ , which, if matching the experimental results, should form a curved trajectory when plotted on a graph. Reproducing this, however, even just qualitatively, would be a great testament to the accuracy of the simulation.

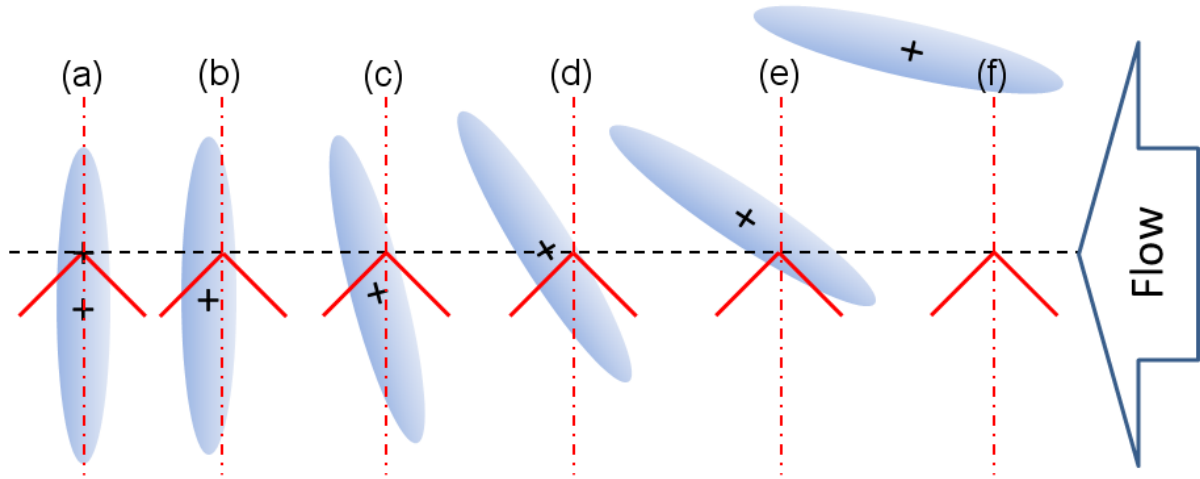


Figure 36: The proposed scenario for the response of the ellipsoid to a Stokes flow, finishing with the expulsion of the particle from the trap. The rightmost arrow indicates the direction of the flow. The red dashed and dotted lines mark the position of the laser beam axis in each frame, with the solid lines marking the laser focus. See text for comments.

A-3.5.7. The vertical stability of the 3D trap

The Δz_+ stability test starts with the particle in the same position as that sketched in Figure 28, with the laser focus initially located at point T. The focus is then slowly moved down so that the particle makes contact with the cell bottom (QW interface). Once contact is made ($z_{laser\ focus} = z_{touch}$), the focus continues to be moved down. This makes it possible to use the reaction force of the interface in order to move the focus vertically down, towards the bottom tip of the particle. In all cases it was observed that the ellipsoid would stay trapped along the beam axis over a large range in the z direction, down to a position with the laser focus below the particle centre. This altitude will be denoted as z_A from now on, and is represented pictorially as A in Figure 37. If the laser focus is brought below z_A , the configuration fluctuates, with the particle alternating between a vertical and a tilted position with respect to the beam axis. This phenomenon ceases to exist once the laser focus is taken beyond point B in Figure 37, which is marked as the altitude z_B , and is located below z_A . It is only in the altitude range $z_B < z_{laser\ focus} < z_A$ that the aforementioned fluctuations exist. Once the beam focus is below z_B , the particle is ejected laterally from the laser beam, which is shown in Figure 38, along with the relevant parameters of the experiment.

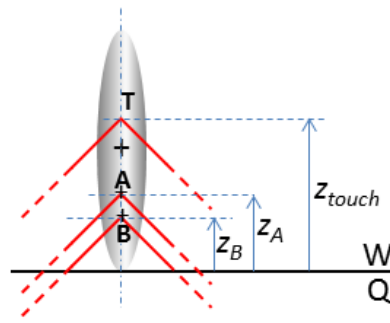


Figure 37: The Δz_+ stability test. The ellipsoid remains trapped along the laser axis when the laser focus is located between points T and A. The interval between points A and B is the domain where fluctuations in the tilt and position of the particle exist. Point B is the lower limit of 3D optical trapping. The distance between A and B has been exaggerated in favour of clarity.

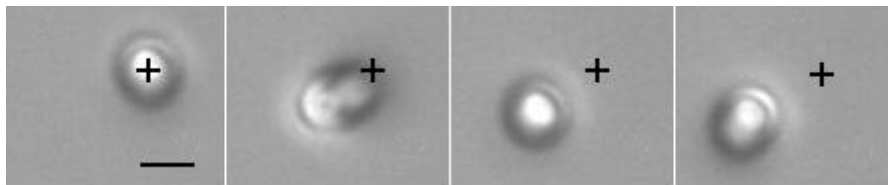


Figure 38: Ejection of the particle from the optical trap one the laser focus reaches point B (see Figure 37). Experimental parameters: $c = 5.25\mu\text{m}$, $a \approx 1\mu\text{m}$, $k \approx 5.3$, $z_{touch} = 7.5\mu\text{m}$, $z_A = 2.45\mu\text{m}$ and $z_B = 2.25\mu\text{m}$, with the scale bar in the first (leftmost) frame representing $2\mu\text{m}$.

A-3.5.8. Fluctuations near the bottom boundary

Here, the fluctuations of the ellipsoidal particles are addressed. During experiments around the bottom boundary, it was observed that when the laser focus was moved below point A (see Figure 37), the particle, rather strikingly, switches between two positions, one being along the beam axis, and the other with the particle tilted with respect to that axis. The typical tilt angles are significant enough to be noticed clearly, usually within the range of $\sim 20^\circ$ to $\sim 30^\circ$ (see Figure 39).

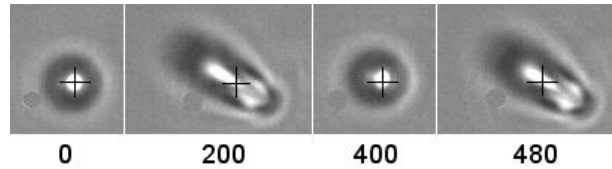


Figure 39: The oscillations of an ellipsoid in contact to the cell floor. The laser beam is elliptically polarized, with the setup being in the AOin-NGoff configuration. The position of the laser axis is marked by the black cross, and the number below each photo indicates the time in milliseconds. The sequence shows that the tilt does not change in sign, meaning that the ellipsoid always favours one side of the laser axis. Experimental parameters: $P_{100x} = 5\text{mW}$, $c = 5.15\mu\text{m}$, $k \approx 6.4$.

A spectral analysis of the videos that recorded this behaviour showed that the particle oscillates with a characteristic frequency f_{osc} , and that this frequency increases with the laser power in an approximately linear fashion. During these experiments, it was observed that the particles would always tilt in the same direction (and hence have the same plane of oscillation) regardless of the beam polarisation and power, or the location of the particle on the QW interface. It was soon concluded that the source of this asymmetry had to lie in the intensity distribution of the beam cross-section. This was as a result of a small misalignment of the beam axis relative to that of the objective. Large errors in alignment are easily detected by looking at the Airy spot on the QW or WG interfaces; however, very small errors are not so easy to spot. In the case of the observed fluctuations, the particle acts as a very sensitive detector of the beam cross-section symmetry, and may be used to refine the centring of the beam on the objective pupil quite accurately. Hence, the large amplitude particle oscillations and the related cross-sectional anisotropy are able to be suppressed through small adjustments in the M3 mirror (see Figure 7), as the laser axis aligns itself with that of the objective. Figure 40 a) shows the particle lying along the beam axis after corrections have been made, whereas Figure 40 b) to e) displays the consequences that small misalignments in different directions can have on the particle.

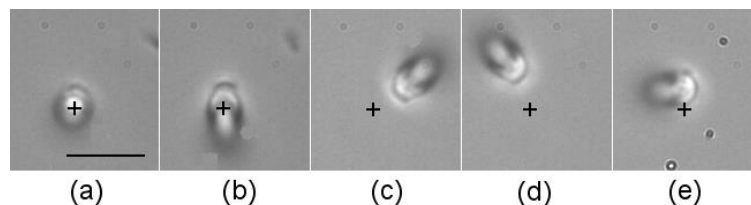


Figure 40: The effect of beam misalignment on particle oscillations. (a) Optimizing the alignment results in the particle being, on average, aligned and centred with respect to the beam axis. (b, c, d, e) The beam has been intentionally misaligned, resulting in the particle undergoing large amplitude oscillations in a direction which can be chosen by adjusting the sign and amplitude of the applied correction accordingly. Only images of high tilt are shown for the misaligned configurations. Experimental parameters: $c = 5.25\mu\text{m}$, $a \approx 1\mu\text{m}$, $k \approx 5.3$ and $P_{100x} = 35\text{mW}$.

Once the appropriate correction has been made, the particle is approximately centred on, and aligned with, the beam axis, yet still exhibits fluctuations. These fluctuations, which are of the order of $0.5\mu\text{m}$, are still large enough to be easily visible, and for the concept of their domain of existence to be between points A and B in Figure 37 to hold. In the region between points T and A, the particle remains firmly locked on to the beam axis, with no fluctuations, other than small Brownian motions.

Figure 41 to Figure 44 show preliminary results of a quantitative analysis of the fluctuations. The goal was to gather enough information to compare these fluctuations with the polar angle oscillations seen in optical levitation experiments, and check whether they are of the same nature. In principle, the corrections made to the alignment have left only the beam polarisation as a possible cause of anisotropy, and hence fluctuations. Therefore, the next course of action was to see whether the fluctuations were sensitive to the polarisation of the beam, and to find out if they were essentially random excursions, or real oscillations. As will be shown, the analysis indicated that the particle does in fact “oscillate” with a finite frequency, in spite of strong noise.

The video analysis of the oscillations was performed by in-house software developed by P. Merzeau (see Appendix - Spheroid tilt-tracking software). In short, the program sorts pixels of every image in binary form as either bright or dark, with the distinction between the two being set either by the user, or automatically using a well-marked two-mode histogram of grey levels. The program then determines the centre of each family of pixels, and each image yields two points, namely + and –, which look like a dipole superposed onto the particle. The separation between these two points is null when the particle stands vertically, and its image is round; however, this changes once the particle is tilted. This distance, d_{\pm} , is an increasing function of the particle tilt angle, θ . It is not necessary to know the shape of this function precisely, since it depends on the particle characteristics, illumination conditions, and camera parameters in a manner that is very complex. It is assumed that d_{\pm} , which will be referred to as the “tilt signal” hereafter, is proportional to the angle in the limit, $\theta \rightarrow 0$, which is sufficient to make quantitative comparisons between different videos of the same particle. An example of a tilt signal as a function of time is shown in Figure 41.

Experimental results

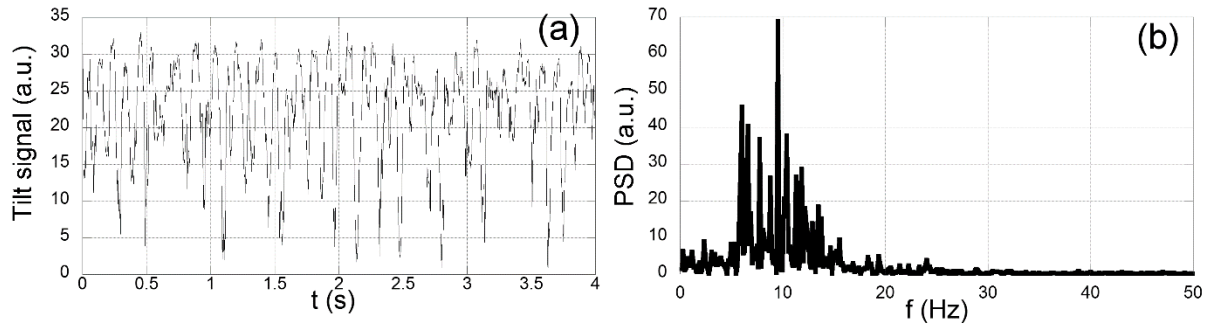


Figure 41: The polar angle fluctuations of a particle at the QW bottom boundary, with the laser focus in the domain between points A and B (see Figure 37). (a) The tilt signal against time. (b) The corresponding power spectral density. Experimental parameters: $c = 5.25\mu\text{m}$, $a \approx 1\mu\text{m}$, $k \approx 5.3$ and $P_{100x} = 50\text{mW}$, with a video frame rate of 211fps.

The spectral analysis reveals a distinct maximum in the Fourier spectrum at $f_{osc} \approx 9.5\text{Hz}$, which can be seen in Figure 41 b), in spite of the rather chaotic aspect of the tilt signal. The analysis indicated that the frequency varies in an approximately linear fashion with respect to the laser power, as is shown by the graph in Figure 42. However, it is not a simple proportionality, as is evident by the linear fit of the experimental points. The extrapolation of the graph to the frequency of zero indicates that the oscillatory character of the fluctuations only exists if the power is larger than the threshold value of about 12mW.

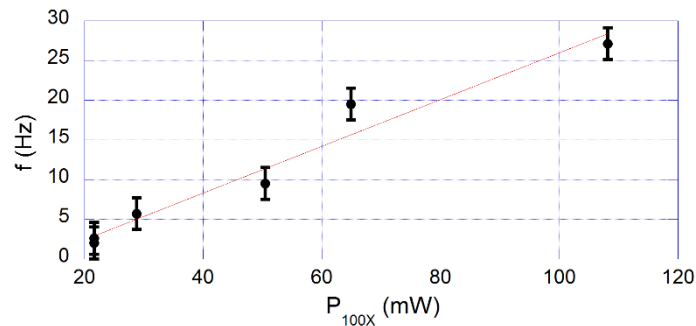


Figure 42: The characteristic frequency of the polar angle oscillations against laser power. The particle is the same as that in Figure 41.

The sensitivity of the oscillations to the polarisation of the laser is demonstrated in Figure 43. The graphs show the points best representing the mean (x, y) coordinates of the particle during fluctuations, which are defined as the barycentre of the dark pixels from the aforementioned binary pixel separation. This choice was deemed to be satisfactory, as far as could be discerned by the human eye (see Appendix - Spheroid tilt-tracking software). As can be seen in Figure 43, the clouds of points have a characteristic two-lobe structure. The graph indicates that the ellipsoid indeed switches between two configurations, which differ by a small shift, usually less than $1\mu\text{m}$, in the position of the particle. When the direction of the linear

polarisation is turned by 90°, the cloud structure definitely changes, proving that the oscillations are directly influenced by the state of polarisation of the light.

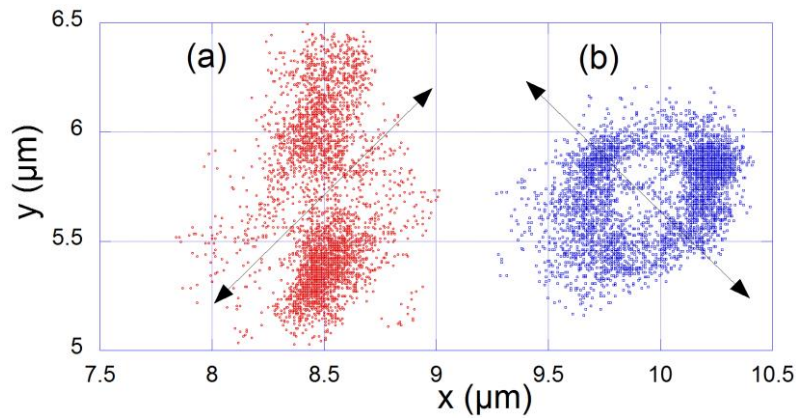


Figure 43: Analysing the sensitivity of the particle fluctuations to the polarisation of the laser beam. The setup was operated in the AOoff-NGin configuration. x and y represent the positions of the particle cross-section, with the two cases, a) and b), having been separated along the x -axis for clarity. The direction of the linear polarisation is indicated by the black arrow (parallel and perpendicular to the microscope symmetry plane in a) and b), respectively). Experimental parameters: the particle is the same as that in Figure 41 and Figure 42, with $P_{100x} = 22\text{mW}$.

The same method of positional analysis was used to study how the amplitude of the oscillations varies as a function of the laser power. The results are displayed in Figure 44. Despite the large scattering of the data points, it is possible to see that increasing the power has the effect of diminishing the amplitude of the oscillations.

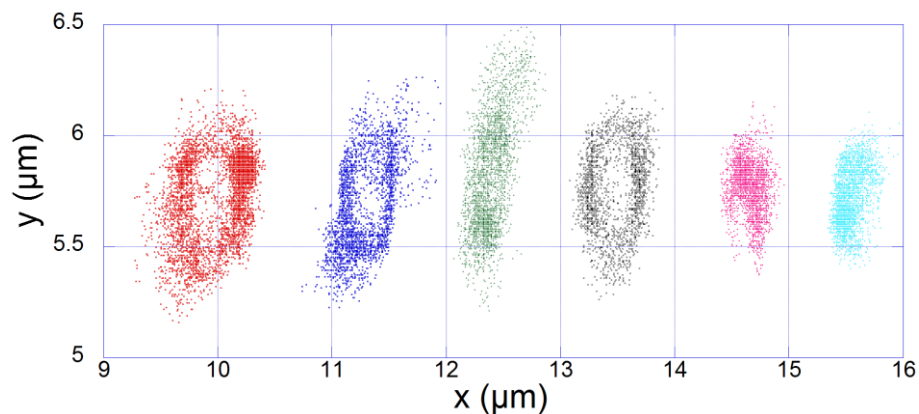


Figure 44: The amplitude of the particle oscillations against the power of the laser. The clouds of points have been separated along the x -axis for clarity. Laser power is as follows, for the cases from left to right, $P_{100x} = 22, 29, 50, 65, 94$ and 108mW .

The two main trends of the oscillations are that both their frequency and amplitude show a dependence on the total power of the laser, P_{100x} . More specifically, the frequency, f_{osc} , is not

Experimental results

simply proportional to P_{100x} , and the amplitude of the oscillatory motions is a decreasing function of P_{100x} . Both of these trends show that these oscillations are not of same nature as those seen in the optical levitation experiments evidenced in Section A-3.3.1, as well as [35, 36, 37], and that thermal noise plays an essential role in the phenomenon. Any model of the oscillations should include both optical and thermal (Langevin) forces. These points will be addressed further in the discussion Section, A-5.

A-4. Numerical simulations

The models used as comparisons for the experimental results of the levitation powers are classical Geometrical Optics (GO), Generalised Lorenz-Mie Theory (GLMT) and Multilevel Fast Multipole Algorithm (MLFMA). Here, GLMT and MLFMA are the rigorous methods, based on Maxwell's equations, whilst GO is an approximation which represents light as a collection of rays.

GLMT results for the levitation powers were obtained for spheres only, using the ABSphere software developed by Kuan Fang Ren [28]. While GLMT calculations for spheroids have been attempted over the years by many people [59], more recently, the modelling of radiation pressure forces using GLMT was theorised for spheroids of low aspect ratio, $k \leq 2$, by Xu et al. [31]. We will not make use of this model, as particles with an aspect ratio $1 < k \leq 2$ are extremely rare in the samples used here. There will be a short overview of GLMT in Section B-2.2.

MLFMA is described well in [40, 60], and so will not be elaborated on in any detail. The model will serve as a rigorous comparison for the levitation powers of all aspect ratio spheroids.

This section is devoted to the results obtained with 2D GO simulations made by J.C. Loudet (JCL). In this method, representation of a laser beam has been simplified greatly by approximating it as a collection of rays. Therefore, the wave nature of light is ignored, with only the intensities of the rays being considered, and the effects of diffraction disregarded. Due to these simplifying assumptions, the method cannot produce quantitatively exact results. However, physically meaningful trends can be obtained, as will be seen. Perhaps most interestingly, the simplicity of this method allows for the calculation of full optical force and torque maps, as well as to tackle dynamical problems such as light-driven particle oscillations.

I was not involved in the development of the GO model, or in its coding; however, I closely interacted with JCL for the duration of this PhD, and hence am aware of how it works. This simulation helped in orienting the experiments and vice versa. For instance, the two-beam levitation experiments were mainly inspired by results from the simulations that predicted the existence of oblique, off-centred, static configurations of the particles. Conversely, the observations made with the optical tweezer setup have been the starting point of a new version of the simulation that deals with the case of a single, large aperture beam. In the following subsections, results that are of direct relevance to the performed experiments are reported,

since they are deemed to be of interest to the reader. Firstly, in Section A-4.2, the case of two small-aperture beams is dealt with (simulating the OL), followed by Section A-4.3, which addresses the simulations performed with a tightly focused beam, equivalent to that of the OT setup.

The simulation is based on a simple ray-optics model of a Gaussian laser beam interacting with a particle. Moreover, the model is limited to 2D, with the particle boundary being a simple ellipse, whereby the rays propagate inside a plane containing that ellipse. As a detailed description of the approach can be found in [37, 39], only a brief outline will be given here.

A-4.1. 2D RO forces and torques

To calculate the particle response to the laser beam in the experiments, we must determine what forces and torques affect the particle as a result of the radiation pressure, as well as include some hydrodynamic components to account for the drag of the medium.

Due to the relative simplicity of the model, and some rough assumptions, it is not adequate to presume that the results obtained with it are quantitatively accurate; however, it can provide a qualitative explanation for some of the experimental phenomena that are observed. It can also prove that only radiation pressure is responsible for these observations.

As previously mentioned, the development of the code was performed by Jean-Christophe Loudet, and is detailed in [39], so this will be a cursory description.

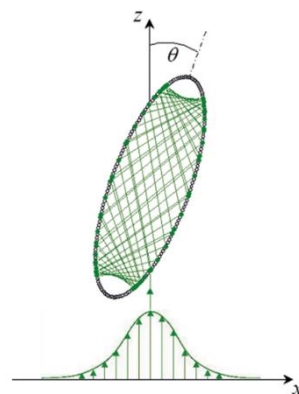


Figure 45: The long axis of the ellipsoid making an angle, θ , with respect to the z -axis. 60 reflections inside the ellipsoid are shown here for illustration. The laser beam has a Gaussian intensity profile along x .

The model involves the approximation of a Gaussian beam using rays. This is done by having a set of N rays, all propagating parallel to, and in the direction of, the positive z -axis, with their

intensities following a Gaussian distribution along the x -axis, as per Figure 45. This being a two-dimensional analysis, and the fact that the interaction plane is also the symmetrical plane of the particle, we can assume that the rays do not diverge into the third dimension. It is worth noting that for each computation, N is checked to make sure that it is large enough, meaning that a high enough number of rays are incident upon the particle, so that there is good detail obtained, yet adding more rays than that does not significantly impact the force and torque values. This amounts to optimising the efficiency of the simulation.

The calculations of the force and torque due to the radiation pressure are performed in the same way as in [55], [61], [25] and [62]. Every ray interacts with the particle surface at certain points, M_j , where every such scattering event has a force contribution of \vec{f}_j , which is proportional to $\frac{n_1 P}{c}$, where n_1 is the refractive index of the medium outside the particle, P is the initial power of the ray and c is the speed of light in a vacuum. For the i -th ray, the total vector force contribution (the summation of all \vec{f}_j associated with that ray) for all scattering events is:

$$\vec{f}_i = \frac{n_1 P}{c} \left[\hat{\mathbf{i}}_0 - R_0 \hat{\mathbf{r}}_0 - T_0 \sum_{j=1}^{\infty} T_j \left(\prod_{k=1}^{j-1} R_k \right) \hat{\mathbf{t}}_j \right] \quad \text{A.21}$$

Here, $\hat{\mathbf{i}}_0$ is the directional unit vector of the incident ray, $\hat{\mathbf{r}}_0$ is the directional unit vector of the first reflected ray, $\hat{\mathbf{t}}_j$ is the directional unit vector of the transmitted ray after j interactions and T_j and R_j are the respective transmissivity and reflectance at interaction j , derived the same way as in Section B-2.3.1. Hence, the effect of polarisation is taken care of by the Fresnel coefficients.

The torque obtained from each scattering event, j , for a given ray, is the expected:

$$\vec{\tau}_j = \vec{r}_j \times \vec{f}_j \quad \text{A.22}$$

where \vec{r}_j is the vector joining the point M_j with the particle centre.

So, the final total force and torque, respectively, acting on the particle can be expressed as:

$$\vec{F} = \sum_i^N \vec{f}_i \quad \text{A.23}$$

$$\vec{\Gamma} = \sum_i^N \vec{\tau}_i \quad \text{A.24}$$

$\vec{\tau}_i$ is the total torque for a given ray (the summation of all $\vec{\tau}_j$ for that ray), and is analogous to \vec{f}_i .

The ray tracing in this model is standard [63], and ceases to apply to a ray once its initial power decreases by a factor of 10^3 . Accounting for rays with an even greater decrease in power does not alter the results significantly.

These calculations are performed for different configurations of the ellipsoid, with $|x| \leq x_{max}$ and $|\theta| \leq \theta_{max}$, where x is the distance between the particle centre and the origin of the coordinate system, and θ is the angle subtended by the semi-major axis of the particle and the positive z -axis, as shown in Figure 45. It is noteworthy to state that the algorithm does not restrict the particle to small excursions only, and lets it move almost completely out of the beam if necessary.

Thus, we can obtain force and torque maps for particles with many aspect ratios and for numerous configurations of x and θ .

However, to present a more complete analysis of the situation, hydrodynamic friction forces are also included, both for translation, \vec{F}_{Hx} , and rotation, $\vec{\Gamma}_{H\theta}$, as well as a buoyancy corrected gravitational force, $\tilde{m}g$, which points in the negative z direction. Inertia forces are negligible due to the low Reynolds number associated with the modelled particles in water. So, to a first approximation, \vec{F}_{Hx} and $\vec{\Gamma}_{H\theta}$ reduce to their Stokes limit:

$$\vec{F}_{Hx} = -\gamma_x \dot{x} \hat{x} \quad \text{A.25}$$

$$\vec{\Gamma}_{H\theta} = \gamma_\theta \dot{\theta} \hat{y} \quad \text{A.26}$$

where γ_x and γ_θ are the translational and rotational friction coefficients along \hat{x} and around \hat{y} , respectively, and the dot represents a time derivative. Also, it is assumed in the above

equations that the translational and rotational frictions are decoupled. The configuration near the top or bottom boundary of the container, where the particle maintains about the same altitude, can be modelled with the addition of a contact force, \vec{F}_c . Assuming that this contact does not influence the hydrodynamic friction greatly, \vec{F}_c can be considered to be a vertical force, acting in the \hat{z} direction. This means that any dynamics that may be revealed using this method are general, and would occur in bulk as well as near a boundary. At the ceiling, \vec{F}_c is equal in magnitude to the radiation pressure force acting along \hat{z} , \vec{F}_z , and creates circumstances which are consistent with experimental procedure [64, 37]. A specific lubrication term, such as that discussed in [38], may be used to enhance the model near the boundaries, however it is not essential here.

To obtain the equations of motion, the net forces and torques acting on the particle amount to zero, so when the particle is free in bulk, and not confined by a boundary, they can be expressed in the limit of a small tilt angle ($\theta \ll \frac{\pi}{2}$) as:

$$\vec{F} \cdot \hat{x} = \gamma_x \dot{x} \quad \text{A.27}$$

$$\vec{F} \cdot \hat{z} = \tilde{m}g + \gamma_z \dot{z} \quad \text{A.28}$$

$$\vec{T} \cdot \hat{y} = -\gamma_\theta \dot{\theta} \quad \text{A.29}$$

where γ_z is the translational friction coefficient in the \hat{z} direction.

However, we are mainly interested in the ceiling configuration due to the experiments that were carried out. Therefore, whilst we may keep Equation A.27 the same, Equations A.28 and A.29 can be collapsed into:

$$\vec{T} \cdot \hat{y} + \tilde{R}\theta\vec{F} \cdot \hat{z} = -\gamma_\theta \dot{\theta} \quad \text{A.30}$$

Here, \tilde{R} is a length, specifically $\tilde{R} = Rk^{-\frac{4}{3}}(k^2 - 1)$, and the term, $\tilde{R}\theta\vec{F} \cdot \hat{z}$, is the torque produced by the combination of the radiation pressure force and the contact of the particle to the top boundary.

Equations A.27 and A.30 are then numerically integrated with a fourth order Runge-Kutta algorithm.

The friction coefficients used here are those derived for three-dimensional prolate ellipsoids. These are, $\gamma_x = 6\pi\eta a G_a$, $\gamma_z = 6\pi\eta c G_c$ and $\gamma_\theta = 6\eta V G_\theta$, where V is the volume of the particle, η is the viscosity of the medium, a and c are the semi-minor and semi-major axes of the ellipsoid, respectively, and G_a , G_c and G_θ are geometrical factors dependant on the particle aspect ratio, which are derived from Perrin's equations [65, 43].

Although this model is rather approximate, and two-dimensional, it has enough rigour to arrive at qualitative agreement with experimental data.

A-4.2. Two-beam levitation

As in most two-beam experiments, it is considered that the ellipsoid is in the “contact” configuration sketched in Figure 4 c). In this case, the vertical component of \vec{F} , F_z , is exactly balanced by the reaction force exerted by the boundary that the particle is in contact with. Gravity is neglected, because the buoyant weight of the particle becomes $\ll F_z$ whenever the laser power $\gg P_{lev}$. It is also supposed that changes in the optical forces and torques which may be due to the proximity of the cell boundary are negligible. These assumptions greatly simplify the problem, and are justified by the fact that the particles were observed to oscillate in very similar ways in bulk water and in contact to the cell ceiling [37].

For a given position of the particle centre, x , and orientation, θ , of the ellipsoid with respect to the beam axis, z , the computed values of \vec{F} and \vec{T} are fed into the equations of motion (written in the limit of small particle tilt angles, where $\theta \ll \frac{\pi}{2}$), which are then further integrated to access the particle dynamics. In the model, the horizontal components of RP forces and torques are balanced by the corresponding Stokes drag terms, as in Equations A.27 and A.30.

When simulating one-beam operation, this simple model performs fairly well at reproducing the observed bifurcation between static states and limit cycles, as the aspect ratio, k , increases [37, 39].

As for the two-beam configuration, it was first predicted by this model that the permanent one-beam PA oscillations could be suppressed through the addition of a second, counter-propagating beam with the same power, meaning $\varepsilon = 1$ [39]. In this symmetrical configuration, the computed phase portrait of a high- k ellipsoid no longer exhibits limit cycles, but rather two pairs of stable focal points located away from the origin. These correspond to non-trivial,

oblique configurations of the ellipsoid. In these cases, the particle is tilted, with its centre slightly off the laser beam axis, as described in Section A-3.2.2 (see Figure 18 a) and Figure 19) [64]. These preliminary results have recently been extended to other values of ε and k , and may be used to build multidimensional bifurcation diagrams, such as the one presented in Figure 46. For a given beam waist, this diagram summarises all the static and dynamical regimes in the (k, ε) plane for ellipsoids in the “contact” configuration of Figure 4 c). This graphic may be divided into three regions. The grey and red regions, containing the black crosses and black solid circles, respectively, correspond to the non-oscillating states, whereas the sustained PA oscillations, marked by the empty blue circles, can be found inside the blue contour. The black crosses in the grey area indicate that the origin point, $(x = 0, \theta = 0)$, is the only stable attractor in the phase portrait. This is not so in the red area, where the origin is a saddle point, meaning that it is unstable. Instead, a variable number of fixed points (either stable nodes or stable focus points) are located away from the origin, corresponding to the aforementioned oblique particle configurations. Some of these configurations coexist alongside limit cycles, within the blue contour (these are marked with a superposition of black solid circles and empty blue ones). The standard number of fixed points in the red and blue areas is four, unless labelled otherwise in the diagram (with the small digits near the solid black circles).

The computed bifurcation diagram of Figure 46 in fact shows good qualitative agreement with its experimental counterpart, Figure 24. Noteworthily, the simulation actually predicts that PA oscillations can be “killed” above some threshold value of ε , which is in turn dependent on k , exactly as has been observed experimentally (see Figure 24). As an illustration of the agreement on the latter point concerning the ε -dependent damping of the oscillations, the plot in Figure 47 confirms that the period of oscillations of a $k = 4.1$ ellipsoid is a drastically increasing function of ε . When $\varepsilon > 0.4$, the ellipsoid eventually stalls and adopts one of the off-centred and tilted configurations mentioned above. Therefore, just like in the experiments, the simulations show that ε is in fact another bifurcation parameter in the two-beam scheme. This leads to the second major experimental finding that is also obtained in the simulations, namely the existence of static, tilted, off-centred configurations of the ellipsoid. Such static configurations can occur with the ellipsoid exhibiting either static, or oscillatory behaviour while ε is very low ($\varepsilon < 0.1$). Once again, this is solidly verified in the experiments.

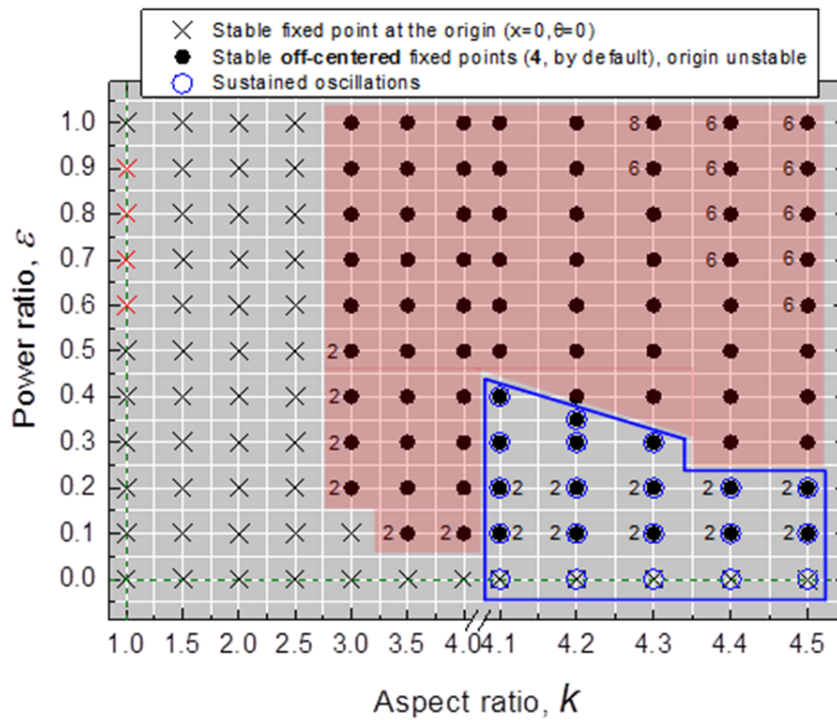


Figure 46: A bifurcation diagram computed by 2D RO in the (k, ε) plane for the two-beam configuration of Figure 4 c). The grey region with black crosses shows the points where the stable configuration for the ellipsoid is at the origin and along the beam axis, $(x = 0, \theta = 0)$. The red area marks the region where the ellipsoids no longer oscillate, and only off-centred fixed points are present. In this area, the origin $(x = 0, \theta = 0)$ is a saddle point, and is therefore unstable. The region encompassed by the blue contour corresponds to a coexistence of limit cycles and fixed points. The digits on the diagram indicate the number of fixed points (4 if no number is shown), which can be either stable nodes or stable focus points (see Figure 49 and Figure 50). The beam waist radius used was $\omega_0 = 1.3\mu\text{m}$.

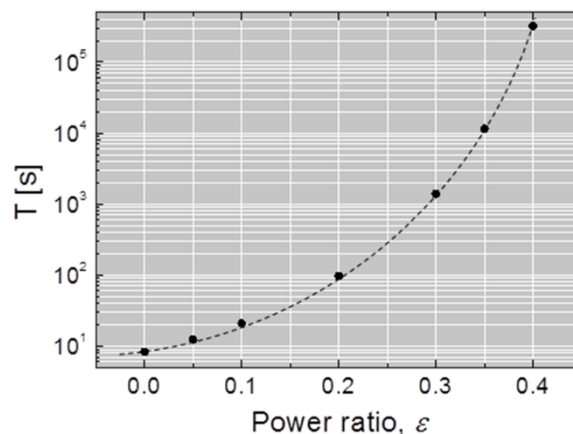


Figure 47: The 2D RO computation of the oscillation period, T , as a function of the power ratio, ε . As can be seen, T increases steeply with ε . When $\varepsilon > 0.4$, the ellipsoid no longer oscillates and adopts one of the oblique configurations mentioned in the text. The dashed line is simply a guide for the eye. Calculation parameters: $k = 4.1$, $\omega_0 = 1.3\mu\text{m}$, and the polarisation is perpendicular to the interaction plane (see [39]).

Trapping an ellipsoid in an asymmetrical configuration like those in Figure 18 a) and Figure 19 may seem unlikely; however, to justify this outcome, let us consider the 2D space, (x, θ) used in the RO simulations. For given values of x and θ , the up-beam exerts a certain force, $F_{\uparrow}(x, \theta)$, and torque, $\Gamma_{\uparrow}(x, \theta)$, on the particle. In general, the down-beam exerts a different force, $F_{\downarrow}(x, \theta)$, and torque, $\Gamma_{\downarrow}(x, \theta)$, because it “sees” a different particle configuration. The symmetry considerations outlined in [39] show that:

$$F_{\downarrow}(x, \theta) = -F_{\uparrow}(-x, \theta) \quad \text{A.31}$$

and

$$\Gamma_{\downarrow}(x, \theta) = \Gamma_{\uparrow}(-x, \theta) \quad \text{A.32}$$

Hence, a fixed point, (x_0, θ_0) , or in other words, a static configuration of the ellipsoid, must satisfy:

$$F_{\uparrow}(x_0, \theta_0) = -F_{\uparrow}(x_0, \theta_0) = F_{\uparrow}(-x_0, \theta_0) \quad \text{A.33}$$

and

$$\Gamma_{\uparrow}(x_0, \theta_0) = -\Gamma_{\downarrow}(x_0, \theta_0) = -\Gamma_{\uparrow}(-x_0, \theta_0) \quad \text{A.34}$$

For non-spherical particles, it is possible to find several sets of points, (x_0, θ_0) , located away from the origin and satisfying the above equalities. This depends on the system parameters, namely the power ratio, ε , and the aspect ratio, k . The simulation offers a convenient way to directly visualise the positions of any fixed points that have been found during the procedure. This is illustrated on the force and torque maps in Figure 48. They were computed for $k = 4.1$ and $\varepsilon = 1$, a situation where only static oblique states are present (see Figure 46). On these maps, a binary colour coding has been used for the total force, $F^{(2)} = F_{\uparrow} + F_{\downarrow}$, and the total torque, $\Gamma^{(2)} = \Gamma_{\uparrow} + \Gamma_{\downarrow}$, meaning that only their signs are kept (+1 or -1), and not their amplitude. In this way, the regions where $F^{(2)}$ and $\Gamma^{(2)}$ change sign and pass through zero are easily resolved, since they appear as sharp boundaries between the two domains. Phase trajectories (the white curves in Figure 48) ending in stable focus points have been superimposed onto these plots. It can be seen that all of these focal points of stability are located only on the sharp borders corresponding to a configuration where, $F^{(2)} = 0$ and $\Gamma^{(2)} = 0$ are simultaneously satisfied. It has been checked, and can be seen in Figure 46, that this

occurs for a great deal of other fixed points, both for particles of different aspect ratios, and across many values of the laser power ratio.

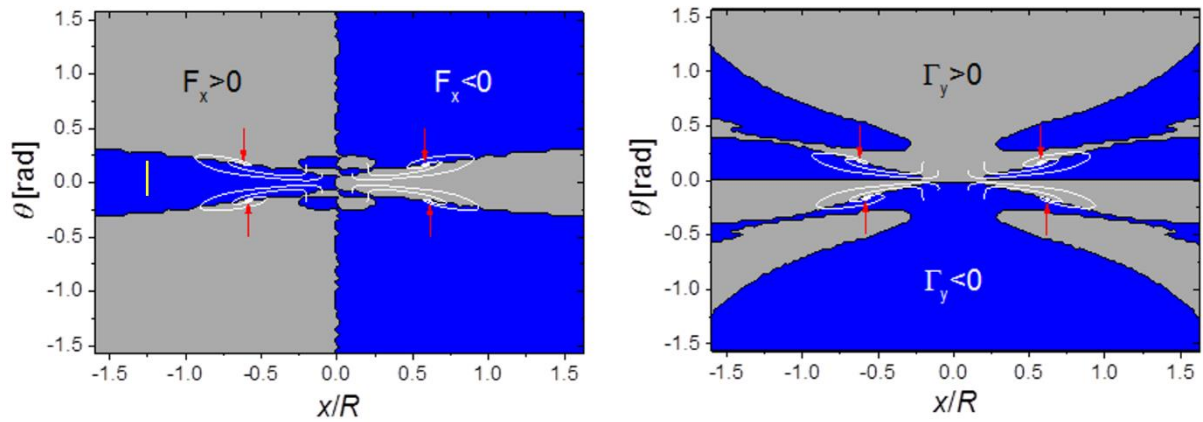


Figure 48: A force map (left) and a torque map (right) calculated using 2D RO for a particle of aspect ratio, $k = 4.1$, with a laser power ratio of, $\varepsilon = 1$, and beam waists of radius, $\omega_0 = 1.3\mu\text{m}$, within a two-beam configuration. The blue regions represent negative amplitudes of the force and torque, with the grey region signifying the positive amplitudes. The white trajectories lead to focus points of stability for the particle (marked by the red arrows), where equilibrium is reached and the forces and torques are balanced. These always occur on the boundary between sign transitions for both the force and the torque. The x and y axes contain the phase space of the simulation, showing the location of the particle centre along the x -axis, and the angle between the long axis of the ellipse and the positive z -axis, respectively.

Even though the simulation is successful in (qualitatively) reproducing some essential trends that were also observed experimentally, it still has severe limitations. For example, when compared to the experimentally obtained bifurcation diagram of Figure 24, the simulations miss the existence of AA oscillations (yellow circles), the *off-centred* PA oscillations (green squares), as well as the irregular motions. This is not surprising, since the AA oscillations, and the irregular motions actually correspond to 3D phenomena, and so cannot be accounted for with a 2D description.

Another source of disagreement concerns the stability of the origin point. For low enough values of k , the experiments reveal that the origin can be a stable fixed point only if $\varepsilon = 0$. Otherwise stated, the particle stands vertically and is centred, only if no power is fed to the down beam. Conversely, simulations predict that the latter configuration persists even when $\varepsilon > 0$, for particles where $k < 3$ (see Figure 46).

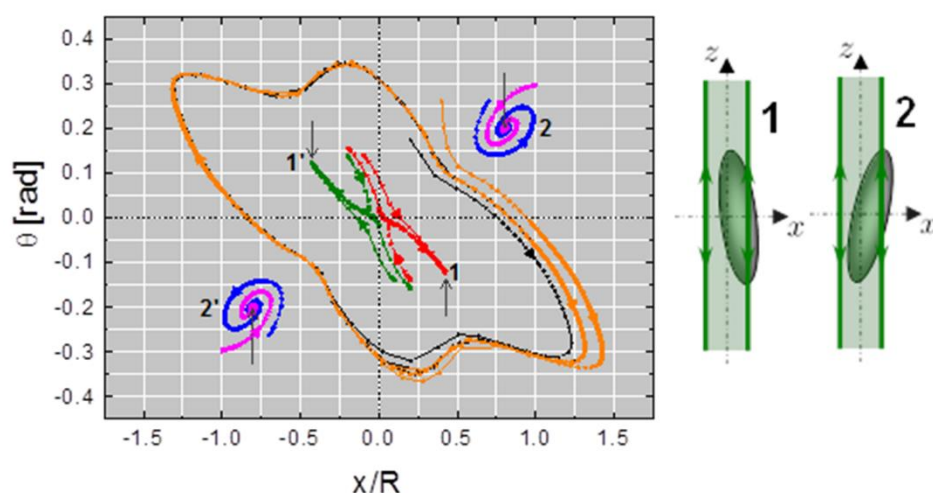


Figure 49: 2D RO simulations of a phase portrait in the two-beam geometry, which exhibits a coexistence between a limit cycle and two pairs of symmetric stable points marked by arrows. The origin point is a saddle point, meaning that it is unstable. The pair of points labeled (1, 1') correspond to stable nodes, whereas points (2, 2') are stable focus points. For each type of point, the approximate position and orientation of the particle are sketched to the right of the plot. Only a few phase trajectories, corresponding to different initial conditions, are shown, for clarity. Calculation parameters: $\varepsilon = 0.3$, $k = 4.1$ and $\omega_0 = 1.3\mu\text{m}$.

The computed phase portrait in Figure 49 shows that static and dynamical regimes may in fact coexist. In this particular example, the limit cycle encompasses a pair of stable node points, while a pair of stable focus points is located outside of it. Depending on the initial conditions, the particle dynamics converge toward one of the co-existing attractors. Such coexistence between static and dynamical regimes is not something that is observed in experiments (see Figure 24). Other phase portraits, such as that of Figure 50, exhibit several pairs of stable focus points, which are generally obtained for high k and ε (see Figure 46 for more examples like this).

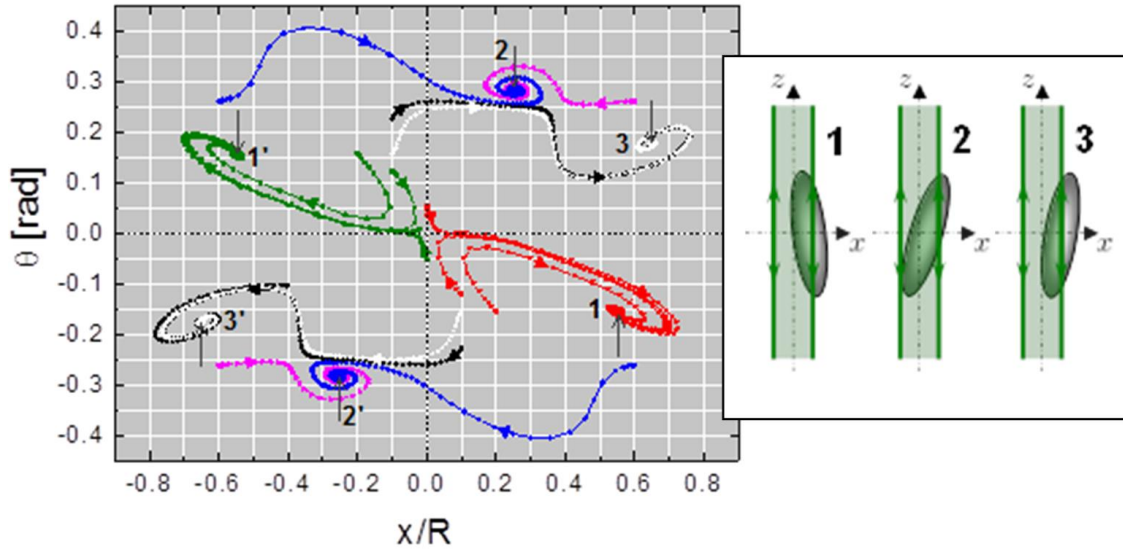


Figure 50: Another example of 2D RO simulations of a phase portrait obtained in the two-beam geometry, this time for $k = 4.4$ and $\varepsilon = 0.7$. As in Figure 49, several pairs of symmetric stable points (marked by arrows) coexist with a saddle point at the origin. These pairs are: (1, 1'), (2, 2') and (3, 3'). The limit cycle evidenced in Figure 49 no longer exists with the present set of parameters. As in Figure 49, the sketches to the right illustrate the approximated oblique configuration of the particle in each case. Only a few phase trajectories are displayed for clarity. The beam waist radius remains as, $\omega_0 = 1.3\mu\text{m}$.

So far, general configurations of the particle (meaning non-zero tilt, as well as off-centring) have only been studied in two dimensions. 3D calculations have begun only for the simplest configuration, where $r = 0$ and $\theta = 0$, for particle which are vertically oriented and centred on the laser axis, as is the case in one-beam levitation experiments for $k < k_c$. In this case, each incident ray remains within the same plane of incidence, and the calculation is just a straightforward generalization of the 2D case. Nevertheless, this “simple” calculation is still useful for a quantitative comparison with experimental values of the levitation power. As can be seen from the diagrams in Figure 17, P_{lev} values calculated this way are in line with the general tendency as k increases.

A-4.3. Single tightly focused beam (optical tweezers)

Here, the case of a tightly focused beam (equivalent to the optical tweezer geometry) will be addressed. The scenario has been sketched in Figure 51. The point denotes as F_V is where the rays would converge if there were no quartz coverslip in the way, and the ray path was submerged in water after the rays leave the oil that immerses the objective. This point is a virtual focus, hence the “V” subscript. Because of the refraction at the QW interface, rays within the water converge to focal points located below the virtual focus, F_V . In the paraxial approximation, one considers rays whose incidence angle is vanishingly small. These rays

converge to the paraxial focus, which is denoted as F_{PAR} in Figure 51. Real rays, corresponding to finite values of the incidence angle, converge to foci located below F_{PAR} . The point, F_{LOW} , corresponds to the maximum incidence angle, which is the same as the aperture, u , of the objective. The fact that the rays do not converge to a single focus, but instead to a series of foci between F_{PAR} and F_{LOW} , is the manifestation of the spherical aberration caused by the interface.

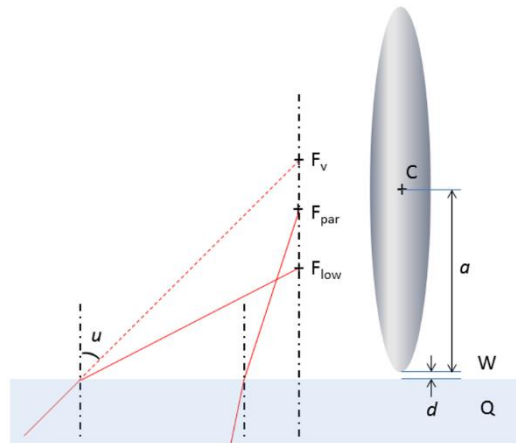


Figure 51: Optical tweezers geometry. The beam focal points, F_V , F_{PAR} and F_{LOW} , as well as the particle configuration, are shown. In principle, the particle self-aligns on the beam symmetry axis when entering the optical trap. The sketch shows the particle separate from the beam axis, for clarity.

Figure 52 shows a quantitative version of Figure 51 which has been obtained numerically using ray tracing, supposing that $u = 60^\circ$. The set of refracted rays generates a zone of high intensity inside a curvilinear boundary. This zone is known as the “spherical aberration caustic”.

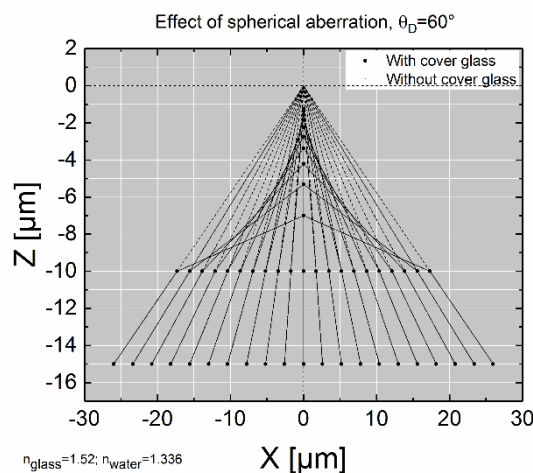


Figure 52: The spherical aberration caustic obtained with numerical ray-tracing. Calculation parameters: $n_{quartz} = 1.52$, $n_w = 1.336$ and the aperture angle, $u = 60^\circ$.

Let the altitude of the QW interface be the origin of the z -axis. The altitude, $z_{F_{PAR}}$, of F_{PAR} , is related to the altitude, z_{F_V} , of F_V , by:

$$z_{F_{PAR}} = \frac{n_w}{n_{oil}} z_{F_V} \quad \text{A.35}$$

with the refractive index of oil assumed to be the same as that of the quartz coverslip, as has been done before in Section A-3.5, meaning that $n_{quartz} = n_{oil} = 1.52$.

The numerical simulation allows the calculation of the forces and torques acting on the particle in the configurations which were experimentally explored in Section A-3.5. During experiments, the 3D-trapping of particles in bulk water was realised. This constituted in the particle being held vertically and centred on the beam axis, with its bottom tip at some distance, d , above QW. A part of the study was dedicated to the case where $d = 0$, meaning that the particle was in contact with the QW interface. In this case, the reaction force from the interface was used to keep the particle at a constant altitude, whilst the position of the beam focus was moved vertically. It was shown that the particle could be maintained in alignment with the beam axis when the focus (F_{PAR} , strictly speaking) is between points T and B, in Figure 37. T corresponds to the equilibrium configuration for the trapped particle in bulk water, while B is the lower limit of the trapping stability.

Analysis of the experimental data led to the general conclusion that the particle centre, C, was slightly below F_{PAR} , no matter what the value of d was, so long as it was positive. This conclusion may seem paradoxical in view of available results from previous calculations, either for spheres [55, 66], or for ellipsoids [56], which lead to the opposite prediction, namely that C should be above F_{PAR} . In other words, the major part of the particle body should be downstream the laser focus. However, the latter prediction only holds in the ideal situation, when spherical aberration is neglected. The influence of spherical aberration on the trapping configuration of a sphere was explored by Fällman & Axner [67, 68]. These authors found that the aberration had the effect of slightly shifting the particle position downwards. The latter conclusion may be reached from intuition. As can be seen from Figure 51 and Figure 52, the presence of the caustic has the effect of creating a continuous set of foci, the average position of which is definitely below F_{PAR} , resulting with the particle experiencing an effective focus located below F_{PAR} as well. Consequently, the equilibrium position of C, the particle centre, is then shifted slightly downward, possibly below F_{PAR} .

Figure 53 and Figure 54 show the results from recent simulations made by J.C. Loudet. The simulation was first performed for spheres, to confirm the results of the literature, after which it was extended to the case of ellipsoids, for comparison with the gathered experimental data shown in Section A-3.5. The graphs show the variation of the vertical trapping force efficiency, Q_z , as the altitude of the particle changes with respect to the beam focus. Q_z is related to the vertical optical force, F_z , by:

$$Q_z = \frac{c}{n_{oil}P} F_z \quad \text{A.36}$$

The variable, z , is defined as the difference in altitude between the particle centre, z_C , and of the virtual focus, z_{F_V} :

$$z = z_C - z_{F_V} \quad \text{A.37}$$

In Figure 53 and Figure 54, the altitude will be dealt without dimensions, using the ratio, $\frac{z}{R}$, where R is the radius of the mother spheres, which in the case of these calculations is, $R = 5\mu\text{m}$.

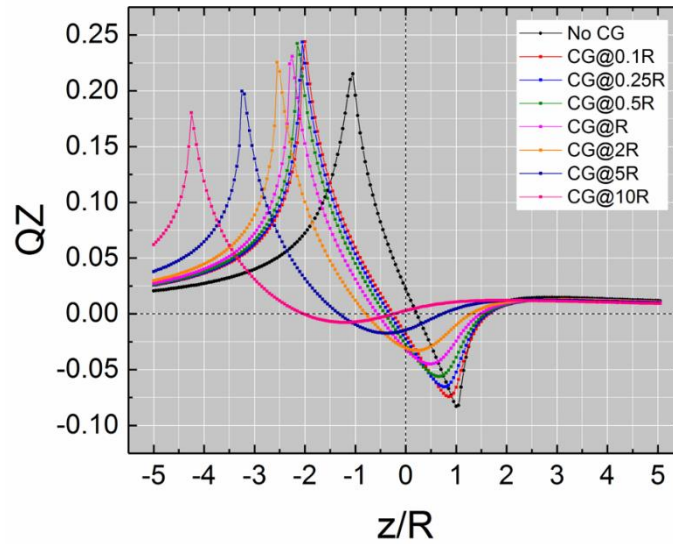


Figure 53: The vertical component of the optical force trapping efficiency, Q_z , against the altitude of the particle, obtained for a simple sphere. The altitude is measured without dimensions, using $\frac{z}{R}$, where z is the difference in altitude between the particle centre and the virtual focus, F_V , with R being the radius of the sphere, in this case, $R = 5\mu\text{m}$. The different colors correspond to different values of d , the distance of the particle bottom from the glass coverslip, CG. This is measured with respect to the radius of the sphere.

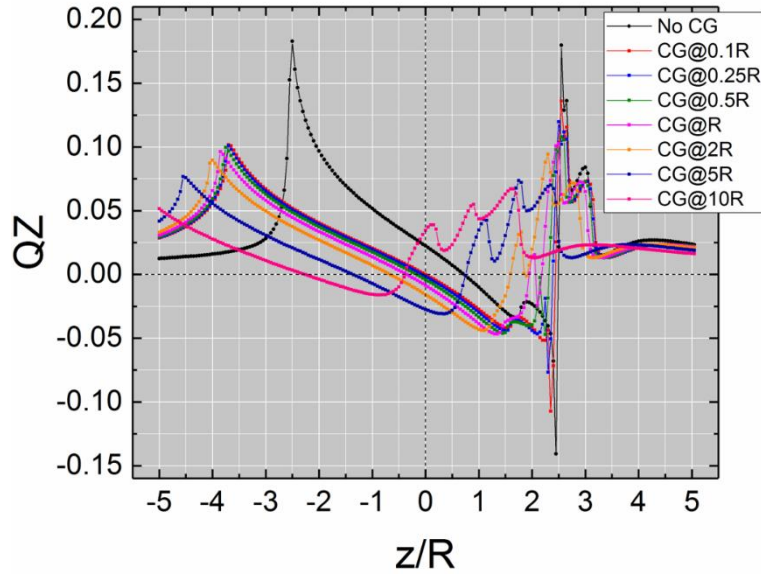


Figure 54: The vertical component of the optical force trapping efficiency, Q_z , against the altitude of the particle, obtained for an ellipsoid with $k = 4$. The altitude is measured without dimensions, using $\frac{z}{R}$, where z is the difference in altitude between the particle centre and the virtual focus, F_V , with R being the radius of the mother sphere, in this case, $R = 5\mu\text{m}$. The different colors correspond to different values of d , the distance of the particle bottom from the glass coverslip, CG. This is measured with respect to the radius of the mother sphere.

The simulation predicts that the particle, be it a sphere, or a prolate ellipsoid, gets stably trapped at the position where the Q_z curve crosses 0 with a negative slope, with the altitude at that point being denoted as $z^{eq} = z_C - z_{F_V}^{eq}$. It can be seen that z^{eq} is positive when the particle is close to $d = 0$, in the absence of spherical aberration, but becomes negative as d increases. Therefore, the general conclusion is that the trapping configuration is quite sensitive to spherical aberration. To compare the computed results with the experimental observations, z must be converted into a variable involving the paraxial focus, meaning $z_C - z_{PAR}$. Based on Equation A.35, it is found that:

$$z_C - z_{F_{PAR}} = \left(1 - \frac{n_w}{n_{oil}}\right)(c + d) + \frac{n_w}{n_{oil}}(z_C - z_{F_V}) \quad \text{A.38}$$

where c , the semi-major axis of the ellipsoid, is related to the mother sphere of radius, R , by $c = k^{\frac{2}{3}}R$. Equation A.38 may then be written in the dimensionless form as:

$$\frac{z_C - z_{F_{PAR}}}{R} = \left(1 - \frac{n_w}{n_{oil}}\right)\left(k^{\frac{2}{3}} + \frac{d}{R}\right) + \frac{n_w}{n_{oil}}\frac{z}{R} \quad \text{A.39}$$

In order to compare the simulation results to the experimental observations, configurations where the particle centre is located below the paraxial focus were needed. This means that the equilibrium state had to satisfy the condition, $z_C - z_{F_{PAR}} < 0$. This translates as:

$$\frac{z}{R} < \left(1 - \frac{n_{oil}}{n_w}\right) \left(k^{\frac{2}{3}} + \frac{d}{R}\right) \quad \text{A.40}$$

By reading the graph in Figure 54, the values relevant to Table 4 may be found:

$\frac{d}{R}$	0.1	0.25	0.5	1	2	5	10
$\left(1 - \frac{n_{oil}}{n_w}\right) \left(k^{\frac{2}{3}} + \frac{d}{R}\right)$	-0.36	-0.38	-0.41	-0.48	-0.62	-1.04	-1.72
$\frac{z}{R}$	0.03	-0.08	-0.18	-0.38	-0.68	-1.38	-2.28

Table 4: Results from the simulation for a $k = 4$ ellipsoid. The position of the particle centre relative to the virtual focus, as the distance of the particle from the bottom boundary of the cell increases.

It can be seen that condition A.40 is satisfied when $\frac{d}{R} \geq 2$. In the experiments, particles stretched from mother spheres with $R = 1.5\mu\text{m}$ were used. The latter condition then translates as $d \geq d_{min} \approx 3\mu\text{m}$, a rather short distance compared to the particle length, where $2c \approx 7.6\mu\text{m}$. Therefore, the simulation predicts that the centre of the particle is upstream of the paraxial focus, as observed in the experiments; however, only when the particle is trapped in bulk water, with a minimum of $3\mu\text{m}$ between itself and the QW interface.

The simulation then correctly reproduces the trend observed in experimentally, except for the case when the particle is very close to the QW interface. Clearly, spherical aberration makes the particle centre shift down to a position below the paraxial focus, when d is large enough. In principle, the aberration becomes too small in the $d \rightarrow 0$ limit for the inversion occur, contrary to what the observations suggest. The reason for this discrepancy is currently unknown. It may be due to the intrinsic limitation of the ray-optics model, which is questionable whenever the characteristic lengths are not large compared to the wavelength (as is the case for d_{min}).

Stability along z is maintained, so long as the slope, $\frac{dQ_z}{dz}$ is negative. This condition remains satisfied when the position of F_V (and simultaneously F_{PAR}) is slightly lowered, as was done in

the experiments (see Figure 37). If, for example, the curve corresponding to $\frac{d}{R} = 0.1$ is chosen from Figure 54, then the altitude at which the sign of its slope changes is $\frac{(z_C - z_V^{REV})}{R} \cong 1.5$. With $R = 1.5\mu\text{m}$, and using Equation A.38, the position of the associated paraxial focus may be deduced, which in this case would be, $z_C - z_{PAR}^{REV} \cong 1.62\mu\text{m}$, and so, $z_{PAR}^{REV} \cong 2.16\mu\text{m}$ for an ellipsoid with $k = 4$. Noteworthily, this prediction has reasonable agreement with the experimental findings for the positions of points A and B in Figure 37. During the experiments, $z_{PAR}(A) \cong 2.45\mu\text{m}$ and $z_{PAR}(B) \cong 2.25\mu\text{m}$ were found for an ellipsoid with an aspect ratio slightly larger than $k = 4$. The prediction of the simulation for the lower limit of stability (in this case, B from Figure 37) then conforms to what is observed in reality.

Currently, the simulations are limited to the calculation of profiles describing the vertical component of the optical force. Simulating the oscillations described in the experimental section is a much more demanding task, as it involves computing full force and torque maps in (x, z) and solving the dynamical equations. This is in progress, and will be the subject of a future publication.

A-5. Discussion

A-5.1. Manipulation of spheres using the optical levitator

Levitation of PS spheres was achieved with powers slightly lower than those predicted by GLMT. The mismatch is almost imperceptible with the large beam waist of $\omega_0 \approx 3.6\mu\text{m}$, as can be seen in Figure 16; however, it is evident with the more focused beam, $\omega_0 \approx 1.7\mu\text{m}$, as shown in Figure 14. The reason of the discrepancy may be looked for within the parameter values of the simulation. Changing the value of the density would not change the $\frac{P_{lev}^{exp}}{P_{lev}^{GLMT}}$ ratio in the graphs showing P_{lev} against v_{sed} , as was explained in that section. The only option left is to alter the refractive index. An instinctive and simple assumption may be that the material of the particles is slightly absorbing, thereby interacting with a fraction of the incident photons in that way. Since absorbed photons completely transfer their momentum to the particle, absorption is more efficient than refraction in producing a levitation force. As shown in Figure 55, agreement is easily obtained by introducing a finite value of the imaginary part of the refractive index. Here, the imaginary part of the refractive index of polystyrene has been set to $n_{PS}^{Im} = 6.7 \times 10^{-5}$. Choosing this value brings the theoretical curves on top of the group of experimental points for both values of the beam waist radius (see Figure 55). It was found that any values within the range of $4.02 \times 10^{-5} \leq n_{PS}^{Im} \leq 6.7 \times 10^{-5}$ provide an adequate correction. A finite non-zero value of n_{PS}^{Im} corresponds to an absorption length given by:

$$l_{abs} = \frac{\lambda_0}{2\pi n_{PS}^{Im}} \quad \text{A.41}$$

When $n_{PS}^{Im} = 6.7 \times 10^{-5}$, Equation A.41 gives $l_{abs} \approx 1.22\text{mm}$, meaning that more than 50% of the laser power is absorbed when passing through a 1mm layer of the particle material. Such a high loss is clearly unrealistic when dealing with polystyrene alone; however, this cannot be ruled out in the case of the particle material, since it is not pure polystyrene. It should be noted that if this was indeed the absorption length of the particle material, then only $\approx 1\%$ of the power would be attenuated. The transparency of PS spheres was checked by drying a small sample of them, then submerging the particles in a high refractive index liquid ($n \approx 1.57$, provided by Cargille) to see if all the light passed through. The particles looked almost invisible within this liquid, and displayed no attenuation effects, so therefore do not absorb.

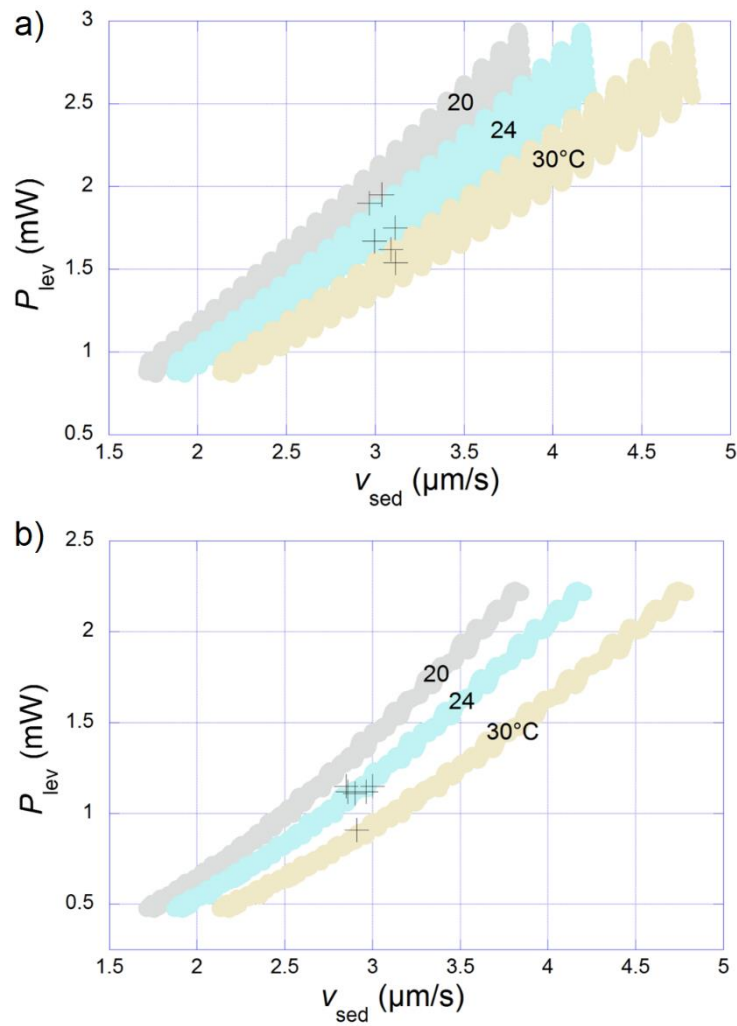


Figure 55: The effect of introducing absorption. Calculation parameters: $n_{pS}^{Im} = 6.7 \times 10^{-5}$, $R_0 = 5\mu\text{m}$, a) $\omega_0 = 1.70\mu\text{m}$ and b) $\omega_0 = 3.60\mu\text{m}$.

The possible small absorption is presumably not enough for the particle to heat up and generate a convection flow strong enough to compete with the optical levitation forces. Indeed, there seems to be no such manifestation, as far as can be gathered from the $P_{\uparrow} - P_{\downarrow}$ against $P_{\uparrow} + P_{\downarrow}$ graph (see Figure 56). The test does not show any definite negative slope that could be interpreted as laser-induced heating and convection.

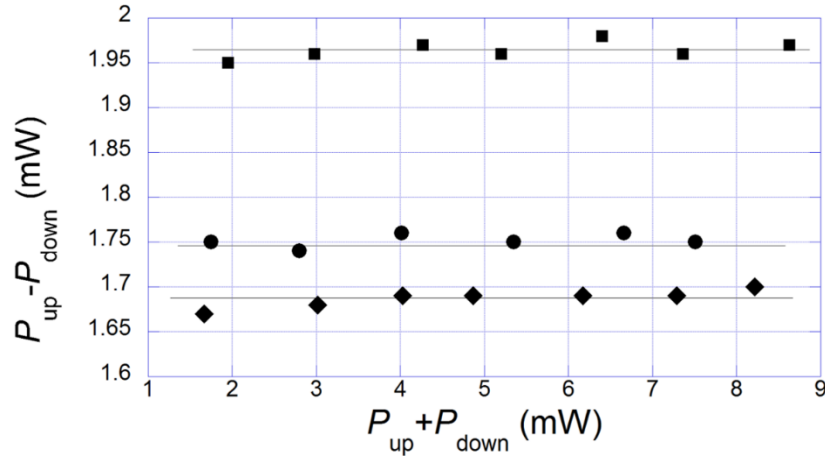


Figure 56: Power difference against total power experimental results performed with PS particles of radius $R_0 \approx 5\mu\text{m}$.

A-5.2. Manipulation of ellipsoids using an optical levitator and optical tweezers

In this thesis work, we have reported observations of the mechanical responses of polystyrene spheroidal particles to laser light, first in a two-beam levitation setup and then in the classical optical tweezer geometry. Water was the continuous medium around the particles in both cases.

A-5.2.1. The optical levitation experiments

These experiments were designed as an extension of the work of Mihiretie on the response of ellipsoids to a single moderately focused laser beam [35, 36, 37]. The responses of such particles to the standard configuration of two counter-propagating beams was systematically explored. It was found that particle responses could be sorted as either static or dynamical states, depending on the ellipsoid aspect ratio, k , and on the power repartition between the two beams, ε . The many observed responses could therefore be gathered into a general state diagram (see Figure 24), with k and ε as the control parameters.

The polar-angle oscillation mode (PA), discovered by Mihiretie et al., was confirmed and generalised to continuous values of ε . Moreover, two new modes of oscillation were also evidenced. These are the off-centred PA and the conical azimuthal motion (AA).

The possibility to “kill” PA oscillations, which had been predicted by 2D RO simulations by J.C. Loudet [39], has been experimentally proven within large intervals of both k and ε values. The configuration of the ellipsoid in such condition is non-trivial, as the particle not only rests off the beam axis, but is also tilted, meaning that it has finite values of Δr and θ . This case is especially interesting as a validation method for theoretical simulations, due to the unique combination of forces and torques necessary to produce such a static state.

AA oscillations seen with our ellipsoids may be similar to motions observed by Neves et al. with nanofibers [11]. These authors used a standard OT geometry with a linearly polarized Gaussian beam ($\lambda = 800\text{nm}$), carrying neither spin, nor orbital angular momentum. The nanofibers had subwavelength diameters, with lengths in the range, $10 - 100\mu\text{m}$, and could be trapped either at the sample boundary (water-quartz interface), or in bulk water. In both cases, the particles were seen to rotate at a constant rate around the trapping point, provided a high enough tilt angle existed between the nanofiber axis and that of the beam axis. Based on T-matrix calculations, Neves et al. verified that the observed motions could be driven by optical torques in the configuration of their experiment. However, and as far as we know, no theory was proposed to explain how the particle self-orientates and positions itself across the laser beam to produce a geometry that leads to continuous rotation. In our case, we evidenced AA oscillations, meaning that the motion seemingly reverses, with the particle moving back and forth between two boundary azimuthal positions. The mechanism that causes this reversal is not known yet.

A-5.2.2. The experiments with optical tweezers

These experiments were aimed at observing the behaviours of ellipsoids in a tightly focused beam (contrary to the weakly focused case of the previously discussed OL), with an aperture large enough to produce three-dimensional trapping. Indeed, 3D trapping was easily achieved with all particles, no matter the aspect ratio. Every particle was trapped vertically in an on-axis configuration. The position of the particle could be characterised within the laser beam focal zone, and it was possible to test the stability of the trap equilibrium when the focus was moved along the symmetry axis of the particle. It was found that the particles were trapped with the laser focus located between the centre and the top extremity of the particle. Otherwise stated, more than half of the particle body was located upstream of the laser focus. This finding adheres to observations made by Neves et al., in their experiments with polymer nanofibers [11], as well as by Toe et al., with indium phosphide nanowires [69]. Both cited articles show sketches with the laser focus located above the centre of the trapped rods. However,

simulations using the Discrete-Dipole-approximation (DDA) [56] led to the opposite conclusion, that a trapped ellipsoid should have its centre downstream the laser focus. The discrepancy between the observed and calculated configurations may arise from the fact that the oil-water interface in the real system modifies the structure of the laser beam focal zone by producing spherical aberration [67], as well as losses through reflection. This is discussed in detail in Section A-4.3.

A-5.2.3. Nonlinear versus noise-driven oscillations

Rather intriguingly, with the OT setup, each tested particle was observed to undergo polar angle oscillations whenever the laser focus was brought within a narrow region close to the bottom tip of the particle (between A and B in Figure 37). Such oscillations, as is argued below, are different from those seen in the levitation experiments.

Standard PA oscillations of the type reported in Section A-3.3.1, denoted from now on as PA_{osc}^{lev} , are periodic, corresponding to a sharp peak in the Fourier spectrum [37]. Mihiretie et al. showed that the frequency of PA_{osc}^{lev} is proportional to the laser power, so $f_{osc} \propto P$, while their amplitude is virtually unaffected by it.

Conversely to PA_{osc}^{lev} , oscillations within the 3D trap of the optical tweezers, PA_{osc}^{OT} , are very noisy, with the corresponding broad peak in the power density spectrum that comes with that kind of motion (see Figure 41). The frequency of PA_{osc}^{OT} increases with P , but the relation is not a simple proportionality. There seems to be a lower limit in P , below which the particle does not oscillate (see Figure 42). Another difference resides in the amplitude of the oscillations. While the amplitude of PA_{osc}^{lev} is independent of P , that of PA_{osc}^{OT} decreases with it (see Figure 44), further suggesting that PA_{osc}^{OT} is noise-driven.

A model has been proposed by Mihiretie et al. to explain the existence of PA oscillations in the levitation experiments [39]. This model is two-dimensional, meaning that the coordinates describing the particle motion are reduced to x (the distance of the particle centre to the laser beam axis), z (the vertical motion of the particle centre), and θ (the tilt of the longest axis of the ellipsoid with respect to the positive z -axis). The particle is then assumed to be in frictionless contact with the ceiling of the cell, and gravity is neglected (with the latter assumption being valid whenever $P \gg P_{lev}$, as is the case in most of the experiments). Moreover, the model is limited to small values of θ , a further simplification which allows the vertical motion of the particle centre to be neglected, meaning that $z \approx constant$. Based on

these assumptions, the equations for the particle motion can be expressed by Equations A.27 and A.30, for the optical force and torque, respectively.

Properties of the frequency and amplitude of the oscillations are best found by writing the above equations, A.27 and A.30, in terms of dimensionless quantities, which are defined as follows:

$$\bar{x} = \frac{x}{R_0} \quad \text{A.42}$$

$$\bar{z} = \frac{z}{R_0} \quad \text{A.43}$$

$$\bar{F}_i = \frac{F_i c}{P} \quad \text{A.44}$$

$$\bar{\Gamma} = \frac{\Gamma c}{P R_0} \quad \text{A.45}$$

$$\bar{\gamma}_x = \frac{\gamma_x}{\eta R_0} \quad \text{A.46}$$

$$\bar{\gamma}_z = \frac{\gamma_z}{\eta R_0} \quad \text{A.47}$$

$$\bar{\gamma}_\theta = \frac{\gamma_\theta}{\eta R_0^3} \quad \text{A.48}$$

$$\bar{t} = \frac{t}{\tau} \quad \text{A.49}$$

with the characteristic time, τ , being:

$$\tau = \eta R^2 \frac{c}{P} \quad \text{A.50}$$

Equations A.27 and A.30 can now be expressed as:

$$\bar{F}_x = \bar{\gamma}_x \frac{d\bar{x}}{d\bar{t}} \quad \text{A.51}$$

$$\bar{\Gamma} + \bar{R}\theta\bar{F}_z = -\bar{\gamma}_\theta \frac{d\theta}{d\bar{t}} \quad \text{A.52}$$

From the structure of Equation A.50, one can deduce that the solution can be expressed as:

$$\bar{x} = X(\bar{t}) \quad \text{A.53}$$

$$\theta = \Theta(\bar{t}) \quad \text{A.54}$$

Equations A.53 and A.54 prove that the amplitude of the oscillations does not depend on the laser power. The latter parameter only intervenes through the characteristic time, τ . Increasing P only amounts to decreasing the period of the oscillations, which is proportional to $\frac{\eta R^2}{P}$.

Equations A.27 and A.30 can be generalised into a compact form that is written:

$$\Phi(\mathbf{q}) = \zeta \dot{\mathbf{q}} \quad \text{A.55}$$

Here, $\mathbf{q} = (x, \theta)$ is what defines the configuration of the particle, and ζ is the friction matrix. In this case, the friction matrix is assumed to be diagonal, as it is in the analysis of Mihiretie, although this assumption is not necessary.

$$\zeta = \begin{pmatrix} \gamma_x & 0 \\ 0 & -\gamma_\theta \end{pmatrix} \quad \text{A.56}$$

with Φ being defined as:

$$\Phi(\mathbf{q}) = \Phi(x, \theta) = \begin{bmatrix} \mathbf{F}_x \\ \bar{\Gamma}_y + \bar{R}\theta\bar{F}_z \end{bmatrix} (x, \theta) \quad \text{A.57}$$

It should be noted that the optical forces and torques depend on the translational and rotational degrees of freedom of the particle in a very complex way. Φ is therefore a nonlinear operator acting on \mathbf{q} .

The simplest and most standard trapping configuration is when $(x = 0, \theta = 0)$. To know whether the particle can be optically trapped amounts to knowing if $(0, 0)$ is stable or not. To find out if this condition is true, one takes the linear limit of Equation A.55:

$$\Phi_{lin}(\mathbf{q}) = \zeta \dot{\mathbf{q}} \quad \text{A.58}$$

$$\mathbf{L}(\mathbf{q}) = \zeta^{-1} \cdot \Phi_{lin}(\mathbf{q}) = \dot{\mathbf{q}} \quad \text{A.59}$$

The linear operator Φ_{lin} is obtained by expanding $\Phi(\mathbf{q})$ to the first order in (x, θ) , near $(0, 0)$. The explicit form of \mathbf{L} is a 2x2 matrix, namely the “stiffness matrix”, of the optical trap. In general, there is no reason why the off-diagonal terms of \mathbf{L} , namely $(x\theta)$ and (θx) , should be equal. Due to the non-equivalence of $(x\theta)$ and (θx) , \mathbf{L} is a non-symmetrical matrix. An interesting situation occurs when \mathbf{L} has complex conjugate eigen-values:

$$\lambda_{1,2} = \lambda' \pm i\lambda'' \quad \text{A.60}$$

When the real part, λ' , is negative, then $(0, 0)$ is a stable trapping configuration. In the (x, θ) configuration space, $(0, 0)$ is a “stable focus point”. Stability translates as shown in Figure 57 a). When the system is pushed off $(0, 0)$, it always comes back to $(0, 0)$. Note that the trajectory is a spiral. This is due to the imaginary part of the eigenvalues, which makes the (x, θ) point rotate around the origin. In practice, $(0, 0)$ corresponds to the particle lying vertically, as well as being centred on the laser beam axis. When the particle is pushed off this position by some perturbation, it comes back to the origin through a few oscillations that are coupled in position and tilt angle. The amplitude of these oscillations vanishes as the particle comes closer to $(0, 0)$.

When λ' is positive, $(0, 0)$ is unstable. The particle moves off the $(0, 0)$ configuration in both x and θ . The trajectory is a spiral, for the same reason as above (see Figure 57 b)). The particle again makes oscillations, but this time of growing amplitude. The simulation does not go further, because the linear analysis only deals with the early steps of the motion, when $x \ll R_0$, and for infinitesimal θ . Once x and θ become large enough, only the full nonlinear analysis can describe the evolution of the system.

A model of the nonlinear evolution of the system has been proposed by Mihiretie et al. [37]. The model is based on a simple analytical form for Equation A.55:

$$\begin{aligned} \dot{x} = X(x, \theta) = & G(x)G(\theta - 1) - G(x)G(\theta + 1) - G(x - 1)G(\theta) \\ & + G(x + 1)G(\theta) \end{aligned} \quad \text{A.61}$$

$$-\dot{\theta} = Y(x, \theta) = A \cdot [G(\theta + u)G(x - t) - G(\theta - u)G(x + t)] \quad \text{A.62}$$

In Equations A.61 and A.62, G is the Gauss function. $t \geq 1$ and $u < 1$ are positive constants. A is a positive parameter representing the amplitude of the torque, and is an increasing function of the ellipsoid aspect ratio, k . The above equations have been built as a schematic representation of the main features of the force and torque maps calculated from a ray-optics model [37, 39]. The ray-optics based simulation did show the same standard PA oscillations as those seen in levitation experiments. The authors verified that the dynamical system based on Equations A.61 and A.62 showed the same types of dynamical regimes and bifurcation as seen in the numerical simulation and the experiments. These models, either in the basic numerical version, or in the simplified form of Equations A.61 and A.62, are only valid as qualitative representations, but are still relevant, since they capture the main physical features of the dynamics of ellipsoids illuminated by the beam of an optical levitator. Numerical integration of Equations A.61 and A.62 yields the trajectories shown in Figure 57 a) and b).

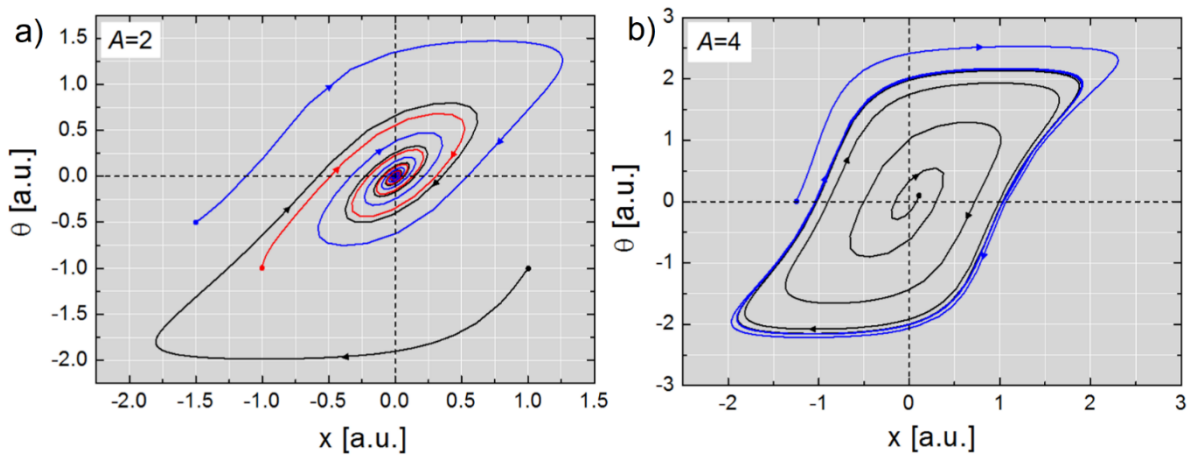


Figure 57: These graphs show trajectories obtained via the integration of Equations A.61 and A.62. The graphs are taken from [37]. Here, $t = 0.5$ and $u = 0.5$. a) shows the case where $A = 2$, and the particle is stably trapped.

b) shows the case where $A = 4$, with the particle not stably trapped, and instead undergoing permanent nonlinear oscillations.

Linearization of Equations A.61 and A.62 near $(0, 0)$ yields an explicit form of $L(\mathbf{q}) = L(x, \theta)$, [37]. The stiffness matrix has complex conjugate eigenvalues (Equation A.60) in a large interval of A , more specifically $0.44 \leq A \leq 14.97$. For $A = 2$, the central point, $(0, 0)$, is a stable focus point, with the particle being trapped, as per Figure 57 a). A small value of A corresponds to a small aspect ratio, with destabilisation occurring at $A_c \approx 2.57$. For $A > A_c$, i.e. for a more elongated particle, the $(0, 0)$ configuration is spirally unstable. The divergence saturates on a limit cycle, whose amplitude increases with A . In practice, this limit cycle translates as periodic

PA oscillations of the type seen in the levitation experiments (P_{osc}^{lev}). These oscillations are termed “nonlinear”, since they clearly originate from the nonlinear character of the equations dictating the motion of the particle.

The linearized version, Equations A.58 and A.59, cannot produce sustained oscillations. This conclusion holds within the above analysis in so far as thermal noise is neglected. Thermal agitation of the water molecules is the source of the Brownian motion of the particle. In most of the experiments, either in levitation or with optical tweezers, thermal noise is visible as small fluctuations of the particle position. These fluctuations are very small on the scale of the particle size and then can be viewed as small noise, which can be neglected in order to adhere to the “zero-temperature” description of the particle dynamics. However, thermal fluctuations may become non-negligible if the laser power is small, or if the system comes close to the limit of linear stability.

The equation of motion for a particle including thermal noise can be expressed as follows:

$$\Phi(\mathbf{q}) = \zeta \dot{\mathbf{q}} + \mathbf{f}^L(t) \quad \text{A.63}$$

Here, $\mathbf{f}^L(t)$ is the Langevin force, which is usually modelled as white noise with a mean value of zero. Equation A.63 is a very complex stochastic nonlinear differential equation, which has not yet undergone a systematic study. Simpson and Hanna [56] (hereafter referred to as SH) have thoroughly analysed the linear limit of the equation:

$$\Phi_{lin}(\mathbf{q}) = \zeta \dot{\mathbf{q}} + \mathbf{f}^L(t) \quad \text{A.64}$$

Linearizing Equation A.63 is legitimate in describing small fluctuations of an ellipsoid which is optically trapped. In this case, the system is within the linear stability regime, and the fluctuations consist of quasi-infinitesimal random excursions in (x, θ) . As shown by SH, the Langevin force is sufficient to permanently induce cyclic motion in the particle configuration (see the closed orbits in Figure 58). It should be noted that the orbits are averages obtained by superposing many repeated calculations of the particle motion in (x, θ) space. In reality, the particle undergoes what SH term as a “stochastic flapping motion”.

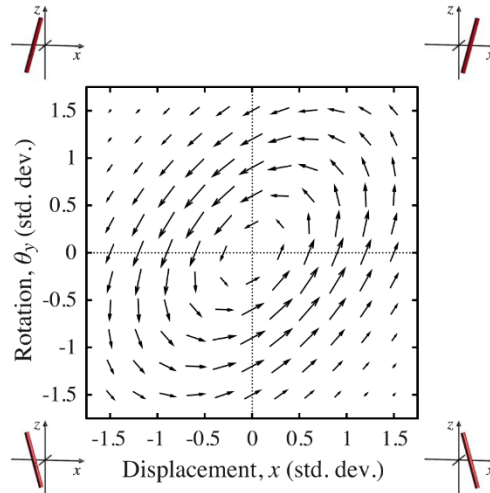


Figure 58: SH orbits (extracted from [56]). The graph shows lines of the probability current describing the time evolution of the particle configuration.

The stochastic character of the cyclic motion should be visible in $x(t)$, $\theta(t)$ time sequences as periodic signals with strong amplitude and phase fluctuations. According to the analysis of SH, the frequency of the signal increases with the laser power. However, increasing P increases the stiffness of the trap and restricts particle excursions to a smaller zone around $(0, 0)$, resulting in decreased amplitudes for the signals.

Toe et al. [69] have reported observations of “resonant fluctuations in the stochastic motion of optically trapped nanowires”, and interpreted their observations with a model of their own (based on specific linear equations for the optical forces and the particle hydrodynamic drag). The motion of the particle was observed indirectly through fluctuations of the intensity in the back focal plane of the microscope. The recorded signals showed characteristic broadband resonance peaks in the kHz domain. From reading the paper, it is not clear to us how the amplitude and frequency of the nanorod motions would depend on the laser power.

The observations reported here, in Section A-3.5, are presumably a direct illustration of “SH oscillations”. Video records unambiguously show the cyclic motion of the trapped particle, consisting in off-centring and tilting of the ellipsoids. The graph in Figure 41 a) approximately represents the angular motion corresponding to such noise driven oscillations, $\theta(t)$. The cyclic character of the motion is evident in spite of the many phase defects. The corresponding spectrum (shown in Figure 41 b)) displays a characteristic broad peak around $f_{osc} \sim 10\text{Hz}$. It was confirmed that the resonance frequency, f_{osc} , increases with the laser power in an approximately linear way. The graph in Figure 42 suggests that the oscillations disappear when the power becomes too low, which is estimated to be for $P \leq 12\text{mW}$. The tendency for

the amplitude, as is shown in Figure 44, is to decrease with P , which is once again a characteristic synonymous with SH oscillations.

As put forward in [56], the conditions necessary for SH oscillations to be observable may be difficult to satisfy. Of the OT experiments presented in this body of work, those concerned with ellipsoids optically trapped in bulk do not show SH oscillations, at least within the resolution of the video records. Oscillations become evident when the laser focus is moved down close to the lower tip of the particle, in the [A, B] interval of Figure 37, using the quartz-water interface to block the particle vertically. It is presumed that the focused laser beam still functions as a stable optical trap in this interval, but with very small stiffness constants. The small stiffness offers a twofold advantage. Firstly, it allows for excursions to be large enough (on the order of $\sim 0.5\mu\text{m}$) to be directly visible in the microscope images, and secondly, the oscillation frequencies are low enough to be easily resolved in the recorded video sequences.

A-6. Conclusion of Section A

Levitation powers were measured for PS spheres ($R_0 \approx 5\mu\text{m}$) with weakly and moderately focused beams ($\omega_0 \approx 3.6\mu\text{m}$ and $\omega_0 \approx 1.7\mu\text{m}$, respectively). Experimental values of the levitation power, P_{lev}^{exp} , were slightly lower than those predicted by GLMT, P_{lev}^{GLMT} , for standard values of the density and refractive index of such particles. The difference is within the experimental uncertainty when $\omega_0 \approx 3.6\mu\text{m}$, but is beyond that ($\sim 30\%$ on average) with the more focused beam. Based on this finding, it is speculated that the particles slightly absorb the green laser light. Assuming absorption of 0.5% to 1% of the laser power by the particle is enough to reconcile the experimental data with the simulation.

On practical grounds, it is concluded that the experimental procedure based on estimating the maximum value of the levitation power in the vicinity of the beam waist plane has been successfully tested, and is therefore reliable. An essential outcome was to verify that the optical levitation force is proportional to the laser power, and that no bias due to laser-induced heating or nonlinear effects is present with PS particles. The fact that the proportionality constant (or in other words, the levitation efficiency) is observed to be higher than that of GLMT indicates that the index of refraction of the particles may not be purely real, and instead has a small imaginary part, with n_{ps}^m being of the order of 10^{-5} . This may be due to molecular absorption, or to scattering by nanometre scaled inhomogeneities inside the particle structure.

The effect of n_{ps}^m is small in practice, and as such, will be ignored in the study about ellipsoids.

Different types of static and dynamical responses of polystyrene spheroids in optical levitation (OL) and optical tweezer (OT) geometries have been observed.

The characteristics of static configurations may serve as stringent tests for theories and numerical simulations of optical forces.

MLFMA and basic ray-optics were compared for P_{lev} values of ellipsoids of varying k , for the basic $(0, \theta)$ configuration. The results from the experiments and the theories show similar tendencies as functions of k ; however, all of them are somewhat scattered. At this stage, simple one-beam levitation seems to be hard to exploit for quantitative tests.

Oblique and off-centred static configurations seen in two-beam manipulations using the OL are of special interest because the powers of both beams may be high enough for gravity to

become negligible. Then, only optical forces and torques are involved in the particle equilibrium. Most interestingly, forces and torques combine in a non-trivial way to produce a tilted configuration. The existence of such configurations has been predicted from simple ray-optics [39, 64], but a true quantitative description can only be obtained using a wave theory of the interaction. The latter point has not been explored yet.

Different types of oscillatory motions were observed with ellipsoids, both for the OL and OT experiments. In the discussion it was insisted that a distinction be made between nonlinear oscillations, the type seen in OL experiments, and noise-driven (“SH”) oscillations. Each type of cyclic motion has its own distinctive characteristics, which were described, but both stem from the fundamentally non-conservative nature of optical forces. The existence of permanent motions of particles in laser beams in some (but not all) circumstances highlights the fact that the mechanical responses of particles to laser light do not simply amount to a binary choice of either being in a stable state, or undergoing expulsion from the beam. These responses must instead be viewed as dynamical states, in general.

The 2D ray-optics simulations correctly reproduced the main trends observed experimentally. The agreement is mostly qualitative, as the model cannot pretend to yield accurate values for the optical forces or torques, of boundaries of stable equilibrium domains, or of bifurcation thresholds. However, the simulation yields enough information for the user to identify the main physical mechanisms at work in many experimental situations.

The real experimental system is of course in 3D, but most of the important observations can be roughly understood on the basis of a 2D description. Naturally, some phenomena cannot be accounted for by this model, as they are intrinsically 3D. For instance, real systems can produce chaotic oscillations, while chaos is impossible in 2d.

The main weakness of ray-optics (RO) resides in the neglecting of the wave nature of light. A great deal of progress is to be expected from the dressing of rays with wave properties, as is done in VCRM, even just for a 2D model. The latter method would allow testing of the influence of phases on force and torque calculations in a very direct way. One might then test the validity of RO quantitatively, instead of just obtaining the large approximations it currently provides, which can only even be considered reasonable when all characteristic sizes are much larger than a wavelength.

Part B

Vector Complex Ray Model

B-1. Introduction

Light is one of the most fundamental features of our universe. It is one of the main reasons why there is even life on Earth. As if this were not enough, light continues to be increasingly useful to the human race in the form of a probe, to see the things around us that are not apparent with the naked eye, whether they be as small as a bacterium, or as large as a distant galaxy.

Whenever light interacts with an object, its response gives away a lot of information about what exactly it interacted with, for example: shape, size, colour, temperature and refractive index. To be able to know these properties for objects that cannot be seen directly by eye, the nature of light must be understood to a very high degree. This is of great interest in fields where small particles are involved, ranging in size from hundreds of nanometres, to hundreds of micrometres. There is nowhere in life where small particles are not involved. This could range from aerosols in the atmosphere, to bacteria in a laboratory. In order to know exactly what is being dealt with, often the best thing to use is light.

In cases where samples of small particles require rapid characterisation, a good way to approach this problem is to observe the intensity of light being scattered by the particles, then use theoretical models to predict the properties of the sample contents. This may be done for suspensions containing many particles, to find average sizes and shapes, or for single particles, often using microfluidics to funnel them across a laser beam of light, in order to find properties on a more individual basis [70]. The latter is of high value in bioparticle discrimination, although the technique could be used for many other applications also.

The theoretical models that simulate the scattering of a laser beam of light by small particles are many and varied, with the most prominent being Generalised Lorenz-Mie Theory (GLMT) [59], T-Matrix [71, 72], Discrete Dipole Approximation (DDA) [73, 74], Finite Difference Time Domain (FDTD) [75], and Geometrical Optics (GO) [72, 76, 77, 78], although this is by no means an exhaustive list.

All of these models have advantages and disadvantages. GO, whilst being a rough approximation, is very fast and can be applied to arbitrarily shaped particles of large size. GLMT is a rigorous and accurate model, but has size and shape limitations. The T-matrix formulation is very efficient for particles of comparable size to the wavelength, however, the integration is one dimensional only if the particle has rotational symmetry, so the calculation

is somewhat more demanding otherwise. DDA and FDTD are volume discretised methods, both of which need to be fully performed each time the incident angle of light is changed, which matters a lot if there are many randomly oriented particles. DDA shows slow improvement in accuracy as the number of discrete volumes is increased, however only the scatterer needs to be discretised in such a way [1]. FDTD on the other hand has to be applied over a spatial domain larger than the particle, and must be discretised by cells with lengths much smaller than the wavelength, which poses a problem for large particles [79, 1].

VCRM is a novel method, the fundamental basis of which lies in GO. It is intended for the calculation of light scattering by large (on the order of tens, or hundreds of micrometres) arbitrarily shaped particles. It combines ray optics with wave properties to create a simulation that can potentially provide reasonable accuracy with a lot less processing power.

VCRM has been well established for plane wave scattering by infinite cylinders [4], spheres, and ellipsoids [2, 3]. It has been validated theoretically using LMT and MLFMA [6], as well as experimentally with acoustically trapped droplets [5].

The next step is to extend the model to include Gaussian beam scattering by spherical and ellipsoidal particles, which is the subject of this, Part B of the thesis.

In Section B-2, some classical models for light scattering are discussed, namely LMT, GLMT and GO. GLMT will later be used as the rigorous comparison for all of the numerically calculated scattering patterns for spherical particles. Section B-3 contains the fundamental principles behind VCRM, with Section B-3.2 specifically focusing on the Gaussian beam case. The numerical results, as well as a discussion, are presented in Section B-4. Finally, Part B is concluded in Section B-5.

B-2. Classical models for light scattering

In this chapter, two of the main classical models for describing the scattering of light by a particle will be briefly recalled. One is Lorenz-Mie theory (LMT), as well as its extension, Generalized Lorenz-Mie theory (GLMT), and the other is Geometrical optics (GO).

LMT is a rigorous solution to the Maxwell equations for an isotropic, homogeneous (or stratified) sphere illuminated by a plane wave. This is the simplest case, and serves as a reference to validate other numerical, or approximate methods. When the particle is illuminated by a laser beam, the light (both in amplitude and phase) striking the particle is no longer constant, and the incident beam cannot be considered in the same way as the plane wave. In that case, two series of coefficients are introduced to describe the shape of the beam, thereby generalising LMT to make the aforementioned GLMT. This case is especially important in the study of radiation pressure forces, since for a plane wave, the force exerted on the particle depends only on the power of the wave, with the torque always being zero because of the symmetry of the problem. Contrary to that, when a particle is illuminated by a laser beam, the radiation force and torque imparted by the light onto the particle depend not only on the power of the beam, but also the position of the particle within the beam.

When the particle is not spherical, both LMT and GLMT can no longer be applied in their original form. Some work has been done to extend GLMT to non-spherical particles, such as spheroids and infinite cylinders, but the calculable size for these non-spherical particles is still very limited (usually up to some tens of wavelengths). To interpret some of the results in Part A, a numerical method, MLFMA, was applied, with its precision having been validated by GLMT through comparisons with the case of sphere. Even though MLFMA permits the calculation of the light scattering, as well as the optical forces and torques for non-spherical particles of a volume equivalent to a sphere of radius more than a hundred wavelengths, the computation is very time consuming (around one or two days on a very powerful supercomputer).

Naturally, an alternative solution is to use approximate methods. Ashkin and Roosen, amongst others, have applied GO in the calculation of radiation pressure forces for large spherical particles. Jean-Christophe Loudet has extended this method to calculate the radiation pressure forces and torques for a spheroidal particle. GO is simple, and very instructive when it comes to understanding the mechanisms of light scattering. The fundamental principles of GO will be presented in this section, which also serve as the basis of VCRM.

B-2.1. Lorenz-Mie theory

Consider a homogeneous sphere of radius, a , and refractive index, m , illuminated by a plane wave of wavelength, λ , propagating along the z -axis, and polarised in the xz plane, as shown in Figure 59. Its electric field is given by:

$$\vec{E}_i = E_0 e^{-ikz} \hat{e}_x = E_0 e^{-ikr \cos(\theta)} \hat{e}_x \quad \text{B.1}$$

This field can be expanded in the spherical coordinate system as:

$$\vec{E}_i = E_0 \sum_{n=1}^{\infty} c_n^{pw} \left[\vec{m}_{oln}^{(1)} - i \vec{n}_{eln}^{(1)} \right] \quad \text{B.2}$$

$$\vec{H}_i = E_0 \sum_{n=1}^{\infty} c_n^{pw} \left[\vec{m}_{eln}^{(1)} - i \vec{n}_{oln}^{(1)} \right] \quad \text{B.3}$$

where E_0 is the amplitude of the electric field, and the expansion coefficients of plane wave is given by:

$$c_n^{pw} = i^{-n} \frac{2n+1}{n(n+1)} \quad \text{B.4}$$

with $\vec{m}_{oln}^{(1)}$, $\vec{m}_{eln}^{(1)}$, $\vec{n}_{oln}^{(1)}$ and $\vec{n}_{eln}^{(1)}$ are the vector wave functions [80].

The electric and magnetic fields within the particle, as well as their scattered counterparts, can also be expanded as vector wave functions. Thusly, the internal and scattered electric fields are:

$$\vec{E}_s = E_0 \sum_{n=1}^{\infty} c_n^{pw} \left[i a_n \vec{n}_{eln}^{(4)} - b_n \vec{m}_{oln}^{(4)} \right] \quad \text{B.5}$$

$$\vec{E}_e = E_0 \sum_{n=1}^{\infty} c_n^{pw} \left[c_n \vec{m}_{oln}^{(1)} - i d_n \vec{n}_{eln}^{(1)} \right] \quad \text{B.6}$$

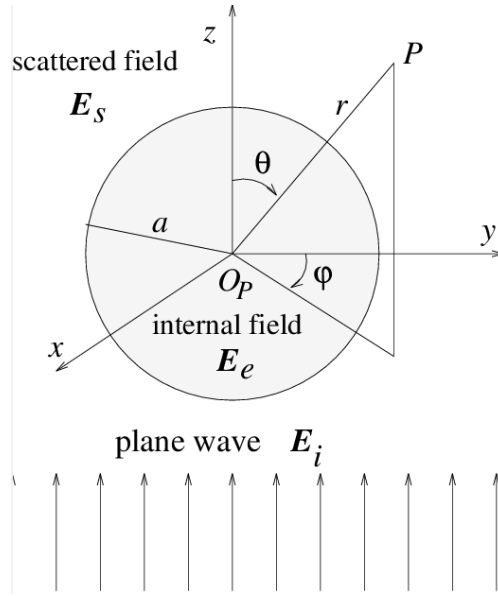


Figure 59: A diagram to aid in explaining the circumstance of the plane wave scattering by a sphere, when considering Lorenz-Mie theory. The sphere is of radius, a , and lies at the origin of an (x, y, z) coordinate system, with the incident field being, \vec{E}_i , the internal field, \vec{E}_e , and the scattered field, \vec{E}_s .

By using the continuous conditions of the tangent components on the surface of the particle:

$$E_{i\phi} + E_{s\phi} = E_{e\phi} \quad \text{B.7}$$

$$E_{i\theta} + E_{s\theta} = E_{e\theta} \quad \text{B.8}$$

$$H_{i\phi} + H_{s\phi} = H_{e\phi} \quad \text{B.9}$$

$$H_{i\theta} + H_{s\theta} = H_{e\theta} \quad \text{B.10}$$

We can obtain the scattering coefficients:

$$a_n = \frac{m\psi_n(\tilde{m}\alpha)\psi'_n(\alpha) - \psi_n(\alpha)\psi'_n(m\alpha)}{m\psi_n(\tilde{m}\alpha)\xi'_n(\alpha) - \xi_n(\alpha)\psi'_n(m\alpha)} \quad \text{B.11}$$

$$b_n = \frac{\psi_n(m\alpha)\psi'_n(\alpha) - m\psi_n(\alpha)\psi'_n(m\alpha)}{\psi_n(m\alpha)\xi'_n(\alpha) - m\xi_n(\alpha)\psi'_n(m\alpha)} \quad \text{B.12}$$

where $\alpha = \frac{2\pi a}{\lambda}$, with ψ_n and ξ_n being Riccati-Bessel functions [76, 80].

In a region far from the particle, the radial component of the scattered field is negligible and the two transverse components are simplified to:

$$E_{s\phi} = -iE_0 \frac{e^{-ikr}}{kr} \sin(\phi) S_1 \quad \text{B.13}$$

$$E_{s\theta} = iE_0 \frac{e^{-ikr}}{kr} \cos(\phi) S_2 \quad \text{B.14}$$

where S_1 and S_2 are distance free amplitudes of the scattered field for perpendicular and parallel polarisation, respectively:

$$S_1 = \sum_{n=1}^{\infty} \frac{2n+1}{n(n+1)} [a_n \pi_n(\theta) + b_n \tau_n(\theta)] \quad \text{B.15}$$

$$S_2 = \sum_{n=1}^{\infty} \frac{2n+1}{n(n+1)} [a_n \tau_n(\theta) + b_n \pi_n(\theta)] \quad \text{B.16}$$

where $\pi_n(\theta)$ and $\tau_n(\theta)$ are two angular functions defined by the Legendre function [80]. Equations B.11 to B.14 then hold all the necessary component for the calculation of the scattered field.

B-2.2. Generalized Lorenz-Mie theory

In the case of shaped beam, the amplitude and the phase of the incident wave is not constant, therefore B.1 is replaced by:

$$\vec{E}_i = E_0 \psi(r, \theta, \phi) e^{-ikr \cos(\theta)} \hat{e}_x \quad \text{B.17}$$

where $\psi(r, \theta, \phi)$ is a complex function describing the variation of the amplitude and phase of the beam at any given point. This field can also be expanded as the more general vector wave functions, $\vec{m}_{mn}^{(1)}$ and $\vec{n}_{mn}^{(1)}$, with two series, $g_{n, TM}^m$ and $g_{n, TE}^m$, called the beam shape coefficients [59]. The scattered fields in a region far from the particle can now be written:

$$E_{s\phi} = -iE_0 \frac{e^{-ikr}}{kr} e^{im\phi} S_1 \quad \text{B.18}$$

$$E_{s\theta} = iE_0 \frac{e^{-ikr}}{kr} e^{im\phi} S_2 \quad \text{B.19}$$

with,

$$S_1 = \sum_{n=1}^{\infty} \sum_{m=-n}^n C_n [ma_n g_{n,TM}^m \pi_n^{|m|}(\theta) + ib_n g_{n,TE}^m \tau_n^{|m|}(\theta)] \quad \text{B.20}$$

$$S_2 = \sum_{n=1}^{\infty} \sum_{m=-n}^n C_n [a_n g_{n,TM}^m \tau_n^{|m|}(\theta) + imb_n g_{n,TE}^m \pi_n^{|m|}(\theta)] \quad \text{B.21}$$

The scattering coefficients depend only on the properties of the particle, namely its size and refractive index, so Equations B.11 and B.12 still apply.

Knowing the scattered field, one can calculate all the required scattering quantities, such as intensity, as well as the radiation force and torque. The three components of the radiation cross-section are given as a function of the beam shape coefficients and the scattering coefficients as follows:

$$\begin{aligned} C_{pr,z} = \frac{\lambda^2}{\pi} \sum_{n=1}^{\infty} \text{Re} \left\{ \frac{1}{n+1} (A_n g_{n,TM}^0 g_{n+1,TM}^{0*} + B_n g_{n,TE}^0 g_{n+1,TE}^{0*}) \right. \\ + \sum_{m=1}^n \left[\frac{1}{(n+1)^2} \frac{(n+m+1)!}{(n-m)!} (A_n g_{n,TM}^m g_{n+1,TM}^{m*} \right. \\ + A_n g_{n,TM}^{-m} g_{n+1,TM}^{-m*} + B_n g_{n,TE}^m g_{n+1,TE}^{m*} \\ + B_n g_{n,TE}^{-m} g_{n+1,TE}^{-m*}) \\ \left. + m \frac{2n+1}{n^2(n+1)^2} \frac{(n+m)!}{(n-m)!} C_n (g_{n,TM}^m g_{n,TE}^{m*} \right. \\ \left. - g_{n,TM}^{-m} g_{n,TE}^{-m*}) \right] \left. \right\} \quad \text{B.22} \end{aligned}$$

$$C_{pr,x} = \text{Re}(C) \quad \text{B.23}$$

$$C_{pr,y} = \text{Im}(C) \quad \text{B.24}$$

where,

$$\begin{aligned}
 C = \frac{\lambda^2}{2\pi} \sum_{n=1}^{\infty} \left\{ & -\frac{(2n+2)!}{(n+1)^2} F_n^{n+1} \right. \\
 & + \sum_{m=1}^n \frac{(n+m)!}{(n-m)!} \frac{1}{(n+1)^2} \left[F_n^{m+1} - \frac{n+m+1}{n-m+1} F_n^m \right. \\
 & + \frac{2n+1}{n^2} (C_n g_{n,TM}^{m-1} g_{n,TE}^{m*} - C_n g_{n,TM}^{-m} g_{n+1,TE}^{-m+1*} \\
 & \left. \left. + C_n^* g_{n,TE}^{m-1*} g_{n,TM}^{m*} - C_n^* g_{n,TE}^{-m} g_{n,TM}^{-m+1*}) \right] \right\} \quad \text{B.25}
 \end{aligned}$$

and

$$\begin{aligned}
 F_n^m = & A_n g_{n,TM}^{m-1} g_{n+1,TM}^{m*} + B_n g_{n,TE}^{m-1} g_{n+1,TE}^{m*} + A_n^* g_{n+1,TM}^{-m} g_{n,TM}^{-m+1*} \\
 & + B_n^* g_{n+1,TE}^{-m} g_{n,TE}^{-m+1*} \quad \text{B.26}
 \end{aligned}$$

with

$$A_n = a_n + a_{n+1}^* - 2a_n a_{n+1}^* \quad \text{B.27}$$

$$B_n = b_n + b_{n+1}^* - 2b_n b_{n+1}^* \quad \text{B.28}$$

$$C_n = -i(a_n + b_{n+1}^* - 2a_n b_{n+1}^*) \quad \text{B.29}$$

All of these calculations have been integrated in the software, ABSphere, developed by Prof. Kuan Fang Ren [28].

B-2.3. Geometrical Optics

GO is a very simple and useful tool to deal with the interaction of light with particles of arbitrary shape, and of size much larger than the wavelength. In GO, a wave of light is modelled as bundles of rays which propagate rectilinearly in a homogenous medium. These rays possess

four properties, namely amplitude, phase, direction and polarisation. Each of these is modified independently each time a ray interacts with the surface of the particle.

GO is an approximate method, and as such, it fails to predict the scattering pattern in certain circumstances. For example, the intensity of scattered light tends to infinity at the rainbow angles. The diffraction, which is responsible for about half of the scattered energy, is also inherently not taken into account. For large particles, it is confined to a narrow angle in the forward direction [76].

B-2.3.1. Fundamentals

Let us first consider the reflection and refraction of a ray on a plane surface. To be able to trace the trajectory of the ray, the direction it travels after an interaction with a boundary must be known, for both the reflected and transmitted case. When the boundary is an interface between two different media, the directions of the ray are related by the Snell-Descartes laws:

$$n_1 \sin(\alpha) = n_2 \sin(\beta) \quad \text{B.30}$$

where n_1 and n_2 are the refractive indices of media 1 and 2 respectively. The directions of the rays are described by the incident angle α , and the refracted angle β , which are defined as the angle between the corresponding rays and the normal to the interface. The reflected ray has the same angle with the normal as that of the incident ray, but unlike the incident ray, its component normal to the interface is reversed.

To determine the amplitudes of the reflected and refracted rays, the Fresnel coefficients must be calculated. The necessary Fresnel coefficients are given below:

$$r_1 = \frac{n_1 \cos(\alpha) - n_2 \cos(\beta)}{n_1 \cos(\alpha) + n_2 \cos(\beta)} \quad \text{B.31}$$

$$r_2 = \frac{n_2 \cos(\alpha) - n_1 \cos(\beta)}{n_2 \cos(\alpha) + n_1 \cos(\beta)} \quad \text{B.32}$$

Where the subscript of r_χ , χ , may take the value of 1 or 2, representing the perpendicular and parallel polarisations to the plane of incidence, respectively. These coefficients dictate the reflectance, R , and transmissivity, T , of the interaction, where:

$$R = |r_\chi|^2 \quad \text{B.33}$$

and

$$T = 1 - R \quad \text{B.34}$$

It is worthwhile to point out that Equations B.31 and B.32 also affect the phase of a ray at the point of reflection. When the media are non-absorbing (meaning that n_1 and n_2 are real), the Fresnel coefficients may be negative, which means that the reflected ray has the opposite phase to that of the incident ray. If total reflection occurs, the Fresnel coefficients become complex, and the argument of this complex number is counted as the phase shift of the reflected ray with respect to the incident ray.

B-2.3.2. Scattering by a sphere

A typical and useful example in the application of GO in the scattering of light by a particle, is that of a homogenous sphere being illuminated by a plane wave, which is the subject of this subsection.

Let us now consider a ray impinging on the surface of a sphere of radius, a , and refractive index, n , with an incident angle of α , as shown in Figure 60. The reflected ray, of order $p = 0$, makes the same angle with the normal of the surface as the incident ray. The refracted ray propagates within the particle until its next interaction with the particle surface. Once this occurs, the refracted ray exits the particle as part of the $p = 1$ order. The angle of this emergent ray with respect to the normal of the particle surface is also equal to the angle of incidence, α . The internally reflected ray, however, continues to propagate and interact with particle surface. It should be noted that all emergent rays make the same angle with normal of the particle surface as did the original ray they came from, namely the angle, α .

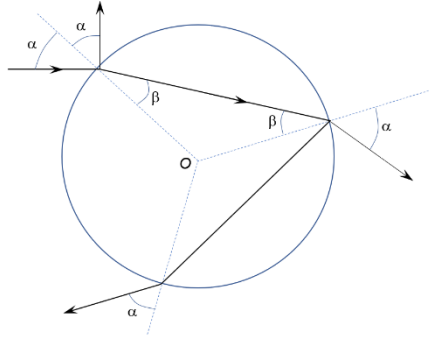


Figure 60: A depiction of a ray striking the surface of a particle of radius, a , and refractive index, n , with an incident angle of α . The angle after refraction is β , whereas the angle for reflection remains the same as the angle of incidence, α .

The amplitude of each emergent ray can be calculated using the Fresnel coefficients. Since all emergent rays, except those that are initially reflected (for $p = 0$), experience two transmissions and $p - 1$ internal reflections, with the Fresnel coefficient having an opposite sign for those reflection, the ratio of the emergent ray to that of the incident ray is given by:

$$\varepsilon_{\chi} = \begin{cases} r_{\chi} & \text{for } p = 0 \\ (1 - r_{\chi}^2)(-r_{\chi})^{p-1} & \text{for } p = 1, 2, 3 \dots \end{cases} \quad \text{B.35}$$

The amplitude of the emergent rays also depends on the divergence, or convergence, of the wave on the surface of the particle. Thanks to the symmetry of the problem, this influence can be described by a so-call divergence factor, derived analytically by the balance of energy.

Consider a bundle of rays from a plane wave impinging on a surface element of the particle, described as $dA = a^2 \cos(\alpha) d\alpha d\phi$. After an interaction with the particle, this bundle of rays is spread onto a surface element, $dA' = r^2 \sin(\theta) d\theta d\phi$. Here, r is the distance of this surface element from the particle centre, with θ and ϕ being the conventional angle coordinates in a spherical coordinate system. If the intensities of the incident and emergent rays with polarisation χ are then noted as, $I_{\chi,0}$ and I_{χ} , respectively, then the energy flux of the bundle of incident rays is:

$$dW = I_{\chi,0} a^2 \sin(\alpha) \cos(\alpha) d\alpha d\phi \quad \text{B.36}$$

and that of the emergent rays is:

$$dW' = I_{\chi} r^2 \sin(\theta) d\theta d\phi = \varepsilon_{\chi}^2 dW \quad \text{B.37}$$

Since the term B.36 is attenuated by successive interactions with the particle, the fractions of energy that are then carried through are calculated directly using the factor, ε_χ , in Equation B.35. This results in the following expression for the intensity of an emergent ray:

$$I_\chi = \frac{\varepsilon_\chi^2 I_{\chi,0} a^2 \sin(\alpha) \cos(\alpha) d\alpha d\phi}{r^2 \sin(\theta) d\theta d\phi} = \frac{a^2}{r^2} I_{\chi,0} \varepsilon_\chi^2 D \quad \text{B.38}$$

where D is the divergence factor, which accounts for the influence that the shape of the scattering particle has on the angular dispersion of the light, and can be given by:

$$D = \frac{\sin(\alpha) \cos(\alpha)}{\sin(\theta) \left| \frac{d\theta}{d\alpha} \right|} \quad \text{B.39}$$

In order to obtain $\left| \frac{d\theta}{d\alpha} \right|$, we must first define the total deviation of the escaping ray with respect to its incident direction. This can be analytically derived for the spherical case [76]:

$$\theta'_p = 2p\beta - 2\alpha + \pi(1 - p) \quad \text{B.40}$$

The total angle deviation can then be related to the scattering angle of the ray, θ_p , by:

$$\theta'_p = 2\pi k_p + q_p \theta_p \quad \text{B.41}$$

where k_p is an integer, and q_p is ± 1 so that θ_p is between 0 and π .

Once differentiated with respect to α , Equation B.41 enables us to define:

$$d\theta_p = \left| \frac{d\theta'_p}{d\alpha} \right| d\alpha \quad \text{B.42}$$

We can then differentiate B.40 with respect to α also, and using the Snell-Descartes law (Equation B.30) and Equation B.42 we get:

$$\frac{d\theta}{d\alpha} = 2 \left(p \frac{\tan(\beta)}{\tan(\alpha)} - 1 \right) \quad \text{B.43}$$

This completes the expression for the divergence factor in Equation B.39:

$$D = \frac{\sin(2\alpha)}{4\sin(\theta) \left(p \frac{\tan(\beta)}{\tan(\alpha)} - 1 \right)} \quad \text{B.44}$$

There are three factors to consider when counting the phase of the emergent rays [76]. The first is the phase shift due to reflection, $\varphi_{p,refl}$ which is calculated directly, in accordance with the Fresnel coefficients, as was elaborated earlier.

The second factor is the phase due to the optical path. Specifically, this is counted as the difference in optical path between the scattered ray and a reference ray that goes through the centre of the particle as if the particle was not there. The reference ray has the same incident and emergent angle as the incident and emergent rays. The phase due to the optical path can be expressed analytically for the spherical case:

$$\varphi_{p,path} = 2ka \left[\cos(\alpha) - p \frac{n_2}{n_1} \cos(\beta) \right] \quad \text{B.45}$$

where k represents the wavenumber of the medium outside of the particle.

The last factor is the phase change due to foci. After a focal line is passed, the phase advances by $\frac{\pi}{2}$. Once again, there is an analytical solution to this problem:

$$\varphi_{p,FL} = \frac{\pi}{2} \left(p - 2k_p + \frac{1}{2}s - \frac{1}{2}q_p \right) \quad \text{B.46}$$

The k_p and q_p are the same as in Equation B.41, and s , is $+1$ or -1 , depending on the sign of $\frac{d\theta_p'}{d\alpha}$.

Finally, by combining the phase shift and amplitude evolution, the complex amplitude of all emergent rays can be calculated. This can be written as:

$$\tilde{S}_p = S_p e^{i\sigma_p} \quad \text{B.47}$$

where σ is the total phase of the ray:

$$\sigma_p = \varphi_{p,refl} + \varphi_{p,path} + \varphi_{p,FL} \quad \text{B.48}$$

And S_p is the distance free amplitude, given by:

$$S_p = \frac{a}{r} \sqrt{D} \varepsilon_\chi \quad \text{B.49}$$

The final intensity at a given angle is then the summation of the complex amplitudes of all the rays arriving in that angle, and multiplying that value by its complex conjugate.

B-3. Vectorial Complex Ray Model

While GO is a very useful approximation, it is a technique rarely used in any kind of quantitative study of light scattering from non-spherical or non-circular cylindrical particles. This is due to a few difficulties that are encountered as soon as one tries to go beyond the spherical or circular case, and starts modelling more complex shapes.

One of these is the tracing of rays, which is technically possible for any shape, however, it becomes more difficult in three-dimensions. This problem can be overcome by using vectors, which simplifies the processes considerably. In fact, if we multiply the Snell-Descartes law from Equation B.30, by the wave number, $k_0 = \frac{2\pi}{\lambda_0}$, it is found that $k_0 n_1 \sin(\alpha) = k_1 \sin(\alpha)$, and $k_0 n_2 \sin(\alpha) = k_2 \sin(\alpha)$, meaning that the tangential component of the incident wave vector on the interface, is the same as that of the refracted, or reflected wave, after the interaction. Therefore, the Snell-Descartes law can be written in vector form as:

$$k_{\tau i} = k_{\tau r} = k_{\tau l} \quad \text{B.50}$$

where the indices, i , r and l signify the wave vector of the incident, refracted and reflected rays, respectively, with the subscript, τ , indicating that these are tangential components.

The main difficulty in dealing with the light scattering of a non-spherical particle using GO is to evaluate the divergence and convergence of the wave on the surface of the particle. One of the possible methods is to calculate the direction of each individual ray, then using numerical techniques, evaluate the divergence or convergence of the wave that these rays represent. This technique, however, is not only very tedious, but also problematic for the calculation of the scattered intensity in the direction of incidence [81].

Furthermore, the problem of divergence and convergence is also related to the counting of the phase shift due to the focal lines, or focal points, that may occur during propagation. In fact, when a wave passes a focal line, the phase advances by $\pi/2$, and when a wave passes a focal point (two perpendicular focal lines crossing at the same point) the phase advances by π . This phase shift has been discussed by van de Hulst in [76], and Hecht in [82]. In the case of scattering by a homogeneous sphere, it can be calculated analytically, as discussed in Section B-2.3.2.

In order to extend the GO model, and deal with the issues above, the Vectorial Complex Ray Model (VCRM) has been developed by Ren et al. [2, 3]. As the name would suggest, VCRM utilises vectors to deal with the ray tracing, and also makes progress in tackling the problem of beam divergence, by introducing the property of wavefront curvature, attached to each ray. The influence upon the wavefront by an arbitrary curved smooth surface can then be calculated using this technique, so the phase change resulting from passing a focal point can be assessed.

The complex amplitudes of all rays arriving at the same angle can then be added to obtain the total intensity.

Since the wavefront curvature is an intrinsic property of the rays in the model, VCRM can naturally deal with the scattering of a Gaussian beam, or a beam of any shape, by a complexly shaped particle, such as ellipsoids, which are the subject of this thesis, and are discussed in detail in the following subsections.

B-3.1. General principles

In this section, we will discuss the methodology of VCRM, and then apply it to the case where light is scattered in the symmetrical plane of an ellipsoid. However, we will be considering the curvature of the particle, both parallel and perpendicular to that plane.

Each complex ray of light in this model represents a bundle of paraxial rays that form an approximation of an isophase wavefront, which is described using a number of characteristics, namely direction of propagation, phase, amplitude, polarisation and the wavefront curvatures, both perpendicular and parallel to the interaction plane. In turn, the complex rays approximate the overall electromagnetic field. From here on, when the term “ray” is used, it refers to the complex rays of VCRM.

The direction of each ray is expressed by its wave vector, \vec{k} , which is a product of the wavenumber and the directional unit vector. In a medium with refractive index, n , it is given by:

$$\vec{k} = k\hat{k} = \frac{2\pi n}{\lambda_0}\hat{k} \quad \text{B.51}$$

where λ_0 is the wavelength of the light in a vacuum.

The Snell-Descartes law in Equation B.30 can be written in vector form as:

$$\vec{k}_i \cdot \hat{\mathbf{t}} = \vec{k}_r \cdot \hat{\mathbf{t}} = \vec{k}_l \cdot \hat{\mathbf{t}} \quad \text{B.52}$$

where $\hat{\mathbf{t}}$ is the directional unit vector of the tangent to the surface at that point, \vec{k}_i , \vec{k}_r and \vec{k}_l are the wave vectors of the incident, refracted and reflected rays of the interaction, respectively.

Thusly, we can work out the magnitude of the normal component of the post-interaction ray:

$$|\vec{k}_r \cdot \hat{\mathbf{n}}| = \sqrt{|\vec{k}_r|^2 - |\vec{k}_i \cdot \hat{\mathbf{t}}|^2} \quad \text{B.53}$$

where $\hat{\mathbf{n}}$ is the unite vector that is normal to the surface of the scatterer, and the formula applies to the reflected ray by substituting the subscript r for l . We also have the relation between the wave vector magnitudes:

$$|\vec{k}_i| = \frac{n_i}{n_r} |\vec{k}_r| \quad \text{B.54}$$

$$|\vec{k}_i| = |\vec{k}_l| \quad \text{B.55}$$

Here, n_i and n_r are the refractive indices within the media of the incident and refracted rays of the interaction, respectively.

So, provided that the normal to the surface is known for a given point, the directions of all rays can be obtained indefinitely.

In VCRM, the wavefront is calculated using the wavefront equations [2, 3, 83]. Referring to Figure 61, if we suppose that a wave with some wavefront curvature, described by the curvature matrix \mathbf{Q}_i , strikes a smooth dioptric surface, the curvature of which is described by the matrix \mathbf{C} , then it is deduced that the curvature matrix of the wavefront after the interaction, \mathbf{Q}_r or \mathbf{Q}_l , can be expressed by the wavefront matrix equation:

$$(\vec{k}_r - \vec{k}_i) \cdot \hat{n}C = |\vec{k}_r| \boldsymbol{\theta}_r^T Q_r \boldsymbol{\theta}_r - |\vec{k}_i| \boldsymbol{\theta}_i^T Q_i \boldsymbol{\theta}_i \quad \text{B.56}$$

The subscript r can be replaced by l to arrive at the analogous equation for reflection. $\boldsymbol{\theta}$ is the projection matrix between the base unitary vectors of the coordinate systems of the wavefront surface, (\hat{t}_1, \hat{t}_2) , and the scattering surface, (\hat{s}_1, \hat{s}_2) . It can be evaluated by:

$$\boldsymbol{\theta} = \begin{pmatrix} \hat{t}_1 \cdot \hat{s}_1 & \hat{t}_1 \cdot \hat{s}_2 \\ \hat{t}_2 \cdot \hat{s}_1 & \hat{t}_2 \cdot \hat{s}_2 \end{pmatrix} \quad \text{B.57}$$

$\boldsymbol{\theta}^T$ is simply the transpose of $\boldsymbol{\theta}$.

In this case, where the interaction plane is the symmetrical plane of the ellipsoid, the rays are always in a plane containing one of the principal curvatures, so the curvature matrices, C and Q (Q representing the initial, reflected and refracted wavefront principal curvatures, in a general way), are diagonal, and can be written as:

$$C = \begin{pmatrix} \frac{1}{\rho_1} & 0 \\ 0 & \frac{1}{\rho_2} \end{pmatrix} \quad \text{B.58}$$

$$Q = \begin{pmatrix} \frac{1}{R_1} & 0 \\ 0 & \frac{1}{R_2} \end{pmatrix} \quad \text{B.59}$$

where ρ_1 and ρ_2 are the principal curvature radii of the dioptric surface, R_1 and R_2 are the principal curvature radii of the wavefront of the ray (before or after the interaction), and once again, the subscripts 1 and 2 respectively signify the perpendicular and parallel directions of the curvatures relative to the interaction plane.

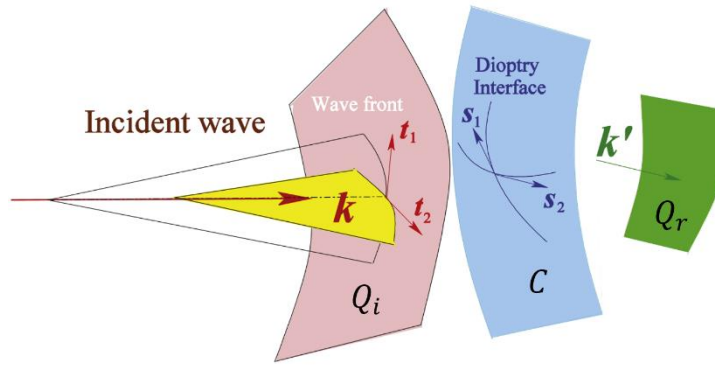


Figure 61: Schematic of the interaction between a wavefront and curved smooth surface.

The following subsections will go into detail about how to calculate the scattering of both, plane waves, and Gaussian beams, in the symmetrical plane of an ellipsoid.

B-3.1.1. Ray tracing

Consider a coordinate system (x, y, z) , the origin of which is the centre of an ellipsoidal particle, with its semi-major axis, c , along the z -axis, and semi-minor axes, a and b , lying along the x -axis and y -axis respectively, as shown in Figure 62. The equation describing the ellipsoid is:

$$\frac{z^2}{c^2} + \frac{y^2}{b^2} + \frac{x^2}{a^2} = 1 \quad \text{B.60}$$

Since only the scattering in the symmetric plane is considered, $y = 0$, and the rays of light are constrained to the xz plane, which they will not leave regardless of any scattering event. Both the wave fronts perpendicular and parallel to the symmetrical plane will change each time the ray interacts with the particle surface.

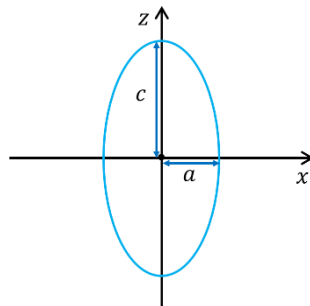


Figure 62: A sketch representing the coordinate system and the dimensions of the kind of ellipsoid being referred to in the text, with semi-minor axes along x and y (coming out of the page), namely a and b (coming out of the page), respectively, with c being the semi-major axis along z .

The particle being homogeneous (with a constant refractive index) means that each ray propagates rectilinearly between any two successive interaction points, and as such, can be described by the equation of a line:

$$x = mz + d \quad \text{B.61}$$

where m is the slope, and d is the x -axis intercept. To obtain the coordinates of a ray crossing the boundary of the ellipse, Equation B.61 is substituted into Equation B.60, whereby the z coordinates can be solved for:

$$z = \frac{-dmc^2 \pm ca\sqrt{a^2 + m^2c^2 - d^2}}{a^2 + m^2c^2} \quad \text{B.62}$$

after which the x coordinates can easily be found with Equation B.61. Then, to define the region of illumination for a plane wave, the discriminant has to be set to zero, and then the two roots of d must be found. These two roots indicate the extrema x -axis intercepts, d , of rays with slope, m , impinging on the particle:

$$d = \pm\sqrt{a^2 + m^2c^2} \quad \text{B.63}$$

This cannot be done analytically for shaped beams, and instead has to be performed numerically, which will be elaborated later.

Then, for a given set of interaction coordinates, the normal of the ellipsoid, which points outward from the particle, is calculated by:

$$\hat{\mathbf{n}} = \left(\frac{c^2x}{\sqrt{(a^2z)^2 + (c^2x)^2}}, 0, \frac{a^2z}{\sqrt{(a^2z)^2 + (c^2x)^2}} \right) \quad \text{B.64}$$

with the tangent at that point as:

$$\hat{\mathbf{t}} = \hat{\mathbf{n}} \times \hat{\mathbf{y}} \quad \text{B.65}$$

where $\hat{\mathbf{y}}$ is the unit vector parallel to the y -axis. It should be noted that for the first interactions, while the rays are still outside of the particle, the normal to the surface, $\hat{\mathbf{n}}$, is used in the opposite direction to that of the rest of the interactions.

So, using Equations B.51 to B.55, as well as those within this subsection, and knowing the initial direction of each ray, all ray tracing can be performed in VCRM for any size and aspect ratio ellipsoid.

B-3.1.2. Wavefront and particle surface curvatures

To know what the wavefront curvature of each ray is after an interaction, we must consider the curvature of the particle at the point of interaction. For the special case, where the interaction plane is a symmetrical plane of an ellipsoid, the principal curvature radii can be calculated as follows [2, 3, 84]:

$$\rho_1 = b^2 \left(\frac{z^2}{c^4} + \frac{x^2}{a^4} \right)^{\frac{1}{2}} \quad \text{B.66}$$

$$\rho_2 = a^2 c^2 \left(\frac{z^2}{c^4} + \frac{x^2}{a^4} \right)^{\frac{3}{2}} \quad \text{B.67}$$

Equations B.66 and B.67, combined with the knowledge of the initial wavefront curvature of each ray, enables the use of Equation B.56 to find the post-interaction wavefront curvatures. Due to the symmetry of the situation, Equation B.56 can be reduced to the following two scalar equations, for perpendicular and parallel wavefront curvatures, with respect to the interaction plane:

$$\frac{|\vec{k}_r|}{R_{1,r}} = \frac{|\vec{k}_i|}{R_{1,i}} + \frac{\vec{k}_r \cdot \hat{n} - \vec{k}_i \cdot \hat{n}}{\rho_1} \quad \text{B.68}$$

$$\frac{(\vec{k}_r \cdot \hat{n})^2}{|\vec{k}_r| R_{2,r}} = \frac{(\vec{k}_i \cdot \hat{n})^2}{|\vec{k}_i| R_{2,i}} + \frac{\vec{k}_r \cdot \hat{n} - \vec{k}_i \cdot \hat{n}}{\rho_2} \quad \text{B.69}$$

Here, the same applies to both, the refracted and reflected wavefronts, the difference being that the subscript r should be replaced with l .

Whilst the ray is propagating freely through a medium, from one point to another, the wavefront curvature radii between two points can be related by:

$$R_{p+1,i} = R_{p,r/l} - r \quad \text{B.70}$$

where $R_{p,r/l}$ is the wavefront curvature radius at the point, p , and $R_{p+1,i}$ is the curvature radius of the same wavefront at the next point of interaction, $p + 1$, with r being the distance between the two points. This style adheres to common sign conventions, where the wavefront radius is positive before it converges toward the focus, and is then negative once it starts to diverge away from the it.

B-3.1.3. Divergence factor

In VCRM, the behaviour of divergence, or convergence, of a wave is described by the divergence factor, D . It can be evaluated directly, using the wave front curvature radii, in accordance to the following equation [2, 3]:

$$\mathfrak{D} = \left| \frac{R_{10,r/l}R_{20,r/l}}{R_{11,i}R_{21,i}} \cdot \frac{R_{11,r/l}R_{21,r/l}}{R_{12,i}R_{22,i}} \dots \frac{R_{1p,r/l}R_{2p,r/l}}{(R_{1p,r/l} - r)(R_{2p,r/l} - r)} \right| \quad \text{B.71}$$

Here, r is the distance between the location of the last interaction and the observation point. In the far field, r tends to infinity, so the denominator is omitted from the calculation, leaving:

$$D = \mathfrak{D}r^2 = \left| \frac{R_{10,r/l}R_{20,r/l}}{R_{11,i}R_{21,i}} \cdot \frac{R_{11,r/l}R_{21,r/l}}{R_{12,i}R_{22,i}} \dots R_{1p,r/l}R_{2p,r/l} \right| \quad \text{B.72}$$

So, for the first reflection, when $p = 0$, the divergence factor would be:

$$D = |R_{10,l}R_{20,l}| \quad \text{B.73}$$

The product of the surface curvatures here, generally expressed as, $\frac{1}{R_{1p,r/l}R_{2p,r/l}}$, is the Gaussian curvature of the given wavefront.

B-3.1.4. Fresnel coefficients

As with GO, VCRM takes into account the Fresnel coefficients as a way to determine the attenuation of a ray at each interaction. In vector form, these can be expressed as:

$$r_1 = \frac{|\vec{k}_i \cdot \hat{n}| - |\vec{k}_r \cdot \hat{n}|}{|\vec{k}_i \cdot \hat{n}| + |\vec{k}_r \cdot \hat{n}|} \quad \text{B.74}$$

$$r_2 = \frac{n_r^2 |\vec{k}_i \cdot \hat{n}| - n_i^2 |\vec{k}_r \cdot \hat{n}|}{n_r^2 |\vec{k}_i \cdot \hat{n}| + n_i^2 |\vec{k}_r \cdot \hat{n}|} \quad \text{B.75}$$

$$t_1 = \frac{2|\vec{k}_i \cdot \hat{n}|}{|\vec{k}_i \cdot \hat{n}| + |\vec{k}_r \cdot \hat{n}|} \quad \text{B.76}$$

$$t_2 = \frac{2n_i n_r |\vec{k}_i \cdot \hat{n}|}{n_r^2 |\vec{k}_i \cdot \hat{n}| + n_i^2 |\vec{k}_r \cdot \hat{n}|} \quad \text{B.77}$$

where n_i is the refractive index of the incident medium, and n_r is the refractive index of the refracting medium.

The incident and the refraction angles (or equivalently $\vec{k}_i \cdot \hat{n}$ and $\vec{k}_r \cdot \hat{n}$) change at each interaction of a ray with the particle surface during light scattering by an elliptical particle. The factor defined in Equation B.35 for a spherical particle, must therefore be replaced by the following equation:

$$\varepsilon_\chi = \begin{cases} r_{\chi,0} & \text{for } p = 0 \\ t_{\chi,0} t_{\chi,p} \prod_{i=1}^{p-1} r_{\chi,i} & \text{for } p = 1, 2, 3 \dots \end{cases} \quad \text{B.78}$$

This mean that that, $\varepsilon_\chi = t_{\chi,0} t_{\chi,1}$, for a ray of order, $p = 1$, and $\varepsilon_\chi = t_{\chi,0} t_{\chi,2} r_{\chi,1}$ for a ray that has undergone 1 internal reflection (order $p = 2$), and so on.

B-3.1.5. Phase calculations

The phase in VCRM can be counted as four parts, similar to GO. They are the phase of the incident ray, the phase due to the optical path, the phase due to reflection (taken care of by the Fresnel coefficients, including total reflection), and focal lines. This amounts to:

$$\varphi = \varphi_i + \varphi_p + \varphi_R + \varphi_{FL} \quad \text{B.79}$$

with φ_i being the initial phase, φ_p the phase due to the optical path, φ_R the phase change due to reflection, and finally φ_{FL} is the phase change from focal lines.

The phase of the incident ray is necessary only for a shaped beam, since it is constant for the plane wave case. An example of this will be dealt with in Section B-3.2, where the case for a Gaussian beam will be addressed.

The phase shift from the optical path is calculated with respect to a reference ray, and is made up of two components, one outside the particle, and the other within it. The reference ray is one that arrives at the same angle as the incident ray, passing by the particle centre, then going out in the same direction as the emergent ray, as if there were no particle. This is represented by the dashed line in Figure 63.

The phase shift due to the optical path within the particle can be calculated directly by counting the total distance travelled by the ray within the particle boundaries, namely $d_{part\ tot}$ (BC in Figure 63), where:

$$\varphi_{p,part} = k_{part}d_{part\ tot} \quad \text{B.80}$$

with k_{part} being the wavenumber within the particle. This is then combined with the phase shift from the path of the ray that is travelled outside the particle. The optical path outside of the particle includes two parts, one before arriving at the particle surface (AB in Figure 63), noted as $d_{diff,inc}$, and the other after emerging from the particle (DE in Figure 63), noted as $d_{diff,exit}$. It is worth noting that the phase due to the outside optical path may be, respectively, positive or negative, depending on whether the ray travels a shorter or longer distance outside the particle than the reference ray does to the origin.

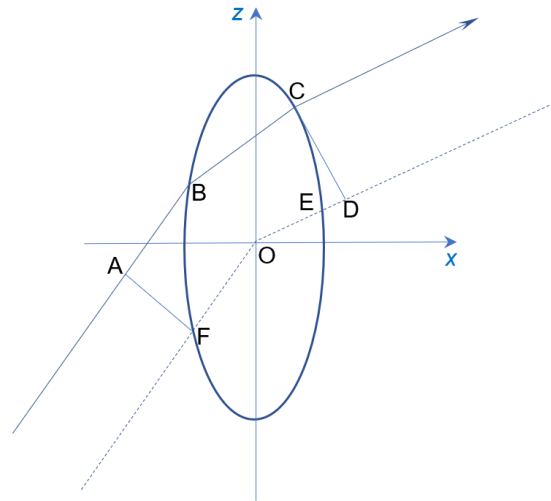


Figure 63: A sketch to aid in the description of the phase change due to the optical path. The dashed line is the reference ray, while the solid line is the ray being scattered.

The total optical path phase can then be expressed as:

$$\varphi_p = k_{out} (d_{ref} - (d_{diff,inc} + d_{diff,exit})) - \varphi_{p,part} \quad \text{B.81}$$

with k_{out} being the wavenumber in the medium outside of the particle, and d_{ref}

This can be taken care of vectorially, using:

$$\varphi_p = -k_{out} (\hat{\mathbf{k}}_0 \cdot \vec{\mathbf{r}}_1 - \hat{\mathbf{k}}_q \cdot \vec{\mathbf{r}}_q) - k_{part} \sum_{i=1}^{q-1} \hat{\mathbf{k}}_i \cdot (\vec{\mathbf{r}}_{i+1} - \vec{\mathbf{r}}_i) \quad \text{B.82}$$

where $\hat{\mathbf{k}}_i$ is the directional unit vector of the ray after interaction point i , with $\vec{\mathbf{r}}_i$ as the position vector at point i . Here, q is the total number of interactions.

As previously stated, the phase shift due to reflection is calculated by the Fresnel coefficients. This is because the reflection coefficients can be positive, negative, or complex (in the case of total reflection, or for an absorbing particle).

If no total reflection occurs, the Fresnel coefficients can only be positive or negative. In this case, there is a phase shift of half a wave [82], meaning that:

$$\varphi_R = \pi \quad \text{B.83}$$

The transmission coefficients are always positive, so there is no phase shift associated with a refractive event.

However, when a ray travels from a medium with a high refractive index, to one with a lower refractive index, $n_i > n_r$, then the condition for total reflection in VCRM may be met if $|\vec{k}_i \cdot \hat{\mathbf{t}}| > |\vec{k}_r|$. This means that if the tangent component of the incident ray is greater than the wavenumber in the second medium, the reflection coefficients become complex. So, Equation B.53 becomes:

$$|\vec{k}_r \cdot \hat{\mathbf{n}}| = i\sqrt{|\vec{k}_i \cdot \hat{\mathbf{t}}|^2 - |\vec{k}_r|^2} \quad \text{B.84}$$

and the reflection coefficients, B.74 and B.75 are changed to:

$$r_1 = \frac{|\vec{k}_i \cdot \hat{\mathbf{n}}| - i\sqrt{|\vec{k}_i \cdot \hat{\mathbf{t}}|^2 - |\vec{k}_r|^2}}{|\vec{k}_i \cdot \hat{\mathbf{n}}| + i\sqrt{|\vec{k}_i \cdot \hat{\mathbf{t}}|^2 - |\vec{k}_r|^2}} \quad \text{B.85}$$

$$r_2 = \frac{n_r^2 |\vec{k}_i \cdot \hat{\mathbf{n}}| - in_i^2 \sqrt{|\vec{k}_i \cdot \hat{\mathbf{t}}|^2 - |\vec{k}_r|^2}}{n_r^2 |\vec{k}_i \cdot \hat{\mathbf{n}}| + in_i^2 \sqrt{|\vec{k}_i \cdot \hat{\mathbf{t}}|^2 - |\vec{k}_r|^2}} \quad \text{B.86}$$

Whilst the amplitude is not attenuated after such an interaction, the phase does change after total reflection. The argument of each of the complex coefficients yields this phase shift, which is applied to the perpendicular and parallel components of the totally reflected ray, respectively:

$$\varphi_{TR,1} = -\tan^{-1} \left(\frac{2|\vec{k}_i \cdot \hat{\mathbf{n}}| \sqrt{|\vec{k}_i \cdot \hat{\mathbf{t}}|^2 - |\vec{k}_r|^2}}{|\vec{k}_i \cdot \hat{\mathbf{n}}|^2 - |\vec{k}_i \cdot \hat{\mathbf{t}}|^2 + |\vec{k}_r|^2} \right) \quad \text{B.87}$$

$$\varphi_{TR,2} = -\tan^{-1} \frac{2 \left(\frac{n_r}{n_i}\right)^2 |\vec{k}_i \cdot \hat{n}| \sqrt{|\vec{k}_i \cdot \hat{t}|^2 - |\vec{k}_r|^2}}{\left(\frac{n_r}{n_i}\right)^4 |\vec{k}_i \cdot \hat{n}|^2 - |\vec{k}_i \cdot \hat{t}|^2 + |\vec{k}_r|^2} \quad \text{B.88}$$

The final phase change is, φ_{FL} , the shift due to the focal lines. Since it was elaborated previously that wavefront curvature is an intrinsic property of the rays in VCRM, the calculation of the phase due to the focal lines amounts to simply counting the sign changes of the wavefront curvatures, which are events that occur as a direct result of passing a focus. If only the perpendicular, or parallel, wavefront curvature changes sign between two interactions, we add $\frac{\pi}{2}$ to the phase. If both change sign, then π is added.

B-3.1.6. Amplitude and intensity

Combining the phase, the divergence factor and the Fresnel coefficients, we can calculate the complex amplitude of each ray. For convenience in describing the calculation of the total field, each ray will have a number, i , from now on. Thus, the complex amplitude of each ray in the far field can be expressed as [2, 3]:

$$S_{\chi,i} = A_{\chi,0,i} e^{i\varphi_i} |\varepsilon_{\chi,i}| \sqrt{\mathcal{D}_i} = \frac{1}{kr} S_{\chi,i} \quad \text{B.89}$$

where $A_{\chi,0,i}$ is the amplitude of the incident ray. $S_{\chi,i}$ is the distance free amplitude, given by:

$$S_{\chi,i} = A_{\chi,0,i} k e^{i\varphi_i} |\varepsilon_{\chi,i}| \sqrt{\mathcal{D}_i} \quad \text{B.90}$$

Knowing the phase and the amplitude of each ray, we can calculate the total complex amplitude of the scattered light at a given angle, by the summation of the complex amplitudes of all rays arriving at that angle:

$$S_{\chi} = \sum_{i=1}^N S_{\chi,i} \quad \text{B.91}$$

where N is the number of rays emerging at the given angle. So, the total intensity at that point is therefore simply the square of its amplitude:

$$i_\chi = |s_\chi|^2 = s_\chi s_\chi^* \tag{B.92}$$

with s_χ^* being a complex conjugate. i_χ is the distance free intensity of the scattered light in the far field, which is the quantity usually presented within a scattering diagram.

However, the summation of Equation B.91 cannot be calculated directly, because the angle with which each emergent ray exits the particle depends on its incident position, its order, the shape of the particle, as well as other factors, which make the angular distribution of the scattered rays irregular, and hence make the summation of the complex amplitudes a not so simple task. This is illustrated in Figure 64, where the variation of the amplitude of emergent rays of order $p = 2$ can be seen. It can clearly be noticed that the same order of rays arrives twice through a given angle range. However, the two amplitudes of the emergent rays at a given angle, for example 142° , are not known. Therefore, the amplitude and phase of each ray at a given angle needs to be determined by an interpolation procedure that includes the local emergent rays.

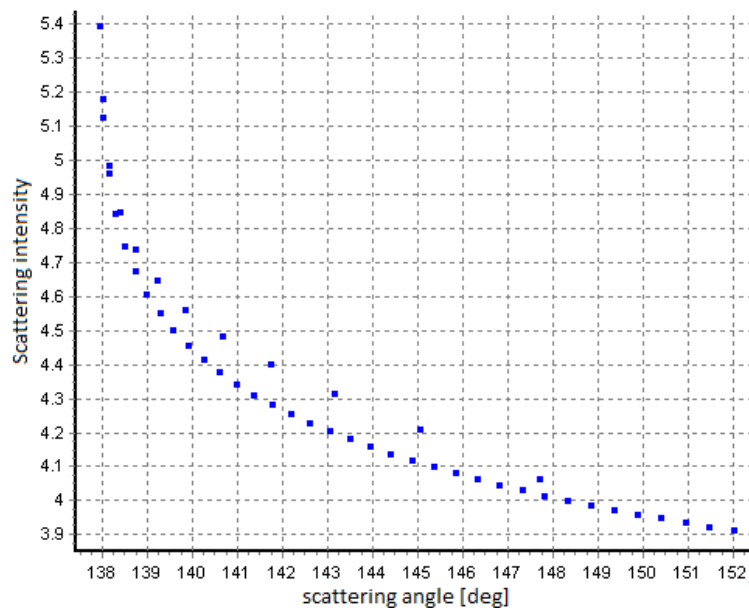


Figure 64: This is a small section of an intensity scattering diagram. It highlights and example of the irregular angular distribution of scattered rays. The rays shown are of order $p = 2$.

B-3.1.7. Interpolation

Usually, interpolation algorithms are used for monotone functions, so the first thing to be done is to separate the emergent rays into groups, so that the variation of the angle in each group

is monotone (either increasing or decreasing, and never both). To accomplish this, we first separate the emergent rays by their orders, p . This means that rays of different orders cannot be used in the same interpolation.

Rays of the same order are then further split into groups based on whether or not there is a returning angle (the angle difference between two successive rays changes sign from one step to the next in a particular order, p). If total reflection is encountered for a particular order, then this also acts as a separator for the groups.

Once the groups of rays are well defined, the amplitudes and phases can be interpolated simultaneously for any angle. Finally, the total complex amplitude can be calculated according to Equation B.91 for all angles necessary for the scattering diagram. In the case of VCRM, the Lagrangian interpolation method is used to calculate the intermediate amplitudes and phases of the rays.

B-3.2. Gaussian beam

One of the important advantages of VCRM is that it can be applied to deal with any shaped beam, provide the latter is not too strongly focused, so that its propagation can be described by rectilinear rays inside the particle.

In this thesis, the interest lies in the radiation pressure forces acting on ellipsoidal particles. So, in this section, the scattering of a Gaussian beam by an ellipsoidal particle will be discussed. Like the plane wave case, only the scattering contained within the symmetrical plane is considered, so the axis of the beam must lie in this plane also.

In VCRM, the only difference between plane wave scattering and beam scattering is that the ray properties (namely amplitude, phase, direction and wave front curvatures) at the incident point are no longer constant. Thusly, the only necessary modification to the model is that these properties need to be determined for each ray at its initial incident point.

B-3.2.1. Description of a Gaussian beam

Consider a circular Gaussian beam of beam waist radius, ω_0 , propagating along the positive w direction in its coordinate system, (u, v, w) . A graphical representation of its intensity can be seen in Figure 65.

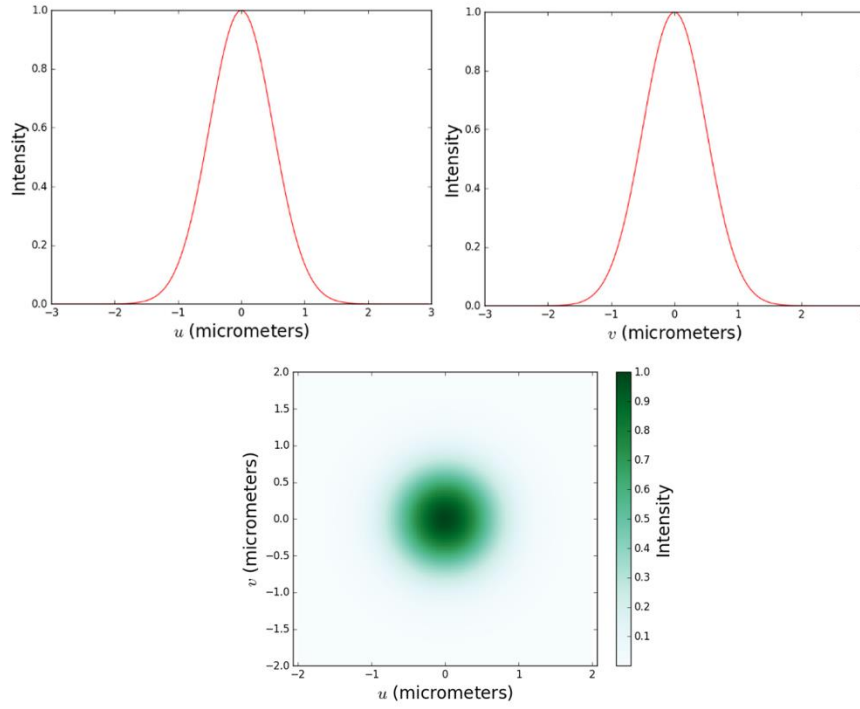


Figure 65: A simple characterisation of a circular Gaussian beam.

The complex amplitude of the Gaussian beam is given by [85]:

$$S_G(u, v, w) = \frac{\omega_0}{\omega_l} \exp\left(-\frac{u^2 + v^2}{\omega_l^2}\right) \exp(i\varphi(u, v, w)) \quad \text{B.93}$$

where

$$\varphi(u, v, w) = -k \left(w + \frac{u^2 + v^2}{2w \left(1 + \left(\frac{l}{w} \right)^2 \right)} \right) + \tan^{-1} \left(\frac{w}{l} \right) \quad \text{B.94}$$

with $\tan^{-1} \left(\frac{w}{l} \right)$ being the Gouy phase, ω_0 the beam waist radius, l the Rayleigh length, and ω_l the local beam radius, where the latter two can be expressed in the following way, respectively:

$$l = \frac{\pi \omega_0^2}{\lambda} \quad \text{B.95}$$

$$\omega_l = \omega_0 \sqrt{1 + \left(\frac{w}{l}\right)^2} \quad \text{B.96}$$

In the case under study, $v = 0$ holds true, because the uw plane of the beam always coincides with the symmetrical plane, xz , of the ellipsoid.

In the plane wave case, the illumination region can be defined analytically, however, this is not the case for a Gaussian beam, because the incident direction changes from point to point. A simple way is to determine if a ray interacts with the particle surface is to calculate the scalar product of the wave vector of the beam and the normal vector of the particle surface at that point. If the result is negative, the ray interacts with the particle, if not it is discarded.

B-3.2.2. Transformation of coordinate systems

To calculate the properties of the incident rays of the Gaussian beam at the interaction point on the particle surface, we need the electric field at that point. However, in the general case, the coordinate system of the beam does not coincide with that of the particle. Hence, a coordinate transformation between the two systems is necessary.

This can be realized by a rotation and a translation. Before the transformation is performed, both coordinate systems are coincident, with u lying along x , v lying along y and w lying along z . The respective translations, (x_0, y_0, z_0) , are made in order to vary the beam centre with respect to that of the particle. As previously discussed, y_0 will always be zero. However, x_0 and z_0 are the coordinates of the beam centre within the particle coordinate system. The complete transformation is then achieved by simply rotating by an angle, θ , about the y axis. The relation between the particle coordinate system and that of the beam is given by:

$$\begin{pmatrix} u \\ v \\ w \end{pmatrix} = A \begin{pmatrix} x - x_0 \\ y \\ z - z_0 \end{pmatrix} \quad \text{B.97}$$

the matrix A , is:

$$A = \begin{pmatrix} \cos(\theta) & 0 & -\sin(\theta) \\ 0 & 1 & 0 \\ \sin(\theta) & 0 & \cos(\theta) \end{pmatrix} \quad \text{B.98}$$

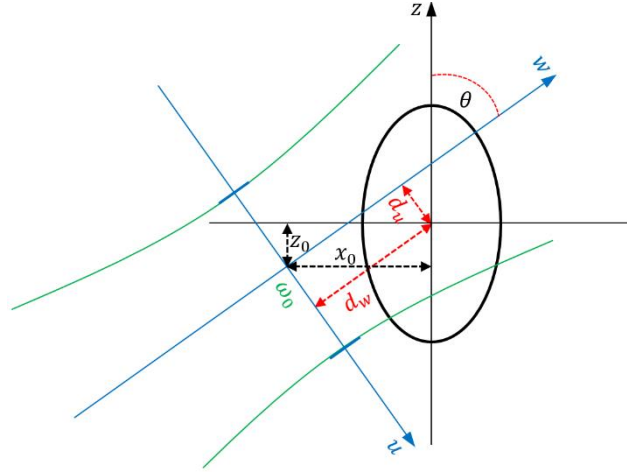


Figure 66: A graphic description of the coordinate system transformation - the ellipsoidal coordinate system being in black, and that of the beam in blue, with the relevant translations, x_0 and z_0 , distances, d_u and d_w as well as the rotation, θ shown accordingly.

Remembering that $y_0 = 0$, and utilising Equation B.97, any point in the particle coordinate system can be obtained within the beam coordinate system using the following expressions:

$$u = (x - x_0) \cos(\theta) - (z - z_0) \sin(\theta) \quad \text{B.99}$$

$$v = 0 \quad \text{B.100}$$

$$w = (x - x_0) \sin(\theta) + (z - z_0) \cos(\theta) \quad \text{B.101}$$

Now all the beam calculations can be managed within its own coordinate system, by transforming each interaction point on the particle surface.

For the purpose of making it easier to match usual experimental conditions with that of the model, two distances may be used to indicate the distance between the beam centre and that of the particle. d_w dictates the perpendicular distance between the beam waist and the particle centre, whilst d_u is the lateral counterpart, this time with respect to the beam propagation axis and the particle centre, as shown in Figure 66. d_u and d_w can be obtained using:

$$d_u = -x_0 \cos(\theta) + z_0 \sin(\theta) \quad \text{B.102}$$

$$d_w = -x_0 \sin(\theta) - z_0 \cos(\theta) \quad \text{B.103}$$

These equations can be solved simultaneously to get the positions, x_0 and z_0 , to correspond to the desired displacements of the beam with respect to the particle centre, d_u and d_w .

B-3.2.3. Propagation direction

In VCRM model, a Gaussian beam is represented by a bundle of rays. Each of these rays is travelling in a direction orthogonal to the local wavefront, which can otherwise be described as the isophase surface. Since the isophase surface propagates in the same direction as the rays, we may obtain that direction by finding the gradient of the phase function (Equation B.94) at the desired point in space (in this case at the surface of the scattering particle). We may then use the transpose of the rotation matrix to find that direction within the coordinate system of the ellipsoid, which we can generally express as:

$$\nabla F(x, y, z) = (F'_x, F'_y, F'_z) = (\varphi'_u, \varphi'_v, \varphi'_w)A \quad \text{B.104}$$

So, in order to obtain the wavevector of the ray, we have:

$$\vec{k} = k \frac{\nabla F(x, y, z)}{\|\nabla F(x, y, z)\|} \quad \text{B.105}$$

where k is the wavenumber.

From Equation B.94, we can find the first order derivatives to be:

$$\varphi'_u = -k \frac{uw}{l^2 + w^2} \quad \text{B.106}$$

$$\varphi'_v = -k \frac{vw}{l^2 + w^2} \quad \text{B.107}$$

$$\varphi'_w = -k - k \frac{(u^2 + v^2)(l^2 - w^2)}{2(l^2 + w^2)^2} + \frac{l}{l^2 + w^2} \quad \text{B.108}$$

B-3.2.4. Wavefront curvature

Since the wavefronts are isophase surfaces, they can be calculated directly from the phase function in Equation B.94. To do this, the method by Goldman [86] is adopted. The principal curvatures, κ_1 and κ_2 are then given by:

$$\kappa_1, \kappa_2 = \kappa_M \pm \sqrt{\kappa_M^2 - \kappa_G} \quad \text{B.109}$$

where κ_M and κ_G are the mean and Gaussian curvatures, respectively. The mean curvature, κ_M , is the average of the principal curvatures, $\kappa_M = \frac{1}{2}(\kappa_1 + \kappa_2)$, whilst the Gaussian curvature is the product of the same, $\kappa_G = \kappa_1\kappa_2$. These can be found by [86]:

$$\kappa_M = \frac{\nabla F \cdot H(F) \cdot \nabla F^T - |\nabla F|^2 \text{Trace}(H)}{2|\nabla F|^3} \quad \text{B.110}$$

$$\kappa_G = \frac{\nabla F \cdot H^*(F) \cdot \nabla F^T}{|\nabla F|^4} \quad \text{B.111}$$

Here, $H(F)$ is the hessian of the function $F(x, y, z)$, and $H^*(F)$ is the cofactor matrix of the hessian. $H(F)$ can be represented as:

$$H(F) = \begin{pmatrix} F''_{xx} & F''_{xy} & F''_{xz} \\ F''_{yx} & F''_{yy} & F''_{yz} \\ F''_{zx} & F''_{zy} & F''_{zz} \end{pmatrix} \quad \text{B.112}$$

where '' stands for a second order derivative. To arrive to Equation B.112 from the beam coordinate system, we use:

$$H(F) = A^T \begin{pmatrix} \varphi''_{uu} & \varphi''_{uv} & \varphi''_{uw} \\ \varphi''_{vu} & \varphi''_{vv} & \varphi''_{vw} \\ \varphi''_{wu} & \varphi''_{wv} & \varphi''_{ww} \end{pmatrix} A \quad \text{B.113}$$

We find the second order derivatives of Equation B.94 to be:

$$\varphi''_{uu} = \varphi''_{vv} = -\frac{kw}{l^2 + w^2} \quad \text{B.114}$$

$$\varphi''_{uv} = \varphi''_{vu} = 0 \quad \text{B.115}$$

$$\varphi''_{uw} = \varphi''_{wu} = -\frac{ku(l^2 - w^2)}{(l^2 + w^2)^2} \quad \text{B.116}$$

$$\varphi''_{vw} = \varphi''_{wv} = -\frac{kv(l^2 - w^2)}{(l^2 + w^2)^2} \quad \text{B.117}$$

$$\varphi''_{ww} = -\frac{kw(u^2 + v^2)(3l^2 - w^2)}{(l^2 + w^2)^3} - \frac{2lw}{(l^2 + w^2)^2} \quad \text{B.118}$$

Therefore, the wave front curvature at each incident point can be calculated using the first and the second derivatives of the phase function, along with the transformation matrix between the beam coordinate system and that of the particle.

B-4. Results and discussion

In accordance with the method of VCRM, described in Section B-3, two programs have been written in Python 2.7.13 to deal with plane wave, as well as Gaussian scattering by spheroidal particles. To address the accuracy and quality of the model, scattering diagrams of the intensity distribution have been calculated for the cases of spheres, as well as both oblate and prolate spheroids. Both, the VCRM plane wave and Gaussian cases are compared alongside rigorous GLMT calculations in order to validate them, at least when dealing with spheres. The particles are all non-absorbing, so their refractive indices are always real. Diffraction is not taken into account in the VCRM model used for these calculations, although for large particles, the effect of diffraction is confined to a very narrow angle range in the forward scattering direction, as will become apparent when comparisons are made with GLMT. Surface waves have also not been taken into account for any of the calculations.

It should be noted that the wavelength for all calculations is that of the commonly utilised Helium-Neon laser, $\lambda_0 = 0.6328\mu\text{m}$, the orders that are considered are from $p = 0$ to $p = 5$, the polarisation is always perpendicular to the interaction plane, and the number of incident rays is $N_{inc} = 5000$, with the number of scattered points being the same, $N_{scattered} = 5000$.

Firstly, some spherical cases are addressed in Section B-4.1, after which scattering diagrams for both oblate and prolate particles at various incidence angles with respect to the direction of light are presented in Section B-4.2.

B-4.1. Scattering diagrams for spheres

Figure 67 shows the scattering of a plane wave by a large sphere ($a = b = c = 100\mu\text{m}$). This is achieved with VCRM and GLMT. The beam waist radius is taken to be $\omega_0 = 1\text{m}$ in the GLMT and VCRM Gaussian beam calculations.

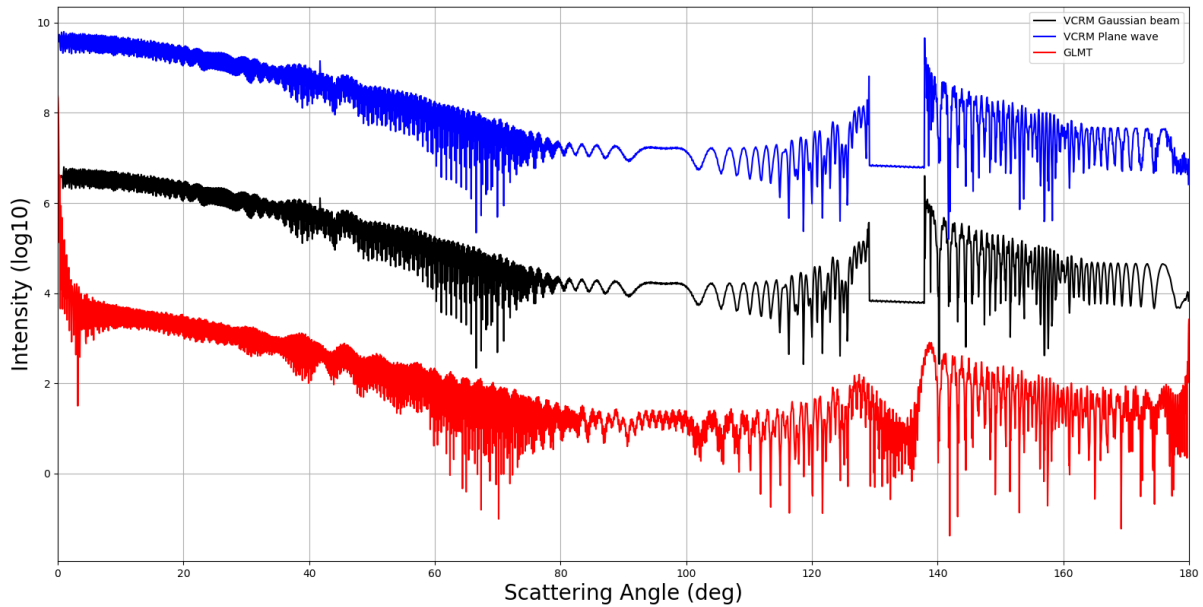


Figure 67: Scattering diagram showing the intensity distribution (in \log_{10}) across the angle range, 0° to 180° , for light scattered by a sphere using a VCRM plane wave (blue), a VCRM Gaussian beam (black), and GLMT (red). Calculation parameters: $a = b = c = 100\mu\text{m}$, $m = 1.333$, $\omega_0 = 1\text{m}$ and $\theta_{inc} = 0^\circ$. Here, the plane wave case (blue) has been offset by 10^3 , and the GLMT calculation (red) has been offset by 10^{-3} , in the interest of clarity.

As can be seen in Figure 67, there is reasonable agreement between the VCRM models and GLMT, although some small differences are discernible, especially in the region of the first and second rainbows (from about $\theta \sim 125^\circ$ to $\theta = 140^\circ$), for which GO approximations fail, since the intensity is calculated as being infinite. Also, as is the case for the rest of the scattering diagrams by spheres, there is a difference due to diffraction for $\theta \lesssim 5^\circ$.

Figure 68 is simply the same sphere as that in Figure 67, but the incident beam makes an angle of $\theta = 20^\circ$ with respect of the z -axis. Theoretically, the rotation of a sphere should not make any difference to the scattering diagram. However, it has been clearly shown that there exists an intrinsic problem in numerical calculations using classical GO [81]. Furthermore, this is a critical step to check the code for scattering by any non-spherical particle. We observe that the scattering diagrams calculated by VCRM are just translated by 20° with respect to on-axis incidence (Figure 67), which shows that the code works well.

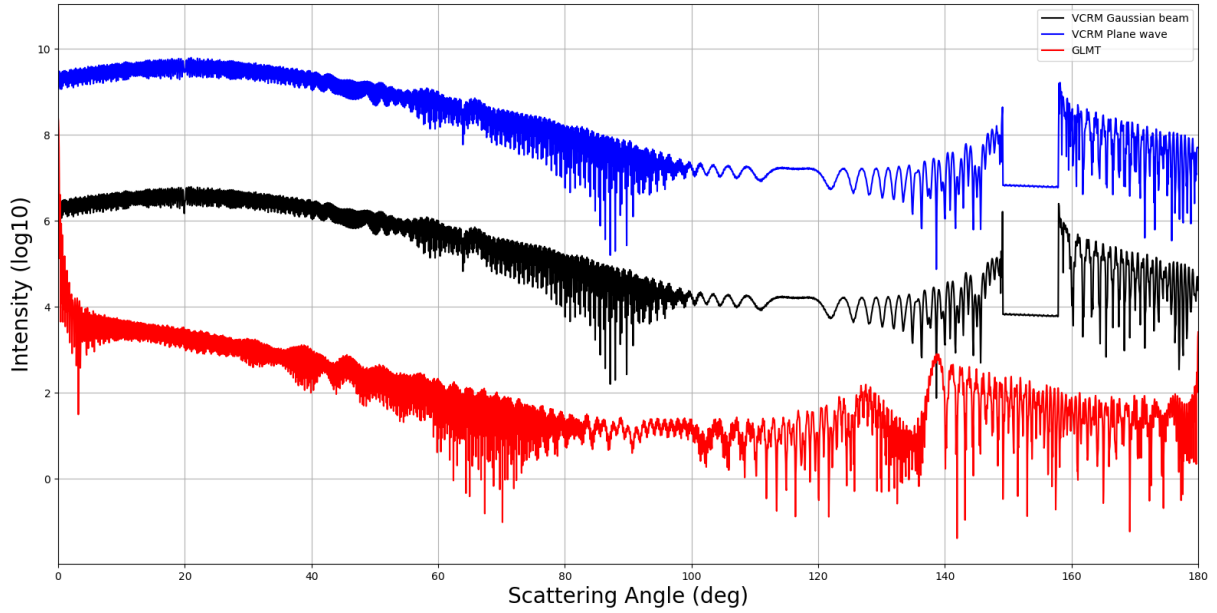


Figure 68: The parameters are the same as in Figure 67, except that $\theta_{inc} = 20^\circ$ for the VCRM plane wave (blue), and the VCRM Gaussian beam (black) cases.

Figure 69 and Figure 70 are scattering diagrams for a sphere with $a = b = c = 50\mu\text{m}$, illuminated by a Gaussian beam with a beam waist radius (for the Gaussian VCRM and GLMT simulations) of $\omega_0 = 50\mu\text{m}$ and $\omega_0 = 10\mu\text{m}$, respectively. While the Gaussian beam waist radius is equal to the particle radius, the scattering diagram is similar to that of a plane wave, but the intensity at the rainbow angles is weaker (see Figure 69). On the other hand, if the beam waist is much smaller than the particle radius (as per Figure 70, with $\omega_0 = 10\mu\text{m}$ and $a = b = c = 50\mu\text{m}$), then the rainbow structures are no longer visible and the profiles of the VCRM Gaussian beam and the GLMT calculations match quite well in Figure 70. In fact, the agreement seems greater than that in Figure 69. This is because the incident intensities of the rays corresponding to the rainbows (the impact point of which is at about $0.86a$ for the first rainbow, and about $0.95a$ for the second) are much lower than those near the beam axis.

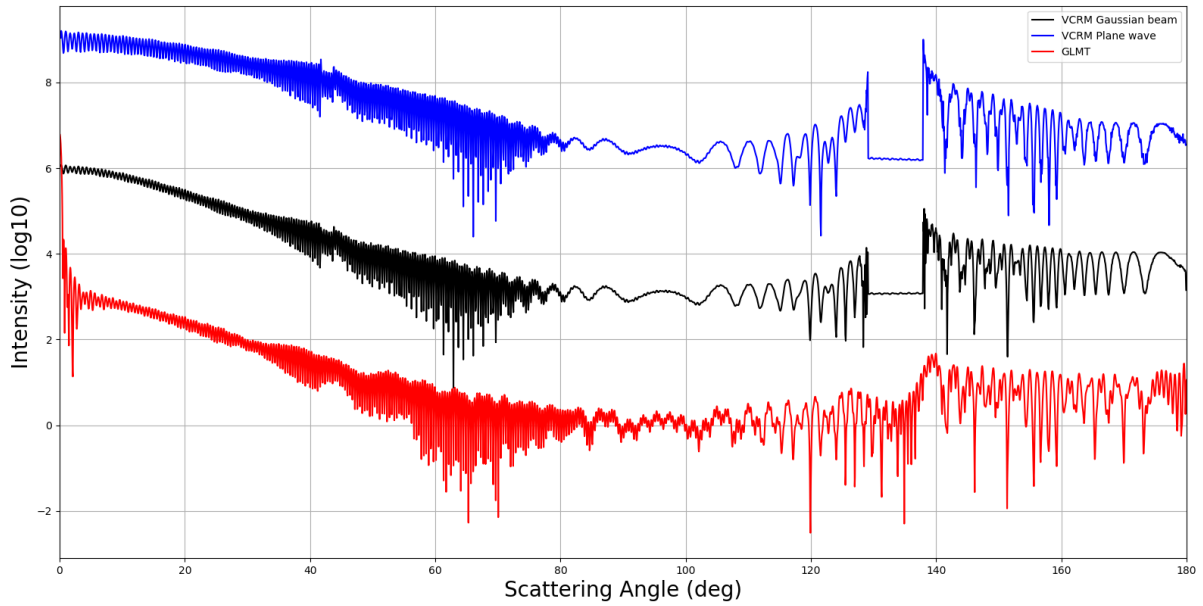


Figure 69: Scattering diagram showing the intensity distribution (in \log_{10}) across the angle range, 0° to 180° , for light scattered by a sphere using a VCRM plane wave (blue), a VCRM Gaussian beam (black), and GLMT (red). Calculation parameters: $a = b = c = 50\mu\text{m}$, $m = 1.333$, $\omega_0 = 50\mu\text{m}$ and $\theta_{inc} = 0^\circ$. Here, the plane wave case (blue) has been offset by 10^3 , and the GLMT calculation (red) has been offset by 10^{-3} , in the interest of clarity.

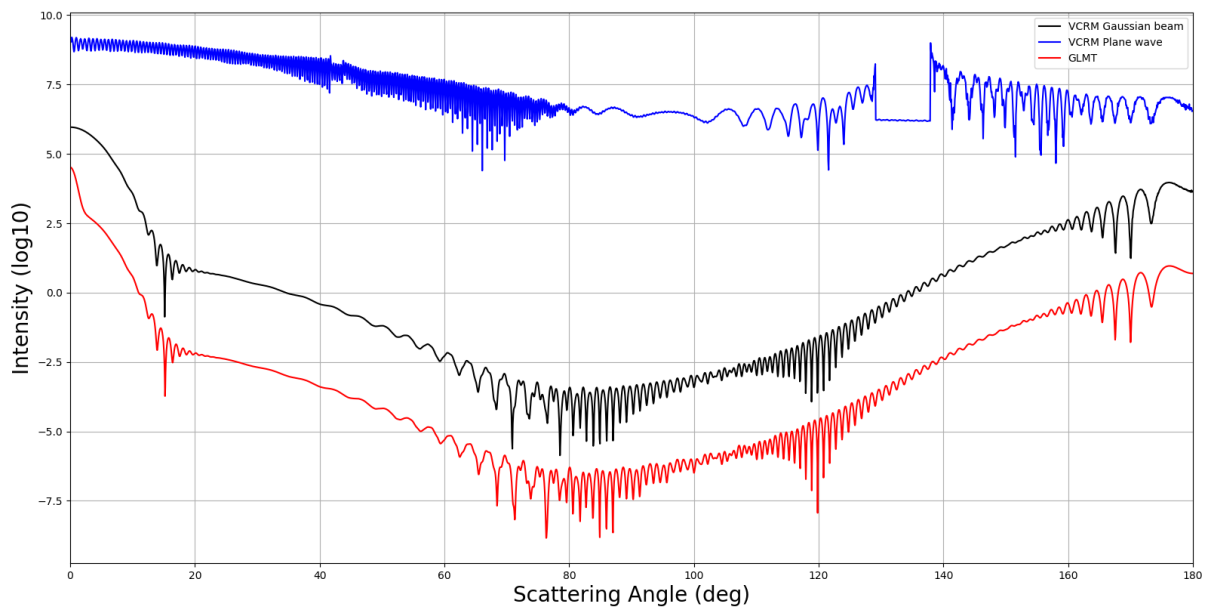


Figure 70: The parameters are the same as in Figure 69, except that $\omega_0 = 10\mu\text{m}$ for the VCRM Gaussian beam (black) and GLMT (red) cases.

Finally, Figure 71 highlights the fact that as the radius of a sphere gets smaller, and becomes not much bigger than the wavelength of the light, the agreement between the scattering of the VCRM Gaussian beam and that of GLMT becomes lower. This leads to the lower particle size limit of VCRM, where accurate results can only be expected for $a = b = c \gg \lambda$.

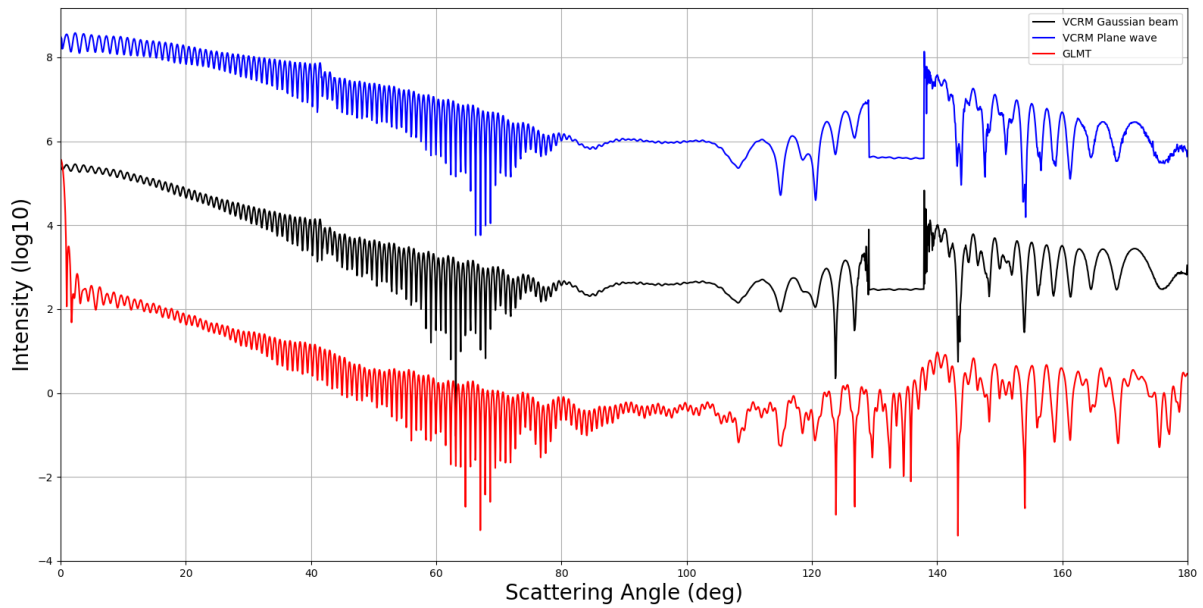


Figure 71: Scattering diagram showing the intensity distribution (in \log_{10}) across the angle range, 0° to 180° , for light scattered by a sphere using a VCRM plane wave (blue), a VCRM Gaussian beam (black), and GLMT (red). Calculation parameters: $a = b = c = 25\mu\text{m}$, $m = 1.333$, $\omega_0 = 25\mu\text{m}$ and $\theta_{inc} = 0^\circ$. Here, the plane wave case (blue) has been offset by 10^3 , and the GLMT calculation (red) has been offset by 10^{-3} , in the interest of clarity.

B-4.2. Scattering diagrams for spheroids

Figure 72 to Figure 74 show the VCRM plane wave and Gaussian beam scattering by an oblate spheroid ($k = 0.8$) of large size (with $a = b = 125\mu\text{m}$ and $c = 100\mu\text{m}$) for different angles of incidence, namely $\theta = 0, 20, 40^\circ$, respectively. The effect of the Gaussian beam can be seen clearly when compared to the plane wave case. We observe that the scattered intensities in the forward and backward direction are of the same order for the plane wave and the Gaussian beam. This is because the main contributors to this part of the scattering diagram are rays that struck the particle near the beam axis. Using the same logic, the scattered intensities for the beam are much weaker on either side of the incident direction, because most of the contributing rays are from near the border of the beam. The rainbows, if visible, are located at the same place for the plane wave and the Gaussian beam, since the beam is relatively large, so the incident rays are almost all parallel, as are the rays of the plane wave.

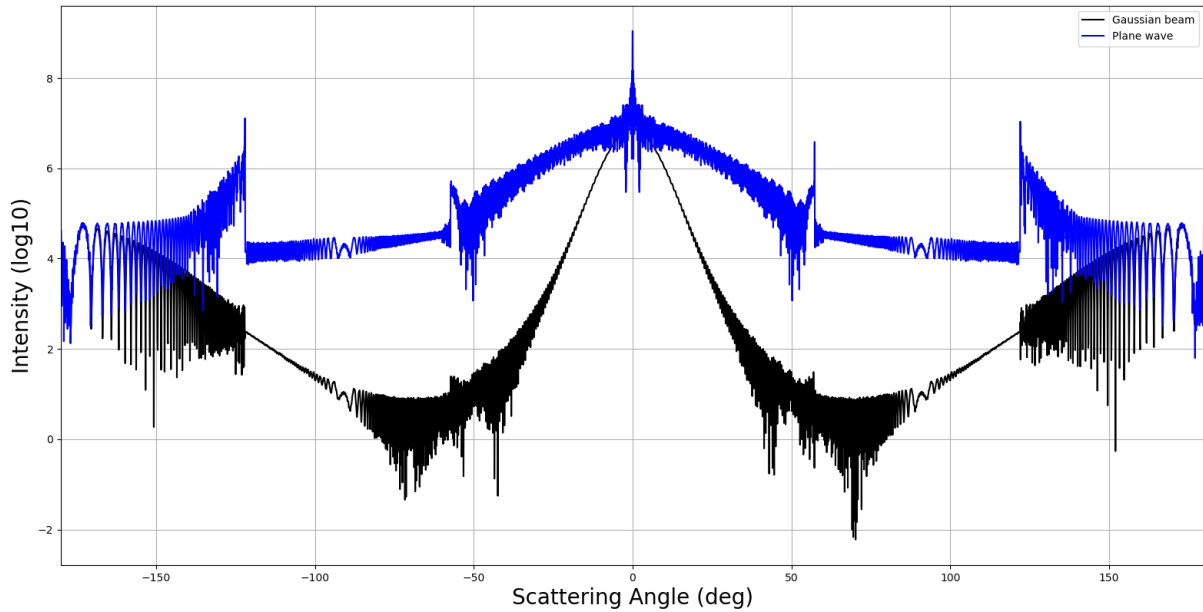


Figure 72: Scattering diagram showing the intensity distribution (in \log_{10}) across the angle range, -180° to 180° , for light scattered by a spheroid using a VCRM plane wave (blue) and a VCRM Gaussian beam (black). Calculation parameters: $a = b = 125\mu\text{m}$, $c = 100\mu\text{m}$, $m = 1.333$, $\omega_0 = 50\mu\text{m}$ and $\theta_{inc} = 0^\circ$. There is no offset in intensity in these diagrams.

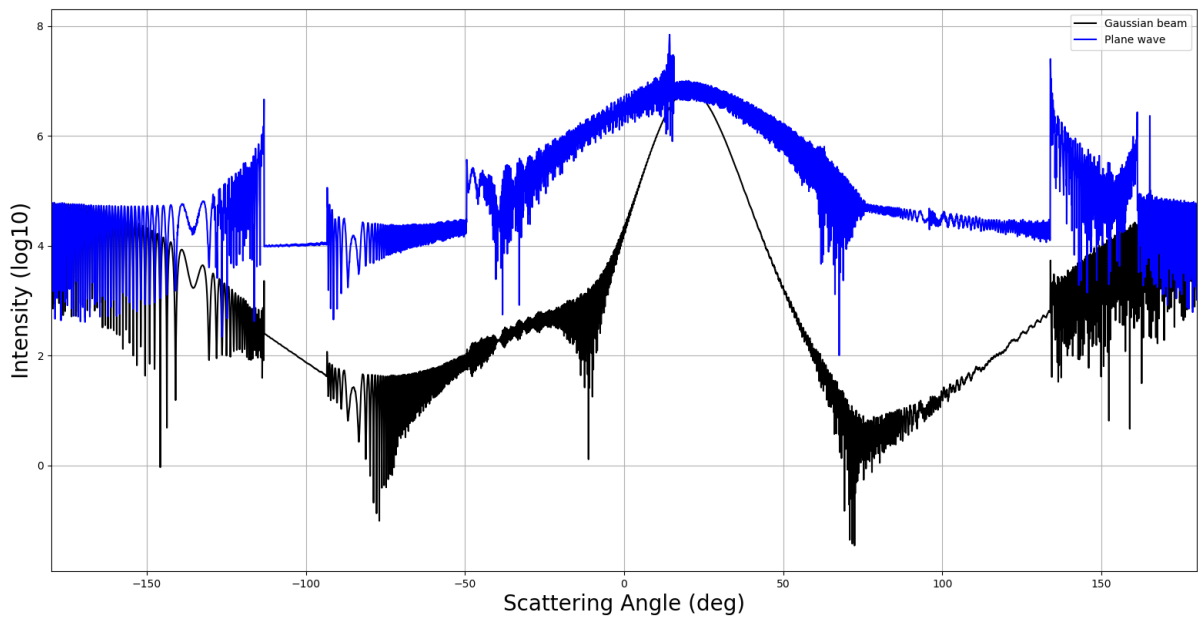


Figure 73: The parameters are the same as in Figure 72, except that $\theta_{inc} = 20^\circ$ for both the VCRM plane wave (blue), and the VCRM Gaussian beam (black) cases.

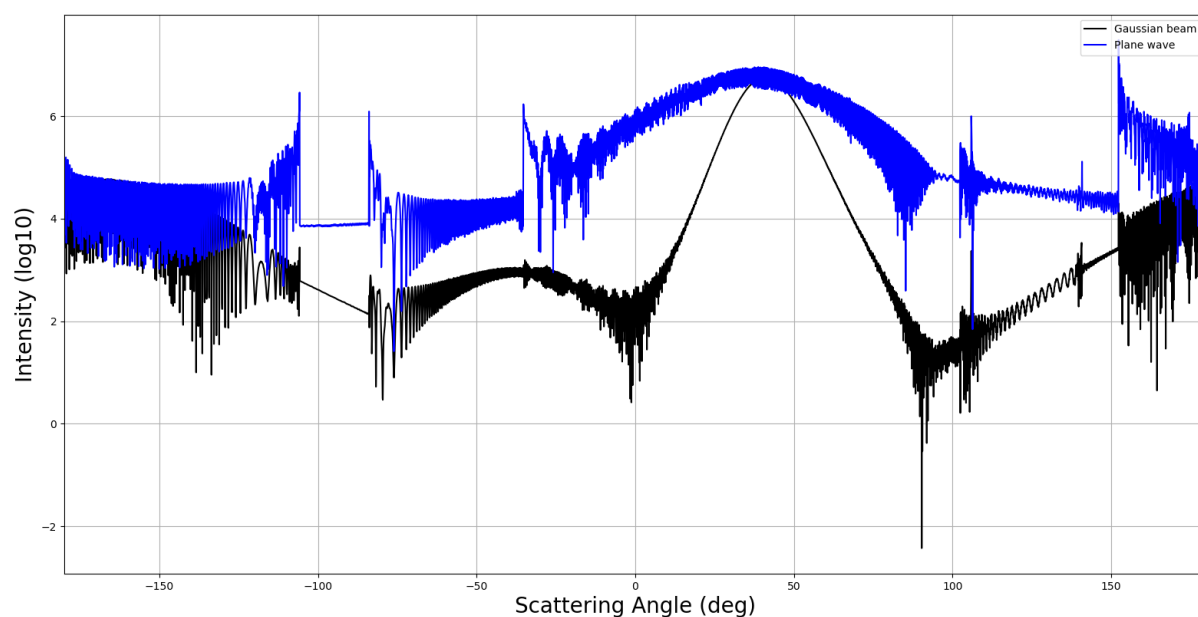


Figure 74: The parameters are the same as in Figure 72, except that $\theta_{inc} = 40^\circ$ for both the VCRM plane wave (blue), and the VCRM Gaussian beam (black) cases.

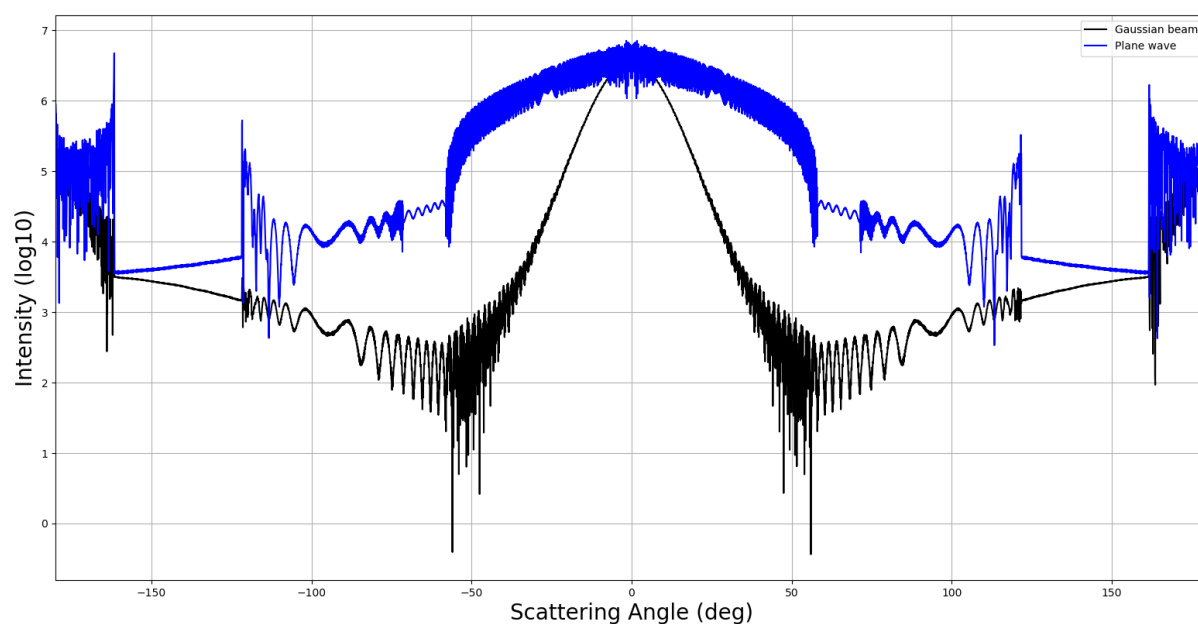


Figure 75: Scattering diagram showing the intensity distribution (in \log_{10}) across the angle range, -180° to 180° , for light scattered by a spheroid using a VCRM plane wave (blue) and a VCRM Gaussian beam (black). Calculation parameters: $a = b = 100\mu\text{m}$, $c = 120\mu\text{m}$, $m = 1.333$, $\omega_0 = 50\mu\text{m}$ and $\theta_{inc} = 0^\circ$. There is no offset in intensity in these diagrams.

Figure 75 to Figure 77 show the scattering of a VCRM plane wave and a Gaussian beam, this time by a prolate spheroid ($k = 1.2$) of similar size to the previous oblate example (with $a = b = 100\mu\text{m}$ and $c = 120\mu\text{m}$). Similar comments as those made for the case of oblate particles

can be made concerning the scattered intensity of prolate particles. Furthermore, we can note that the rainbow positions depend on the incident angle and the aspect ratio, which is something that is also true for oblate spheroids.

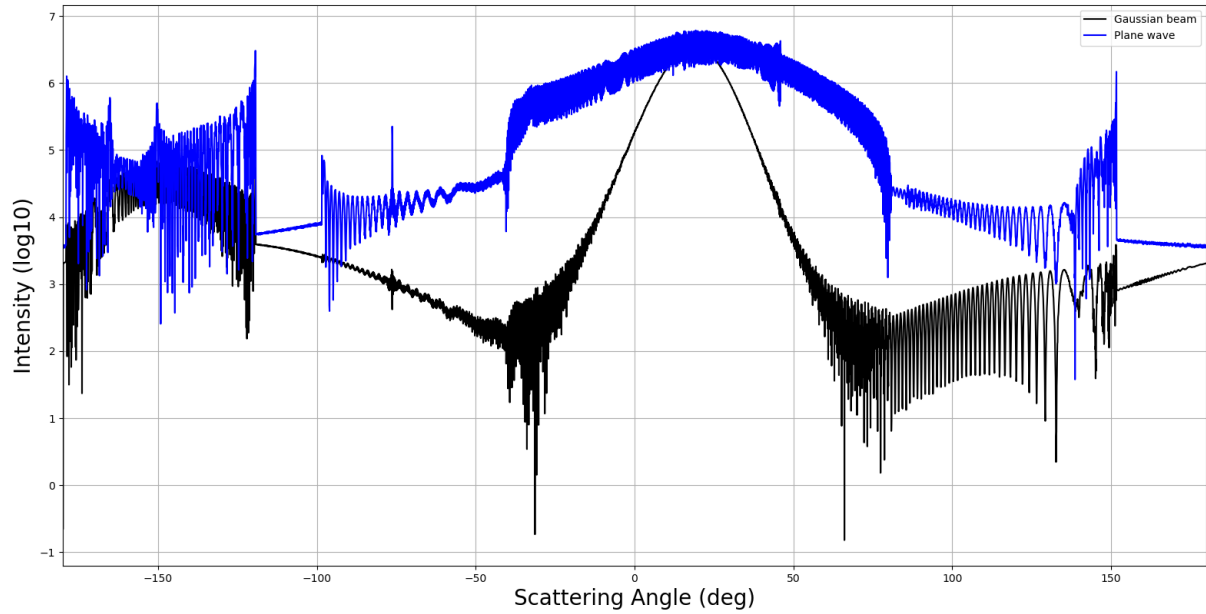


Figure 76: The parameters are the same as in Figure 75, except that $\theta_{inc} = 20^\circ$ for both the VCRM plane wave (blue), and the VCRM Gaussian beam (black) cases.

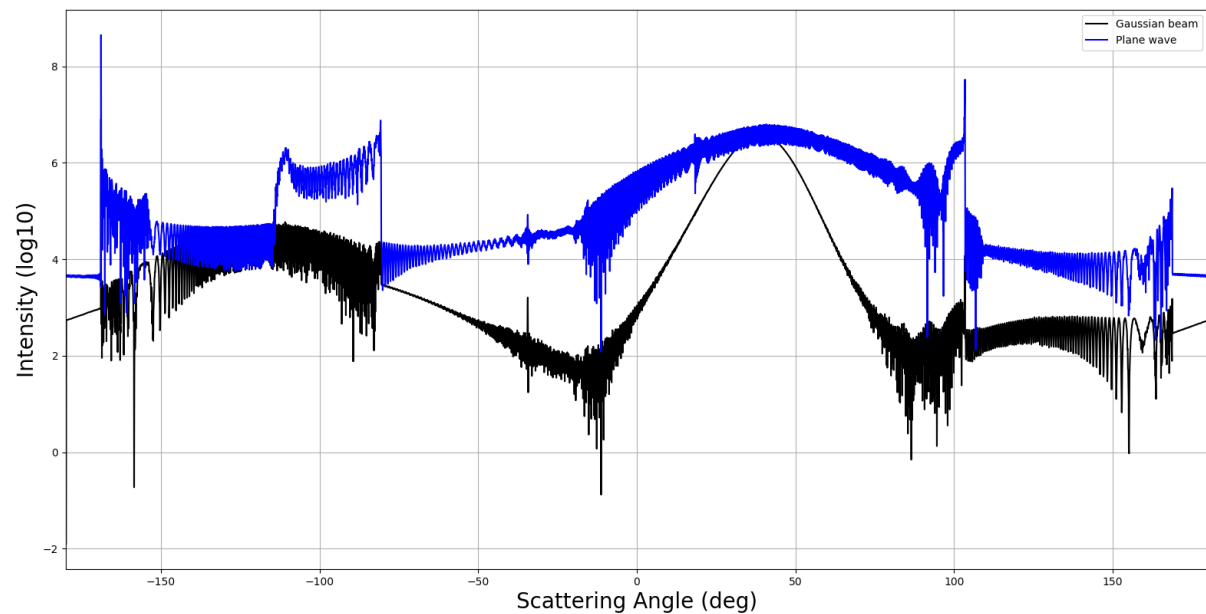


Figure 77: The parameters are the same as in Figure 75, except that $\theta_{inc} = 40^\circ$ for both the VCRM plane wave (blue), and the VCRM Gaussian beam (black) cases.

B-5. Conclusion of Section B

Classical GO was modified by adding wave properties to rays, with the resulting model being the Vectorial Complex Ray Model. This concept was then used in the scattering of both a plane wave and a Gaussian beam by spheres and spheroids. To validate VCRM, the results for spheres were compared with rigorous GLMT calculations, which exhibited good agreement for large particles (where the radius is $\gg 10\lambda$), except at the rainbow angle, and in a narrow range of angles near the angle of incidence. The latter is due to diffraction, which has not been added to the model used for the calculations in this thesis, and the former is a notorious problem with GO approximations.

The model was also used for spheroidal particles. Due to the nature of the calculations, it is easily possible to rotate the particle with respect to the direction of the illuminating light, which holds great flexibility for the characterisation of arbitrarily shaped particles.

The Gaussian scattering profile is easily distinguished from the plane wave, with clear Gaussian characteristics being visible when the beam waist radius is smaller than the particle principle axes.

The first improvement that needs to be included in the current VCRM model is diffraction, so as to match GLMT calculations more closely in the forward scattering direction for large particles.

The second is to extend it to a 3D version, so as to encapsulate the full aspect of light scattering, although this is no easy task, especially due to the interpolation component that is necessary for this model to work.

Once 3D scattering is achieved, optical forces acting on the particle may be incorporated so that the model may be compared and validated with a type of experimental results other than intensity patterns. For example, the levitation powers from Part A would serve as a great tool for comparison.

The following step would be to focus on the analysis of particle dynamics, such as those presented in Section A-3.3, some of which can only be analysed with simulations that have access to all three spatial dimensions. This is possible for a model such as VCRM because of the fast processing times, which could potentially analyse dynamics in minutes, or hours on a

normal computer. This is unlike other, more rigorous models, that may require days of processing on a supercomputer just to calculate the forces acting only on a large, arbitrarily shaped particle in a single position and orientation.

General Conclusion

The aim of this work was to cross experimental information about the mechanical effects of light on particles with simulations.

The focus was placed on the case of spheroids, meaning circularly symmetrical ellipsoid-shaped particles, which are the simplest of the family, “complex-shaped particles”. The particles used were made from polystyrene, with sizes of up to several tens of micrometres in length, which lies within the size domain targeted by the AMOCOPS project.

Systematic experiments concerning the optical levitation, and the 3D optical trapping of such particles was carried out. A large quantity of data has been gathered, documenting the responses of these particles to laser beams, either of low apertures, as in the OL setup, or tightly focused, as with the OT. It was observed that the ellipsoids could be stably trapped in 3D by OT, and that non-trivial static configurations could be produced in a two-beam OL with appropriate ratios of the powers of both beams.

Characteristics of the static equilibria of the particles are directly exploitable for comparison with numerical simulations. In some cases, it was possible to use “exact methods”, such as GLMT and MLFMA, to calculate levitation powers. GLMT was used for spheres, whilst MLFMA was used for the ellipsoids levitated using a one-beam OL, in the simplest configuration, where the particle stands vertically and is centred on the beam axis. The study with spheres allowed us to detect a small absorbance by the material of the particles (mainly polystyrene), a parameter which was necessary to be taken into account to reach quantitative agreement between experimental and GLMT values of the levitation power, P_{lev} . Noteworthy, this method is novel, since previous attempts to measure the absorbance of such particles dealt with suspensions containing many of them [87], instead of the use of a few specimens.

As for the levitation of ellipsoids, the agreement with MLFMA was only qualitative due to large scatter of both the experimental and calculated values of P_{lev} . Reasons for the dispersions of the respective P_{lev} values, as a function of the particle aspect ratio (k), are not yet clear to us. Refinements are possible in the experimental procedure, and many more MLFMA calculations are necessary along a fine grid along the axis containing k , in order to possibly evidence the role of particle resonances.

Oblique configurations of ellipsoids in a two-beam OL, and trapping configurations in OT, have only been explored with standard RO simulations, limited to two dimensions. The simulation did rather well in recovering the main characteristics of most of the experimental configurations. In particular, the mechanisms for the oblique, off-centred equilibria, and the influence of spherical aberration in 3D trapping of the ellipsoids could be understood with the help of the simulations. However, and not surprisingly, the simple 2D RO simulation is not quantitatively reliable, and indeed, predicted values of characteristic parameters do not closely match measured ones. As no source of systematic bias has been noticed so far in the experimental measurements, it is supposed that the differences mainly stem from the limitations of the basic RO model, and from the restriction to 2D in the current version of the simulation.

Basic ray-optics ignores the wave nature of light, meaning that rays scattered by the particle do not interfere. Ignoring these interferences is obviously a source of systematic error in the calculation of the scattering diagram, as well as in the momentum transfer from the light to the particle. The VCRM method [2, 3] recently developed by K. F. Ren is a promising option to approximately reconcile rays with the wave character of light in a practical framework which may apply to any particle shape. The principles of the method are explained, with which a Python version has been coded for the scattering of a plane wave and a Gaussian beam by an ellipsoid in a symmetric plane. This is an extension of the preliminary work for the on-axis Gaussian beam scattering by a spheroid [78], to the scattering of any incident Gaussian beam by an ellipsoid of any orientation [81]. The power of the method was illustrated by efficiently calculating scattering diagrams of ellipsoids illuminated by a Gaussian beam. Unfortunately, it was a lack of time that has caused the lack of elaboration for force maps with VCRM, and to then compare these maps to those calculated with simple 2D RO (the method used by J.C. Loudet).

An important part of this thesis has been dedicated to the dynamical responses of the particles in the OL and OT setups. The observations made here have confirmed those made prior to this work by Mihiretie et al., and thereby the conception that responses of particles to light should be thought of as dynamical states in general. In the course of the two-beam OL experiments, two new types of oscillations involving large angular excursions of the particle were identified, both in the polar and azimuthal angles.

It was verified that oscillations in the OL sensitively depend on the beam waist and the particle aspect ratio. Conversely, it was observed that the ellipsoids were always stably trapped in the OT when in bulk water, but that oscillations were produced for specific configurations with the

particle in contact to the lower boundary of the cell. Interestingly, these oscillations were found to be incoherent, contrary to the types of regular oscillations in the OL.

Our understanding is that the oscillations seen in the OT experiments are of the type described by Simpson and Hanna [56], namely thermal noise-driven oscillations within the linear domain of the force-torque field acting on the particle. Conversely, thermal noise plays no role in the large amplitude oscillations seen in the OL setup [37]. The latter oscillations stem from the nonlinear coupling between translational and rotational degrees of freedom within the force-torque field, hence the distinction made between noise-driven and nonlinear oscillations.

We end this conclusion with suggestions for future developments.

The work with 2D-VCRM is to be continued with calculations of force-torque maps. It will be especially interesting to test the influence of phases in these maps compared to maps obtained with standard RO, where interference is not taken into account [39]. The comparison would be a quantitative test of the accuracy of basic RO, which is a much better way to refute it than the standard statement that RO is inaccurate whenever a characteristic distance in the system is not large enough compared to the wavelength.

3D-VCRM is then the obvious progression of the model. It may reach a reasonable quantitative match between calculated and observed static configurations, which would be a great way to validate it.

A much more ambitious goal is to simulate dynamic states in 3D. This task demands a huge amount of computation, because forces and torques must be calculated within the full 5-dimensional configuration space of the particle. This is certainly beyond practical possibility with MLFMA, due to prohibitive computation times. In this context, 3D-VCRM is the only possible method for computations to be fast enough.

The accuracy of experimental observations can still be improved at different levels:

- ❖ Controlling the temperature of the sample cell in the OL setup is technically difficult, if the side view is to be preserved. However, it is mandatory to eliminate the uncertainty produced by temperature in the graphs showing P_{lev} against v_{sed} .
- ❖ The position of the particle relative to the beam waist plane also needs to be controlled more accurately. This may be feasible using an automated real-time analysis of the

top view images of the particle. The method may bring the uncertainty in particle altitude down to about a micrometre.

- ❖ A detailed analysis of the particle oscillations in terms of their “true coordinates”, (x, y, z, θ, ϕ) , demands developing dedicated tracking software tools far more sophisticated than the crude version used in our experiments.

Bibliography

- [1] F. M. Kahnert, "Numerical methods in electromagnetic scattering theory," *Journal of Quantitative Spectroscopy and Radiative Transfer*, Vols. 79-80, pp. 775-824, 2003.
- [2] K. F. Ren, F. Onofri, C. Roze and T. Girasole, "Vectorial complex ray model and application to two-dimensional scattering of plane wave by a spheroidal particle," *Optics Letters*, vol. 36, no. 3, pp. 370-372, 2011.
- [3] K. F. Ren, C. Roze and T. Girasole, "Scattering and transversal divergence of an ellipsoidal particle by using Vectorial Complex Ray Model," *Journal of Quantitative Spectroscopy and Radiative Transfer*, vol. 113, no. 18, pp. 2419-2423, 2012.
- [4] K. Jiang, X. Han and K. F. Ren, "Scattering from an elliptical cylinder by using the vectorial complex ray model," *Applied Optics*, vol. 51, no. 34, pp. 8159-8168, 2012.
- [5] F. R. A. Onofri, K. F. Ren, M. Sentis, Q. Gaubert and C. Pelce, "Experimental validation of the vectorial complex ray model on the inter-caustics scattering of oblate droplets," *Optics Express*, vol. 23, no. 12, pp. 15768-15773, 2015.
- [6] M. Yang, Y. Wu, X. Sheng and K. F. Ren, "Comparison of scattering diagrams of large non-spherical particles calculated by VCRM and MLFMA," *Journal of Quantitative Spectroscopy and Radiative Transfer*, vol. 162, pp. 143-153, 2015.
- [7] A. Ashkin, "Acceleration and trapping of particles by radiation pressure," *Physical Review Letters*, vol. 24, no. 4, pp. 156-159, 1970.
- [8] A. Ashkin, J. M. Dziedzic, J. E. Bjorkholm and S. Chu, "Observation of a single-beam gradient force optical trap for dielectric particles," *Optics Letters*, vol. 11, no. 5, pp. 288-290, 1986.
- [9] K. C. Neuman and S. M. Block, "Optical trapping," *Review of Scientific Instruments*, vol. 75, no. 9, pp. 2787-2809, 2004.
- [10] J. N. Wilking and T. G. Mason, "Multiple trapped states and angular Kramers hopping of complex dielectric shapes in a simple optical trap," *Europhysics Letters*, vol. 81, no. 5, 2008.
- [11] A. A. R. Neves, A. Camposeo, S. Pagliara, R. Saija, F. Borghese, P. Denti, M. A. Iati, R. Cingolani, O. M. Marago and D. Pisignano, "Rotational dynamics of optically trapped nanofibers," *Optics Express*, vol. 18, no. 2, pp. 822-830, 2010.

- [12] P. J. Pauzauskie, A. Radenovic, E. Trepagnier, H. Shroff, P. Yang and J. Liphardt, "Optical trapping and integration of semiconductor nanowire assemblies in water," *Nature Materials*, vol. 5, pp. 97-101, 2006.
- [13] A. van der Horst, A. I. Campbell, L. K. van Vugt, D. A. Vanmaekelbergh, M. Dogterom and A. van Blaaderen, "Manipulating metal-oxide nanowires using counter-propagating optical line tweezers," *Optics Express*, vol. 15, no. 18, pp. 11629-11639, 2007.
- [14] J. Plewa, E. Tanner, D. Mueth and D. Grier, "Processing carbon nanotubes with holographic optical tweezers," *Optics Express*, vol. 12, no. 9, pp. 1978-1981, 2004.
- [15] M. E. J. Friese, H. Rubinsztein-Dunlop, J. Gold, P. Hagberg and D. Hanstorp, "Optically driven micromachine elements," *Applied Physics Letters*, vol. 78, no. 4, pp. 547-549, 2001.
- [16] S. H. Simpson, "Inhomogeneous and anisotropic particles in optical traps: Physical behaviour and applications," *Journal of Quantitative Spectroscopy and Radiative Transfer*, vol. 146, pp. 81-99, 2014.
- [17] S. H. Simpson and S. Hanna, "Holographic optical trapping of microrods and nanowires," *Journal of the Optical Society of America A*, vol. 27, no. 6, pp. 1255-1264, 2010.
- [18] Y. Cao, A. B. Stilgoe, L. Chen, T. A. Nieminen and H. Rubinsztein-Dunlop, "Equilibrium orientations and positions of non-spherical particles in optical traps," *Optics Express*, vol. 20, no. 12, pp. 12987-12996, 2012.
- [19] R. C. Gauthier, "Theoretical investigation of the optical trapping force and torque on cylindrical micro-objects," *Journal of the Optical Society of America B*, vol. 14, no. 12, pp. 3323-3333, 1997.
- [20] R. C. Gauthier, M. Ashman and C. P. Grover, "Experimental confirmation of the optical-trapping properties of cylindrical objects," *Applied Optics*, vol. 38, no. 22, pp. 4861-4869, 1999.
- [21] P. B. Bareil and Y. Sheng, "Angular and position stability of a nanorod trapped in an optical tweezers," *Optics Express*, vol. 18, no. 25, pp. 26388-26398, 2010.
- [22] S. H. Simpson and S. Hanna, "Optical trapping of microrods: variation with size and refractive index," *Journal of the Optical Society of America A*, vol. 28, no. 5, pp. 850-858, 2011.
- [23] S. H. Simpson and S. Hanna, "Optical trapping of spheroidal particles in Gaussian beams," *Journal of the Optical Society of America A*, vol. 24, no. 2, pp. 430-443, 2007.
- [24] S. H. Simpson and S. Hanna, "Computational study of the optical trapping of ellipsoidal particles," *Physical Review A*, vol. 84, no. 5, 2011.

- [25] H. Sosa-Martinez and J. C. Gutierrez-Vega, "Optical forces on a Mie spheroidal particle arbitrarily oriented in a counterpropagating trap," *Journal of the Optical Society of America B*, vol. 26, no. 11, pp. 2109-2116, 2009.
- [26] C. B. Chang, W. X. Huang, K. H. Lee and H. J. Sung, "Optical levitation of a non-spherical particle in a loosely focused Gaussian beam," *Optics Express*, vol. 20, no. 21, pp. 24068-24084, 2012.
- [27] J. Guck, R. Ananthakrishnan, H. Mahmood, T. J. Moon, C. C. Cunningham and J. Kas, "The Optical Stretcher: A Novel Laser Tool to Micromanipulate Cells," *Biophysical Journal*, vol. 81, no. 2, pp. 767-784, 2001.
- [28] K. F. Ren, *ABSphere, Version 1.10*, <http://amocops.univ-rouen.fr/en/content/download>.
- [29] K. F. Ren, G. Grehan and G. Gouesbet, "Radiation pressure forces exerted on a particle arbitrarily located in a Gaussian beam by using the generalized Lorenz-Mie theory, and associated resonance effects," *Optics Communications*, vol. 108, no. 4-6, pp. 343-354, 1994.
- [30] K. F. Ren, G. Grehan and G. Gouesbet, "Prediction of reverse radiation pressure by generalized Lorenz-Mie theory," *Applied Optics*, vol. 35, no. 15, pp. 2702-2710, 1996.
- [31] F. Xu, K. F. Ren, G. Gouesbet, X. Cai and G. Grehan, "Theoretical prediction of radiation pressure force exerted on a spheroid by an arbitrarily shaped beam," *Physical Review E*, vol. 75, no. 2, 2007.
- [32] G. Roosen and C. Imbert, "Optical levitation by means of two horizontal laser beams: A theoretical and experimental study," *Physics Letters A*, vol. 59, no. 1, pp. 6-8, 1976.
- [33] G. Roosen, "A theoretical and experimental study of the stable equilibrium positions of spheres levitated by two horizontal laser beams," *Optics Communications*, vol. 21, no. 1, pp. 189-194, 1977.
- [34] R. Li, K. F. Ren, X. Han, Z. Wu, L. Guo and S. Gong, "Analysis of radiation pressure force exerted on a biological cell induced by high-order Bessel beams using Debye series," *Journal of Quantitative Spectroscopy and Radiative Transfer*, vol. 126, pp. 69-77, 2013.
- [35] B. M. Mihiretie, P. Snabre, J. C. Loudet and B. Pouligny, "Radiation pressure makes ellipsoidal particles tumble," *Europhysics Letters*, vol. 100, no. 4, 2012.
- [36] B. M. Mihiretie, J. C. Loudet and B. Pouligny, "Optical levitation and long-working-distance trapping: From spherical up to high aspect ratio ellipsoidal particles," *Journal of Quantitative Spectroscopy and Radiative Transfer*, vol. 126, pp. 61-68, 2013.

- [37] B. M. Mihiretie, P. Snabre, J.-C. Loudet and B. Pouligny, "Optically driven oscillations of ellipsoidal particles. Part I: Experimental observations," *The European Physical Journal E*, vol. 37, no. 12, 2014.
- [38] Z. Cheng, T. G. Mason and P. M. Chaikin, "Periodic oscillation of a colloidal disk near a wall in an optical trap," *Physical Review E*, vol. 68, no. 5 Part 1, 2003.
- [39] J.-C. Loudet, B. M. Mihiretie and B. Pouligny, "Optically driven oscillations of ellipsoidal particles. Part II: Ray-optics calculations," *The European Physical Journal E*, vol. 37, no. 12, 2014.
- [40] M. Yang, K. F. Ren, T. Petkov, B. Pouligny, J. C. Loudet and X. Sheng, "Computational study of radiation torque on arbitrary shaped particles with MLFMA," *Optics Express*, vol. 23, no. 18, pp. 23365-23379, 2015.
- [41] J. A. Champion, Y. K. Katare and S. Mitragotri, "Making polymeric micro- and nanoparticles of complex shapes," *Proceedings of the National Academy of Sciences*, vol. 104, no. 29, pp. 11901-11904, 2007.
- [42] C. C. Ho, A. Keller, J. A. Odell and R. H. Ottewill, "Preparation of monodisperse ellipsoidal polystyrene particles," *Colloid and Polymer Science*, vol. 271, no. 5, p. 469–479, 1993.
- [43] J. Happel and H. Brenner, *Low Reynolds Number Hydrodynamics*, The Hague: Springer Netherlands, 1983.
- [44] E. Guazzelli and J. F. Morris, *A Physical Introduction to Suspension Dynamics*, Cambridge: Cambridge University Press, 2012.
- [45] M. I. Angelova and B. Pouligny, "Trapping and levitation of a dielectric sphere with off-centred Gaussian beams. I. Experimental," *Pure and Applied Optics: Journal of the European Optical Society Part A*, vol. 2, no. 4, pp. 261-276, 1993.
- [46] F. Nadal, A. Dazzi, F. Argoul and B. Pouligny, "Probing the confined dynamics of a spherical colloid close to a surface by combined optical trapping and reflection interference contrast microscopy," *Applied Physics Letters*, vol. 79, no. 23, pp. 3887-3889, 2001.
- [47] A. Giroto, N. Danne, A. Wurger, T. Bickel, K. F. Ren, J. C. Loudet and B. Pouligny, "Motion of optically heated spheres at the water-air interface," *Langmuir*, vol. 32, no. 11, pp. 2687-2697, 2016.
- [48] A. E. Siegman, *Lasers*, USA: University Science Books, 1986.

- [49] A. Jonas and P. Zemanek, "Light at work: the use of optical forces for particle manipulation, sorting, and analysis," *Electrophoresis*, vol. 29, no. 24, pp. 4813-4851, 2008.
- [50] G. M. Gibson, J. Leach, S. Keen, A. J. Wright and M. J. Padgett, "Measuring the accuracy of particle position and force in optical tweezers using high-speed video microscopy," *Optics Express*, vol. 16, no. 19, pp. 14561-14570, 2008.
- [51] G. Roosen and S. Slansky, "Influence of the beam divergence on the exerted force on a sphere by a laser beam and required conditions for stable optical levitation," *Optics Communications*, vol. 29, no. 3, pp. 341-346, 1979.
- [52] I. H. Malitson, "Interspecimen Comparison of the Refractive Index of Fused Silica," *Journal of the Optical Society of America*, vol. 55, no. 10, pp. 1205-1209, 1965.
- [53] G. Martinot-Lagarde, B. Pouligny, M. I. Angelova, G. Grehan and G. Gouesbet, "Trapping and levitation of a dielectric sphere with off-centred Gaussian beams. II. GLMT analysis," *Pure and Applied Optics*, vol. 4, no. 5, pp. 571-585, 1995.
- [54] R. Dimova and B. Pouligny, "Absorbing microspheres in water: laser radiation pressure and hydrodynamic forces," *Scattering of Shaped Light Beams and Applications*, pp. 45-65, 2000.
- [55] A. Ashkin, "Forces of a single-beam gradient laser trap on a dielectric sphere in the ray optics regime," *Biophysical Journal*, vol. 61, no. 2, pp. 569-582, 1992.
- [56] S. H. Simpson and S. Hanna, "First-order nonconservative motion of optically trapped nonspherical particles," *Physical Review E*, vol. 82, 2010.
- [57] A. Rohrbach, "Stiffness of optical traps: quantitative agreement between experiment and electromagnetic theory," *Physical Review Letters*, vol. 95, no. 16, 2005.
- [58] N. Malagnino, G. Pesce, A. Sasso and E. Arimondo, "Measurements of trapping efficiency and stiffness in optical tweezers," *Optics Communications*, vol. 214, no. 1-6, pp. 15-24, 2002.
- [59] G. Gouesbet and G. Grehan, *Generalized Lorenz-Mie Theories*, First ed., Berlin: Springer, 2011, pp. 86-87.
- [60] M. Yang, K. F. Ren, M. Gou and X. Sheng, "Computation of radiation pressure force on arbitrary shaped homogenous particles by multilevel fast multipole algorithm," *Optics Letters*, vol. 38, no. 11, pp. 1784-1786, 2013.
- [61] A. Hinojosa-Alvarado and J. C. Gutierrez-Vega, "Geometrical optics calculation of forces and torques produced by a ringed beam on a prolate spheroid," *Journal of the Optical Society of America B*, vol. 27, no. 8, pp. 1651-1658, 2010.

- [62] J. Y. Walz and D. C. Prieve, "Prediction and measurement of the optical trapping forces on a microscopic dielectric sphere," *Langmuir*, vol. 8, no. 12, pp. 3073-3082, 1992.
- [63] A. S. Glassner, *An Introduction to Ray Tracing*, San Francisco: Morgan Kaufmann, 1989.
- [64] T. J. Petkov, M. Yang, K. F. Ren, B. Pouligny and J.-C. Loudet, "Behaviours of ellipsoidal micro-particles within a two-beam optical levitator," *Journal of Quantitative Spectroscopy & Radiative Transfer*, vol. 195, pp. 85-96, 2017.
- [65] Y. Han, A. Alsayed, M. Nobili and A. G. Yodh, "Quasi-two-dimensional diffusion of single ellipsoids: Aspect ratio and confinement effects," *Physical Review E*, vol. 80, 2009.
- [66] W. H. Wright, G. J. Sonek and M. W. Berns, "Radiation trapping forces on microspheres with optical tweezers," *Applied Physics Letters*, vol. 63, no. 6, pp. 715-717, 1993.
- [67] E. Fallman and O. Axner, "Influence of a glass-water interface on the on-axis trapping of micrometer-sized spherical objects by optical tweezers," *Applied Optics*, vol. 42, no. 19, pp. 3915-3926, 2003.
- [68] K. C. Vermeulen, G. J. L. Wuite, G. J. M. Stienen and C. F. Schmidt, "Optical trap stiffness in the presence and absence of spherical aberrations," *Applied Optics*, vol. 45, no. 8, pp. 1812-1819, 2006.
- [69] W. J. Toe, I. Ortega-Piwonka, C. N. Angstmann, Q. Gao, H. H. Tan, C. Jagadish, B. I. Henry and P. J. Reece, "Nonconservative dynamics of optically trapped high-aspect-ratio nanowires," *Physical Review E*, vol. 93, no. 2, 2016.
- [70] V. P. Maltsev and K. Semyanov, *Characterisation of Bio-Particles from Light Scattering*, Leiden: Koninklijke Brill, 2004.
- [71] M. I. Mishchenko, L. D. Travis and D. W. Mackowski, "T-matrix computations of light scattering by nonspherical particles: A review," *Journal of Quantitative Spectroscopy and Radiative Transfer*, vol. 55, no. 5, pp. 535-575, 1996.
- [72] M. I. Mishchenko, L. D. Travis and A. A. Lacis, *Scattering, Absorption, and Emission of Light by Small Particles*, Cambridge: Cambridge University Press, 2002.
- [73] E. Bae, H. Zhang and E. D. Hirtleman, "Application of the discrete dipole approximation for dipoles embedded in film," *Journal of the Optical Society of America A*, vol. 25, no. 7, pp. 1728-1736, 2008.
- [74] M. A. Yurkin and M. Huntemann, "Rigorous and Fast Discrete Dipole Approximation for Particles near a Plane Interface," *The Journal of Physical Chemistry C*, vol. 119, no. 52, p. 29088-29094, 2015.

- [75] S. A. Palkar, N. P. Ryde, M. R. Schure, N. Gupta and J. B. Cole, "Finite Difference Time Domain Computation of Light Scattering by Multiple Colloidal Particles," *Langmuir*, vol. 14, no. 13, p. 3484–3492, 1998.
- [76] H. C. van de Hulst, *Light scattering by small particles*, New York: Dover Publications, Inc., 1981.
- [77] F. Xu, K. F. Ren and X. Cai, "Extension of geometrical-optics approximation to on-axis Gaussian beam scattering. I. By a spherical particle," *Applied Optics*, vol. 45, no. 20, pp. 4990-4999, 2006.
- [78] F. Xu, K. F. Ren, X. Cai and J. Shen, "Extension of geometrical-optics approximation to on-axis Gaussian beam scattering. II. By a spheroidal particle with end-on incidence," *Applied Optics*, vol. 45, no. 20, pp. 5000-5009, 2006.
- [79] T. A. Nieminen, H. Rubinsztein-Dunlop and N. R. Heckenberg, "Calculation and optical measurement of laser trapping forces on non-spherical particles," *Journal of Quantitative Spectroscopy and Radiative Transfer*, vol. 70, no. 4-6, pp. 627-637, 2001.
- [80] C. F. Bohren and D. R. Huffman, *Absorption and Scattering of Light by Small Particles*, New York: J. Wiley and sons, 1983.
- [81] Y. Yuan, *Diffusion de la lumière par un objet irrégulier pour l'application à l'imagerie des sprays*, Rouen: Université de Rouen, 2012.
- [82] E. Hecht, *Optics*, 4th ed., San Francisco: Addison Wesley, 2002.
- [83] G. A. Deschamps, "Ray techniques in electromagnetics," *Proceedings of the Institute of Electrical and Electronics Engineers*, vol. 60, no. 9, pp. 1022-1035, 1972.
- [84] W. F. Harris, "Curvature of ellipsoids and other surfaces," *Ophthalmic and Physiological Optics*, vol. 26, no. 5, pp. 497-501, 2006.
- [85] M. A. Bandres and J. C. Gutierrez-Vega, "Ince-Gaussian beams," *Optics Letters*, vol. 29, no. 2, 2004.
- [86] R. Goldman, "Curvature formulas for implicit curves and surfaces," *Computer Aided Geometric Design*, vol. 22, pp. 632-658, 2005.
- [87] X. Ma, J. Q. Lu, R. S. Brock, K. M. Jacobs, P. Yang and X. Hu, "Determination of complex refractive index of polystyrene microspheres from 370 to 1610 nm," *Physics in Medicine and Biology*, vol. 48, no. 24, pp. 4165-4172, 2003.

Appendices

Sedimentation of spheroids in viscous fluid

Consider a spheroidal particle moving under the sole action of gravity in a fluid of viscosity η . $a = b = \frac{c}{k}$ are the size parameters of the particle (see Figure 2). The particle and its velocity are small enough for inertia forces and torques to be negligible. Here, we briefly recall the results from [43, 44], which are used later to analyse the experimental data gathered here.

We first suppose that the particle moves parallel to its long axis at velocity, v . The fluid opposes this with a drag force whose amplitude is given by:

$$F_{drag}^{\parallel} = \zeta_{\parallel} v \quad \text{App.1}$$

with

$$\zeta_{\parallel}(k) = 16\pi\eta \frac{c}{k} f_{\parallel}(k) \quad \text{App.2}$$

and

$$f_{\parallel}(k) = \left[\frac{-2k}{k^2 - 1} + \frac{2k^2 - 1}{(k^2 - 1)^{\frac{3}{2}}} \ln \left(\frac{k + \sqrt{k^2 - 1}}{k - \sqrt{k^2 - 1}} \right) \right]^{-1} \quad \text{App.3}$$

Similarly, for motion perpendicular to the spheroid symmetry axis:

$$F_{drag}^{\perp} = \zeta_{\perp} v \quad \text{App.4}$$

with

$$\zeta_{\perp}(k) = 16\pi\eta \frac{c}{k} f_{\perp}(k) \quad \text{App.5}$$

and

$$f_{\perp}(k) = \left[\frac{k}{k^2 - 1} + \frac{2k^2 - 3}{(k^2 - 1)^{\frac{3}{2}}} \ln \left(k + \sqrt{k^2 - 1} \right) \right]^{-1} \quad \text{App.6}$$

The theory deals with the general case of a spheroid that starts sedimentation with an initial tilt angle, θ_0 (see Figure 78). Based on the symmetries of the particle shape and of the Stokes equation, the theory predicts that the particle will keep the same tilt angle throughout the sedimentation. The trajectory is a straight line whose tilt angle θ_{sed} depends on θ_0 :

$$\frac{\zeta_{\parallel}}{\zeta_{\perp}} \tan(\theta_0) = \tan(\theta_0 - \theta_{sed}) \quad \text{App.7}$$

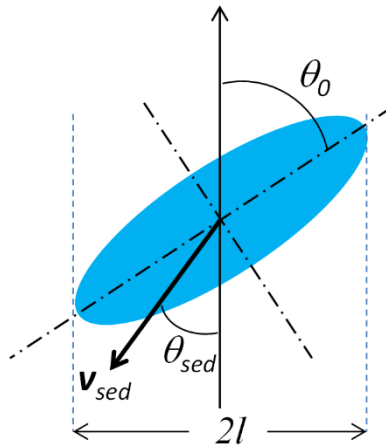


Figure 78: Sedimentation of a spheroid in an oblique configuration. θ_{sed} in the sketch is large, for clarity. In reality, calculated values of θ_{sed} are small ($\leq 6^\circ$).

Simple situations are those when the spheroid is initially vertical, or horizontal. In such conditions the particle falls vertically.

The spheroid is supposed to have the same volume and mass as that of a mother sphere with a radius, R_0 , whose sedimentation velocity is given by:

$$v_{sed}^{(0)} = \frac{2\Delta\rho g R_0^2}{9\eta} \quad \text{App.8}$$

Using Equations App.1 to App.6 and Equation App.8, we can deduce the sedimentation velocity of an initially vertical spheroid ($\theta_0 = 0$):

$$v_{sed}(k, \theta_0 = 0) = \frac{3}{8} k^{\frac{1}{3}} f_{\parallel}^{-1}(k) \cdot v_{sed}^{(0)} \quad \text{App.9}$$

Similarly, if the spheroid is horizontal:

$$v_{sed}\left(k, \theta_0 = \frac{\pi}{2}\right) = \frac{3}{8} k^{\frac{1}{3}} f_{\perp}^{-1}(k) \cdot v_{sed}^{(0)} \quad \text{App.10}$$

Below are shown the results of an experiment which has been carried out with a particle made from a polystyrene mother sphere of radius, $R_0 = 5\mu\text{m}$. The spheroid aspect ratio was estimated from the overall length of the particle as seen through the microscope, combined with the assumption of volume conservation. It was found that $2.65 \leq k \leq 2.83$. The particle, having a moderate aspect ratio, could be trapped in the standard vertical on-axis configuration, and so was prepared with a $\theta_0 = 0$ initial condition. Rather unexpectedly, the particle did not stay vertical and instead tumbled twice before reaching the floor of the sample cell. Throughout the sedimentation sequence, the sample cell was moved vertically to maintain the microscope image of the particle in focus. The particle altitude, z_{part} , was deduced from that of the cell (with a simple correction to take the refraction through water into account). The graphs in Figure 79 show z_{part} and the particle tilt angle, θ , as a function of time. The value of θ was estimated from the projected length ($2l$) of the particle image, using the following formula:

$$\cos^2(\theta) = \frac{k^2}{k^2 - 1} \left[1 - \left(\frac{l}{c}\right)^2 \right] \quad \text{App.11}$$

The predicted value of $v_{sed}^{(0)}$ is $2.73\mu\text{ms}^{-1}$, for $\eta = 10^{-3}\text{Pas}$. It is slightly lower than values measured in experiments with a suspension of mother spheres. The difference ($\sim 5\%$) may be due to an error either on the particle size, or on the value of the fluid viscosity for the temperature at which the experiments have been carried out.

The sedimentation trajectory of the spheroid (see Figure 79) roughly consists of two straight line portions, corresponding to $v_{sed}^{max} = 2.18\mu\text{ms}^{-1}$ and $v_{sed}^{min} = 1.78\mu\text{ms}^{-1}$. Because the tilt angle is far from constant throughout the descent of the particle, the theory cannot be applied in a straightforward manner. As a tentative option, we may compare the above values of v_{sed} to the predicted values for the vertical and horizontal configurations, respectively. These configurations correspond to the maximum and minimum values of the sedimentation velocity, in theory. The results are displayed in Table 5 for $k = 2.83$. The values are almost the same for the lower limit of the aspect ratio, $k = 2.65$. We see that the measured velocities are about

20% lower than the predictions for the vertical and horizontal orientations of the particle. In view of the statistical scatter of the experimental data, and of the limited applicability of the theory, it is estimated that measured sedimentation velocities are not significantly different from what might be expected.

Noteworthy, tumbling of spheroids during sedimentation was observed in all experiments, with particles of different sizes and aspect ratios. As a tentative explanation of the 20% anomaly in v_{sed} , it may be supposed that the particle rotation has the effect of slightly slowing down the sedimentation.

Experiment	$\frac{v_{sed}^{max}}{v_{sed}^{(0)}} = 0.80$	$\frac{v_{sed}^{min}}{v_{sed}^{(0)}} = 0.65$	$\frac{v_{sed}^{max}}{v_{sed}^{min}} = 1.23$
Theory	$\frac{v_{sed}^{\parallel}}{v_{sed}^{(0)}} = 1.04$	$\frac{v_{sed}^{\perp}}{v_{sed}^{(0)}} = 0.86$	$\frac{v_{sed}^{max}}{v_{sed}^{min}} = 1.22$

Table 5: Comparison of theoretical and measured values of sedimentation velocities for a spheroid-shaped particle of $k = 2.83$, with a mother sphere radius of $R_0 = 5\mu\text{m}$.

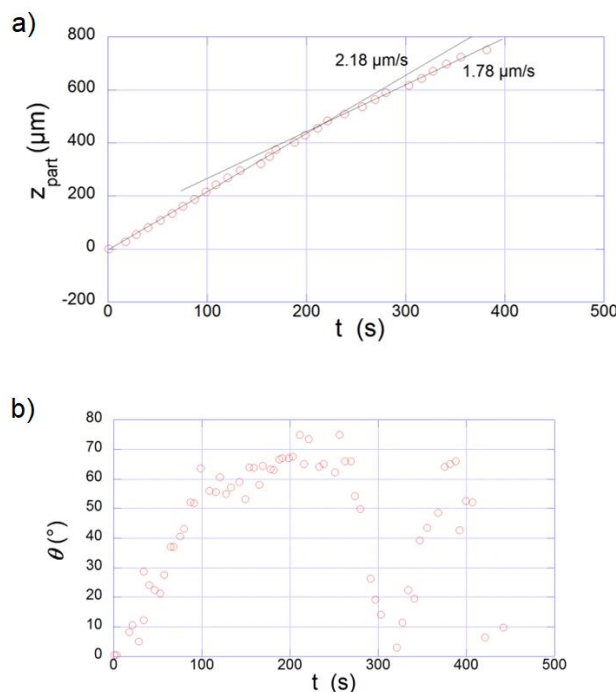


Figure 79: Sedimentation trajectory of a polystyrene spheroid. a) Altitude of the particle as a function of time. b) tilt angle as a function of time. Particle parameters: $k = 2.83$, with a mother sphere radius of $R_0 = 5\mu\text{m}$.

Numerical aperture calibration

In this appendix we describe the procedure which was followed to quantitatively control the aperture of the 100x microscope objective.

First, it is necessary to know the characteristics of the laser beam passing through the objective pupil. Since numerical apertures are involved, the light distribution within a cone of half-angle, u , is considered (see Figure 80). $u = u_{max}$ is the objective aperture angle when the iris diaphragm is fully open. The value of u_{max} is given by $NA = n_{oil} \sin(u_{max})$, where $n_{oil} \approx 1.50$ is the refractive index of oil. $NA_{max} = 1.30$ gives $u_{max} = 60.07^\circ = 1.049\text{rad}$. The minimum aperture, $NA_{min} = 0.60$, gives $u_{min} = 23.58^\circ = 0.412\text{rad}$. $\alpha \in [0, u]$ is the polar angle.

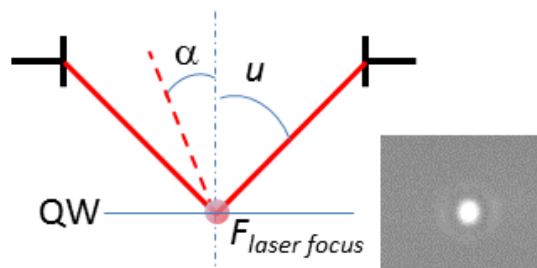


Figure 80: Sketch of objective diaphragm and aperture cone. The aperture angle, u , can be varied between u_{max} and u_{min} . The laser spot (red disk and photo on the right) has a finite size, which increases when closing the iris diaphragm.

The laser beam is supposed to be Gaussian. Thus, the intensity distribution in the plane of the diaphragm reads:

$$I(\alpha) = I_0 e^{\left(-\frac{\alpha^2}{\omega^2}\right)} \quad \text{App.12}$$

for $\alpha < u$, and $I(\alpha) = 0$ for $\alpha > u$.

The laser was focused on the quartz-water interface of the sample cell in order to obtain a clear image of the laser spot (see Figure 80). The total power of the beam in the observation plane, P_{obs} , can be determined (in arbitrary units) by integration of the video signal in each image (we used ImageJ software). The value of P_{obs} depends on the aperture angle, u :

$$P_{obs}(u) = I_0 2\pi \int_0^u e\left(\frac{2\alpha^2}{\omega^2}\right) \sin(\alpha) d\alpha$$

App.13

The experiment yields $\frac{P_{obs}(u_{min})}{P_{obs}(u_{max})} \cong 0.5$. Applying Equation App.13 for u_{max} and u_{min} , we can obtain the value of the beam waist, $\omega \cong 0.725\text{rad}$. It can be seen that the beam intensity is far from uniform within the pupil of the objective. The effective laser beam numerical aperture is $NA_{laser} = n_{oil} \sin(\omega) \cong 1.0$.

Knowing the value of ω , Equation App.13 Eq. (2) allows us to calculate the ratio, $\frac{P_{obs}(u)}{P_{obs}(u_{max})}$ for any value of u . In the experiment, the iris diaphragm was closed to some intermediate position (marked by a point on the objective mount) and the corresponding power ratio was measured. We may then fit the computed value to the measured one to obtain the value of u . This procedure was repeated for a set of intermediate positions of the iris diaphragm ring, and the corresponding NA values were obtained.

Spheroid tilt-tracking software

Video images of a tilted ellipsoid generally show two bright spots and a dark perimeter (see Figure 81 and Figure 82). These features can be monitored with a typical two-peak grey-level histogram of the image (see Figure 81). The main peak corresponds to the brighter zone, and the secondary peak corresponds to the other, less bright, bright zone. The user has to choose parameter values to isolate regions of the histogram close to these zones, and thus constitute two subsets of pixels. The program calculates the barycenters of both subsets, outputting the green and pink points of the bright spots, as can be seen in Figure 82. Note that the positions of both points coincide when the particle stands vertically, like in Figure 82 a) and f), and separate when the particle gets tilted, as shown in the rest of the frames of Figure 82. We take the distance d_{\perp} between the two points as the signal indicating that the particle is tilted. Note that d_{\perp} increases with the tilt angle, θ , but is not proportional to it.

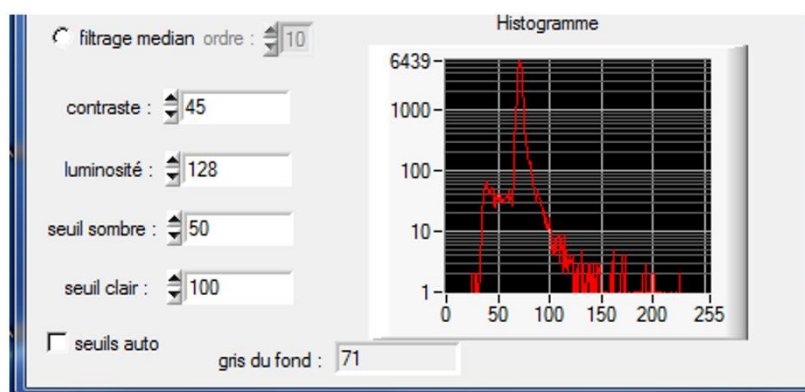


Figure 81: Graphical user interface of the tilt-tracking software. Example of a histogram of grey levels for a given image. The user chooses parameter values according to the positions and amplitudes of the two main peaks of the histogram.

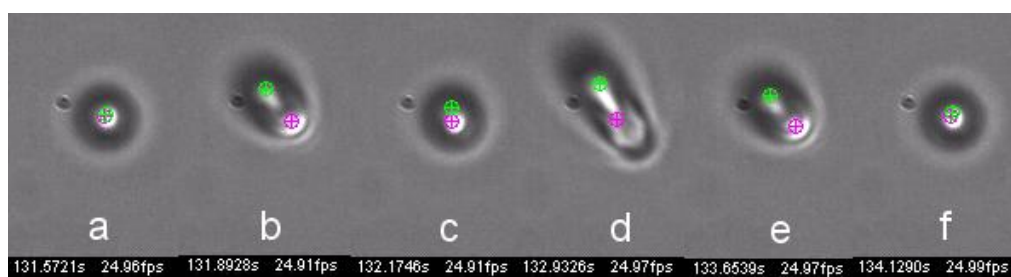


Figure 82: Video sequence showing the oscillation of a trapped ellipsoid in contact to the bottom boundary of the sample cell (quartz-water interface). The green and pink circled crosses indicate the bright spots. Numbers below each photo show the time (in seconds) and frame rate (fps).